Collaborative Investigations of Shallow Water Optics Problems

FINAL REPORT

On Work Performed by

Curtis D. Mobley

Sequoia Scientific, Inc.
2700 Richards Road, Suite 107
Bellevue, WA 98005

Under Contract N00014D01610003

Prepared for

Dr. Steve Ackleson
Environmental Optics Program
Code 322OP
Office of Naval Research
800 North Quincy Street
Arlington, VA 22217-5000

December, 2004

SEQUOIA

REPORT DOCUMENTATION PAGE

Form Approved
OMB No. 0704-0188

Public reporting burden for this collection of information is estimated to average 1 hour per response, including the time for reviewing instructions, searching existing data sources, gathering and maintaining the data needed, and completing and reviewing this collection of information. Send comments regarding this burden estimate or any other aspect of this collection of information, including suggestions for reducing this burden to Department of Defense, Washington Headquarters Services, Directorate for Information Operations and Reports (0704-0188), 1215 Jefferson Davis Highway, Suite 1204, Arlington, VA 22202-4302. Respondents should be aware that notwithstanding any other provision of law, no person shall be subject to any penalty for failing to comply with a collection of information if it does not display a currently valid OMB control number. **PLEASE DO NOT RETURN YOUR FORM TO THE ABOVE ADDRESS.**

1. REPORT DATE (DD-MM-YYYY)	2. REPORT TYPE	3. DATES COVERED (From - To)
21-12-2004	Final Report	Dec 2002 – Dec 2004

4. TITLE AND SUBTITLE
Collaborative Investigations of Shallow Water Optics Problems

5a. CONTRACT NUMBER
N00014-D-0161/0003

5b. GRANT NUMBER

5c. PROGRAM ELEMENT NUMBER

6. AUTHOR(S)
Curtis D. Mobley

5d. PROJECT NUMBER

5e. TASK NUMBER
0003

5f. WORK UNIT NUMBER

7. PERFORMING ORGANIZATION NAME(S) AND ADDRESS(ES)

Sequoia Scientific, Inc.
2700 Richards Road, Suite 107
Bellevue, WA 98005

8. PERFORMING ORGANIZATION REPORT NUMBER Project 48-3 Final Report

9. SPONSORING / MONITORING AGENCY NAME(S) AND ADDRESS(ES)
Environmental Optics and   Biology Program
Code 3220B
Office of Naval Research
800 North Quincy Street
Arlington, VA   22217-5000

10. SPONSOR/MONITOR'S ACRONYM(S)
ONR

11. SPONSOR/MONITOR'S REPORT NUMBER(S)

12. DISTRIBUTION / AVAILABILITY STATEMENT

13. SUPPLEMENTARY NOTES

14. ABSTRACT
A combination of HydroLight and Monte Carlo numerical modeling was used to quantify the effects of water column optical properties, bottom morphology, bottom material reflectances, bottom bidirectional reflectance distribution functions (BRDFs), and external environmental conditions on remote-sensing reflectances in optically shallow waters. It was found that typical variability in these quantities generally causes no more than 10% error in the recovery of bathymetry from hyperspectral remote sensing reflectances. Other research performed under this contract included investigations of radiometer self shading, underwater visibility, analytical modeling of remote sensing reflectances in both deep and shallow Case 2 waters, semianalytical methods for inversion of the radiative transfer equation, and the use of neural networks and regression for inversion of ocean color spectra. Reprints of five publications are included in this report.

15. SUBJECT TERMS
HydroLight, Monte Carlo, shallow water optics, ocean color, remote sensing, look-up-table, hyperspectral imagery

16. SECURITY CLASSIFICATION OF:			17. LIMITATION OF ABSTRACT	18. NUMBER OF PAGES	19a. NAME OF RESPONSIBLE PERSON
a. REPORT UNCLASSIFIED	**b. ABSTRACT** UNCLASSIFIED	**c. THIS PAGE** UNCLASSIFIED	Unlimited	87	Curtis Mobley

19b. TELEPHONE NUMBER (include area code)
425-641-0944 x 109

Standard Form 298 (Rev. 8-98)
Prescribed by ANSI Std. Z39.18

Collaborative Investigations of Shallow Water Optics Problems

FINAL REPORT

On Work Performed by

Curtis D. Mobley

Sequoia Scientific, Inc.
2700 Richards Road, Suite 107
Bellevue, WA 98005

Under Contract N00014D01610003

December, 2004

SE QUOIA

TABLE OF CONTENTS

Collaborative Investigations of Shallow Water Optics Problems

Curtis D. Mobley

Sequoia Scientific, Inc.
2700 Richards Road, Suite 107
Bellevue, WA 98005
phone: 425-641-0944 x 109   fax: 425-643-0595   email: curtis.mobley@sequoiasci.com

Research Objectives

The primary goal of this work was to understand in detail the relative contributions of water column optical properties, bottom morphology, bottom material reflectances, bottom bidirectional reflectance distribution functions (BRDFs), and external environmental conditions on remote-sensing reflectances in optically shallow waters. A secondary goal of the work was to participate in various collaborations with other investigators on oceanic optics problems of Navy interest.

Various methodologies are now under development for the extraction of environmental information such as water-column absorption and scattering properties, bottom depth, and bottom type from remotely sensed hyperspectral imagery obtained in optically shallow waters. Regardless of the methodology used, errors in measured or predicted hyperspectral remote-sensing reflectances $R_{rs}(\lambda)$ will degrade our ability to extract information from the spectra. The potential errors therefore must be understood.

A "look-up-table" (LUT) methodology for extraction of environmental information from measured R_{rs} spectra is under development with separate funding (Mobley et al., 2004). That technique relies on matching computed and measured R_{rs} spectra. To assess the potential errors in the spectrum matching, and to ascertain where additional effort should be expended in improving the underlying LUT databases, it is necessary to know when and how each potential source of error in computed R_{rs} spectra comes in to play.

Other research performed under this contract include investigations of radiometer self shading, underwater visibility, analytical modeling of remote sensing reflectances in both deep and shallow Case 2 waters, semianalytical methods for inversion of the radiative transfer equation, and the use of neural networks and multilinear regression for inversion of ocean color spectra.

Approach

In my primary research, I used a combination of HydroLight (www.hydrolight.info; Mobley and Sundman, 2001a, 2001b) and Monte Carlo numerical modeling to quantify how various sources of error influence predicted R_{rs} spectra. For example, one can expect that water-column absorption and scattering properties (including phase function effects) will be less (more) important for shallow (deep) waters, and that bottom properties (BRDF, material reflectance) will be more (less) important in shallow (deep) waters. However, the interplay of these error sources is complex and simple rules for error analysis are hard to develop. Detailed numerical simulations and validation with observational data are needed for full understanding.

In my secondary work, I used both HydroLight and my Backward Monte Carlo Three Dimensional (BMC3D) code to carry out the needed simulations.

Work Completed

The primary work quantifying sensor, sky, water-column, and bottom effects on retrieval of environmental information from remote-sensing reflectances was presented at Ocean Optics XVII, held in Fremantle, Australia in October 2004. Those results are now being prepared for submission as a refereed journal article.

Additional work completed and published under this contract includes the following:

- A study of self-shading of in-water radiometers (Leathers, Downes, and Mobley, 2004; this paper is attached as Appendix A), which included shallow water effects. This work used the BMC3D Monte Carlo code previously developed with ONR funding under the CoBOP program.

- Development of an analytical model for prediction of remote-sensing reflectances in both deep and shallow waters Case 2 waters (Albert and Mobley, 2004; this paper is attached as Appendix B), which used my HydroLight model.

- A study of bioluminescence and underwater visibility (Johnsen, Widder, and Mobley, 2004; this paper is attached as Appendix C), which used a modified version of my BMC3D Monte Carlo code for computation of the needed Point Spread Functions.

- A comparison of neural networks and regression algorithms for inversion of remote-sensing reflectances (Dransfeld, Tatnall, Robinson, and Mobley; this paper is attached as Appendix D), which used HydroLight to generate test data.

- Investigation of shape-factor models for use in retrieving inherent optical properties from remote sensing reflectances (Hoge, Lyon, Mobley, and Sundman, 2003; this

- Investigation of shape-factor models for use in retrieving inherent optical properties from remote sensing reflectances (Hoge, Lyon, Mobley, and Sundman, 2003; this paper is attached as Appendix E), which used HydroLight.

- Completion of a technical report documenting the Monte Carlo techniques used in several of my studies (Leathers, Downes, Davis, and Mobley, 2004; this report is available on CD, published by NRL-DC).

Results

Consider, as one example of my primary investigations, the LUT methodology for retrieval of bathymetry in optically shallow waters. The HydroLight-generated R_{rs} spectrum database used to match the image R_{rs} spectra was created with various sets of inherent optical properties (IOPs, namely the absorption a, scattering b, and backscattering b_b coefficients). Suppose the database includes R_{rs} spectra corresponding to a and b coefficients that are representative of the imaged water, but does not have in it R_{rs} spectra corresponding to the backscatter fraction $B = b/b_b$ values that occurred in nature at the time the image was acquired. The database R_{rs} spectra will then be a mismatch for the image R_{rs} spectra, and errors in the retrieved bathymetry will result. We thus ask how important it is that the database contains IOPs with the correct B; i.e., how large are the bathymetry errors if the database B values do not correspond to those in nature.

Figure 1 shows four points in the vicinity of Lee Stocking Island, Bahamas, for which water-column IOPs, bathymetry, and bottom classification are known from field observations and are well described in the existing LUT database. These points correspond to shallow (2 m depth) and deeper (8 m) sand (highly reflecting) and seagrass (dark) bottoms. Figure 2 shows the corresponding PHILLS spectra and the closest-matching spectra from the LUT database.

Starting with the "known answers" for these points, I generated R_{rs} spectra for B values ranging from 0.005 to 0.05 (total backscatter fraction, including water and particles), whereas the correct value was near 0.02. The depths (2 m and 8 m) and bottom types (sand and grass) were held the same. I then treated the newly generated R_{rs} spectra as though they were image spectra and searched the database, which contained only spectra with B near 0.02, to retrieve the known depths.

Figure 3 shows a histogram of the depths retrieved when the database does not contain the correct water column B values. For the 2 m depth, the retrievals always gave the correct depth, which was included in the database at intervals of 0.25 m. In other words, the mismatch between the actual (for various B values) and database spectra was not enough to trigger selecting a bottom spectrum that was off by as much as 0.25 m. For such shallow water, the water column backscatter fraction is thus unimportant. For the 8 m depth, the correct depth of 8 m was retrieved 80% of the time over the bright sand bottom, but there

3

was a spread of retrieved depths (7 to 9.5 m) over the dark grass bottom. This shows the importance of having the correct backscatter fraction, all else being the same, as a function of bottom depth and type.

As another example of this type of study, I generated IOPs with various a, b, and b_b spectra: namely for 5 sets of a-a_w, 5 sets of b-b_w, and 5 backscatter fractions, for a total of 125 combinations of IOPs. Figure 4 shows the corresponding R_{rs} spectra for the absorption perturbations (with the scattering and backscattering spectra held constant at their baseline values). Figure 5 shows the histogram of depth retrievals for the 125 combinations of IOP perturbations. We again see that the depth retrievals are quite good. Even for the dark seagrass bottom and 8 m, for which the IOPs are most important, the depth is retrieved to within ±1 m in 85% of the cases.

Similar studies were carried out to assess the importance of the bottom BRDF (Lambertian vs non-Lambertian BRDFs), bottom irradiance reflectance, bottom slope, rippled bottoms (as opposed to smooth flat bottoms), sky conditions, sensor noise, and the like. Without going into the details of each aspect of the study, the overall conclusions from these investigations can be summarized as follows:

- Retrievals of depth, bottom reflectance, and water-column IOPs are not degraded by typical amounts of sensor noise (e.g., random noise, spikes, dropoff near 400 nm).

- Systematic offsets in measured R_{rs} do degrade retrievals, but such offsets are often easy to identify and correct.

- Non-Lambertian bottoms (not included in the present LUT database) can cause depth-retrieval errors of ~10% (i.e., std dev of retrieved depths / true depth ~0.1).

- Sun angle (30 to 60 deg) and off-nadir viewing direction (out to ~30 deg) are not critical for LUT retrievals.

- Random noise in IOPs does not degrade retrievals.

- Systematic perturbations in IOPs can cause depth errors of ~10% for darker and deeper bottoms.

I am currently completing the study of the effects of environmental conditions on remote-sensing reflectances and the implications for LUT retrieval of bathymetry and bottom classification. This work was described in a talk at the Ocean Optics XVII conference. A journal article presentation of the full suite of studies is in preparation.

The results of the secondary studies can be seen in the attached reprints of the resulting journal articles and therefore will not be discussed here.

Impact and Applications

Hyperspectral imagery is increasingly used for a wide range of problems from mapping and monitoring seagrass beds and coral reefs to remote sensing of bathymetry and bottom classification for military applications. For quantitative analysis of hyperspectral imagery it is necessary to have calibrated, accurate hyperspectral reflectance spectra. This need in turn makes it necessary to evaluate in detail the various sources of error in such spectra. By quantifying various error sources, this work provides guidance as to where additional effort should be expended to improve measurements and models used in the analysis of hyperspectral data.

The secondary investigations contribute to our overall knowledge of underwater visibility and to the development of a wide range of tools for extraction of environmental information from remote-sensed ocean color data in a variety of waters (deep or shallow, Case 1 or Case 2). All of these topics are of great Navy relevance, as well as of interest to the optical oceanography research community in general.

Collaborations and Related Projects

This work used data sets, imagery, and models (namely PHILLS imagery and the BMC3D computer code) previously obtained or developed during the ONR CoBOP program. This work directly contributed to my separately funded work on developing the look-up-table methodology for extraction of environmental information from hyperspectral imagery.

My primary work was done in close collaboration with Paul Bissett, Dave Kohler, Mubin Kadawala, Bhavesh Goswami, and others at the Florida Environmental Research Institute. PHILLS imagery and other collaborations were provided by Curtiss Davis, Robert Leathers, Valerie Downes, Marcos Montes and others at the Naval Research Lab, Washington D.C.

The collaborations on the secondary work can be seen in the author list of the attached publications.

References

Albert, A. and C. D. Mobley, 2003. An analytical model for subsurface irradiance and remote sensing reflectance in deep and shallow case 2 waters. *Optics Express* 11(22), 2873-2890.

Dransfeld, S., A. R. Tatnall, I. S. Robinson, and C. D. Mobley, 2004. A comparison of multi-layer perceptron and multilinear regression algorithms for the inversion of synthetic ocean colour spectra,, *Int. J. Remote Sensing*, 25(21), 4829-4834.

Hoge, F. E., P. E. Lyon, C. D. Mobley, and L. K. Sundman, 2003. Radiative transfer equation inversion: Theory and shape factor models for retrieval of oceanic inherent optical properties. *J. Geophys. Res.* 108 (C12), 3386-3399.

Johnson, S., E. A. Widder, and C. D. Mobley, 2004. Propagation and perception of bioluminescence: Factors affecting counterillumination as a cryptic strategy. *Biol. Bull.* 207, 1-16.

Leathers, R. A., T. V. Downes, and C. D. Mobley, 2004. Self-shading corrections for oceangraphic upwelling radiometers, *Optics Express* 12(20), 4709-4718.

Leathers, R. A., T. V. Downes, C. O. Davis, and C. D. Mobley, 2004. Monte Carlo radiative transfer simulations for ocean optics: A practical guide. Naval Research Lab Report NRL/MR/5660—04-8819. Available an CD from the Naval Research Lab.

Mobley, C. D. and L. K. Sundman, 2001a. Hydrolight 4.2 Users' Guide. Sequoia Scientific, Inc., Bellevue, WA, 88 pages (downloadable as a pdf file at www.hydrolight.info).

Mobley, C. D. and L. K. Sundman, 2001b. Hydrolight 4.2 Technical Documentation. Sequoia Scientific, Inc., Bellevue, WA, 79 pages (downloadable as a pdf file at www.hydrolight.info).

Mobley, C. D., L. K. Sundman, C. O. Davis, T. V. Downes, R. A. Leathers, M. J. Montes, J. H. Bowles, W. P. Bissett, D. D. R. Kohler, R. P. Reid, E. M. Louchard, and A. Gleason, 2004. Interpretation of hyperspectral remote-sensing imagery via spectrum matching and look-up tables. *Applied Optics* [submitted March 2004]

Publications

Albert, A. and C. D. Mobley, 2003. An analytical model for subsurface irradiance and remote sensing reflectance in deep and shallow case 2 waters. *Optics Express* 11(22), 2873-2890.

Dransfeld, S., A. R. Tatnall, I. S. Robinson, and C. D. Mobley, 2004. A comparison of multi-layer perceptron and multilinear regression algorithms for the inversion of synthetic ocean colour spectra,, *Int. J. Remote Sensing*, **25**(21), 4829-4834.

Hoge, F. E., P. E. Lyon, C. D. Mobley, and L. K. Sundman, 2003. Radiative transfer equation inversion: Theory and shape factor models for retrieval of oceanic inherent optical properties. *J. Geophys. Res.* 108 (C12), 3386-3399.

Johnson, S., E. A. Widder, and C. D. Mobley, 2004. Propagation and perception of bioluminescence: Factors affecting counterillumination as a cryptic strategy. *Biol. Bull.* 207, 1-16.

Leathers, R. A., T. V. Downes, and C. D. Mobley, 2004. Self-shading corrections for oceangraphic upwelling radiometers, *Optics Express* 12(20), 4709-4718.

Leathers, R. A., T. V. Downes, C. O. Davis, and C. D. Mobley, 2004. Monte Carlo radiative transfer simulations for ocean optics: A practical guide. Naval Research Lab Report NRL/MR/5660—04-8819. Available an CD from the Naval Research Lab.

Figure 1. PHILLS image of the Adderly Cut area near Lee Stocking Island, Bahamas. The numbered points are the pixels where I performed detailed calculations to evaluate the various sources of error in computed remote-sensing reflectances.
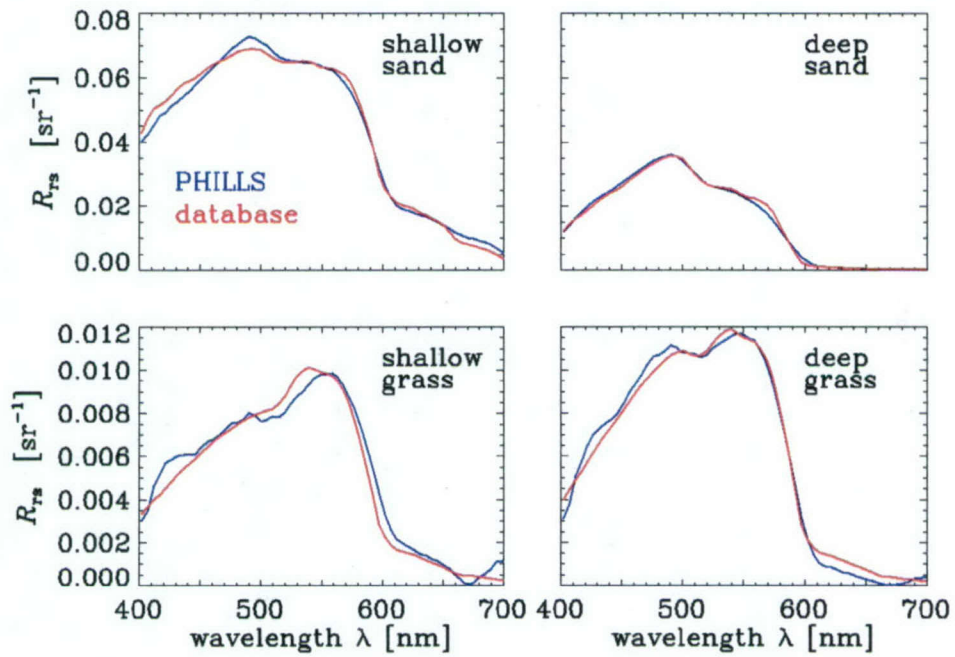
Fig. 2. Measured (PHILLS, blue curves) and closest-matching LUT database (red curves) spectra. These spectra were the starting points for the study.
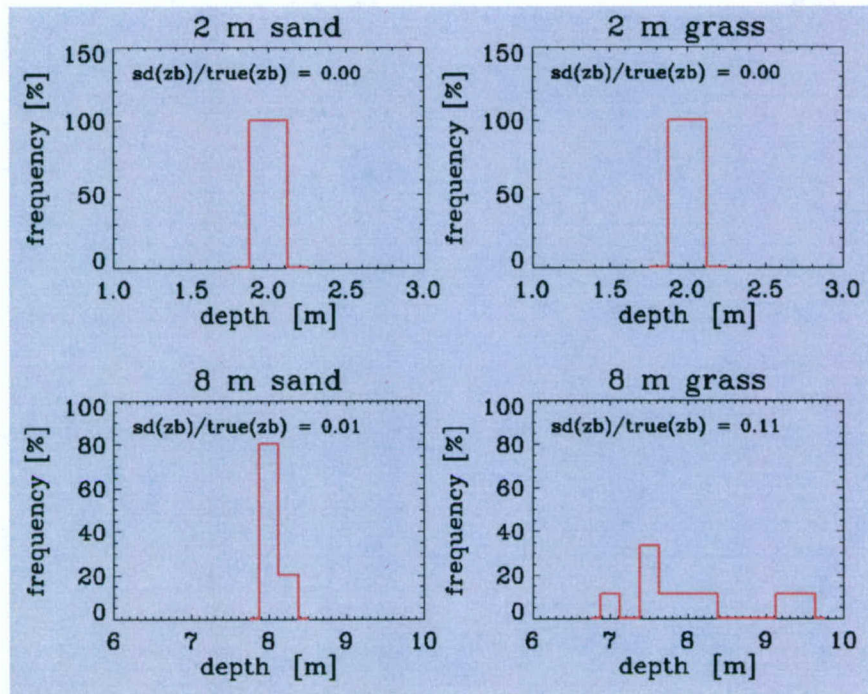
Figure 3. Histograms showing the errors in the retrieved bottom depths if the database of remote-sensing reflectances does not contain the correct water-column backscatter fraction.
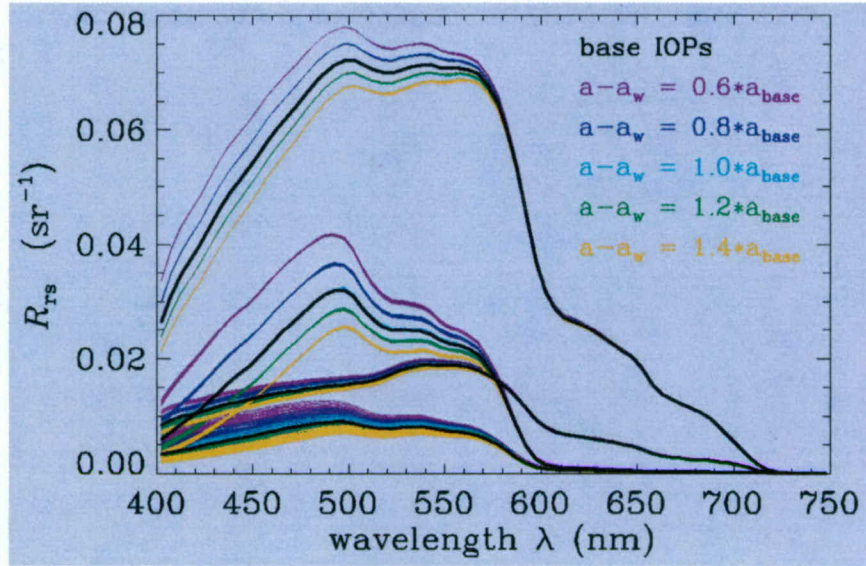
Fig. 4. The Rrs spectra corresponding to perturbations in the absorption coefficient. The upper group of curves is for sand at 2 m depth; the middle group is sand at 8 m; the bottom two groups are seagrass at 2 and 8 m.
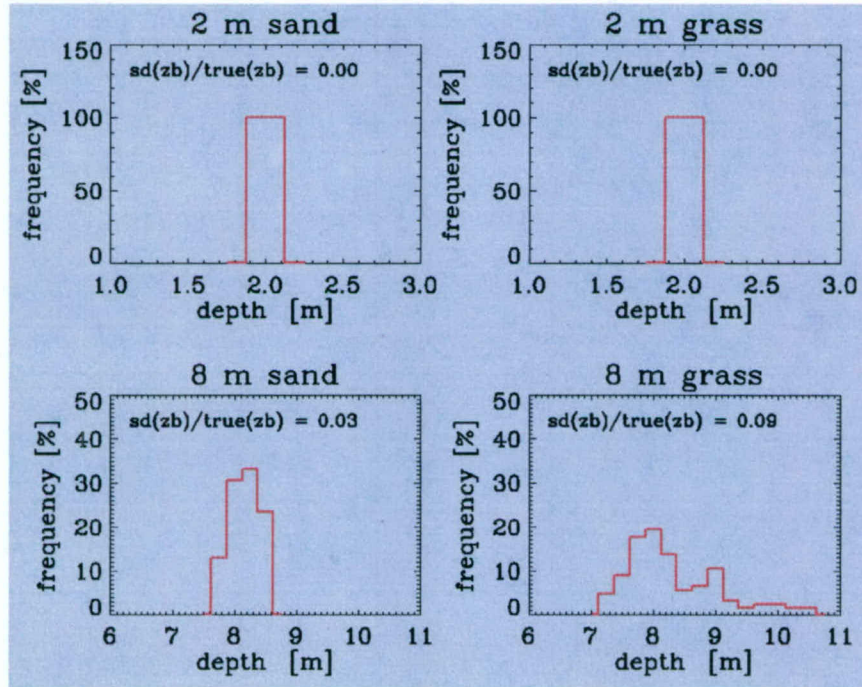
Fig. 5. Histogram of the depth retrievals for 125 different IOP perturbations (as illustrated in Fig. 4 for the absorption perturbations.).

Appendix A.

Self-shading correction for oceanographic upwelling radiometers

Robert A. Leathers, Trijntje Valerie Downes

Optical Sciences Division, U. S. Naval Research Laboratory
4555 Overlook Avenue SW, Washington, DC 20375
leathers@nrl.navy.mil, downes@nrl.navy.mil

Curtis D. Mobley

Sequoia Scientific, 2700 Richards Road, Suite 107, Bellevue, Washington 98005
mobley@sequoiasci.com

Abstract: We present the derivation of an analytical model for the self-shading error of an oceanographic upwelling radiometer. The radiometer is assumed to be cylindrical and can either be a profiling instrument or include a wider cylindrical buoy for floating at the sea surface. The model treats both optically shallow and optically deep water conditions and can be applied any distance off the seafloor. We evaluate the model by comparing its results to those from Monte Carlo simulations. The analytical model performs well over a large range of environmental conditions and provides a significant improvement to previous analytical models. The model is intended for investigators who need to apply self-shading corrections to radiometer data but who do not have the ability to compute shading corrections with Monte Carlo simulations. The model also can provide guidance for instrument design and cruise planning.

References and links

1. H. R. Gordon and K. Ding, "Self-shading of in-water optical instruments," Limnol. Oceanogr. **37**, 491-500 (1992).
2. R. A. Leathers, T. V. Downes, and C. D. Mobley, "Self-shading correction for upwelling sea-surface radiance measurements made with buoyed instruments," Opt. Express **8**, 561-570 (2001).
3. D. R. Lyzenga, "Remote sensing of bottom reflectance and water attenuation parameters in shallow water using aircraft and Landsat data," Int. J. Remote Sensing **2**, 71-82 (1981).
4. J. E. O'Reilley, S. Maritorena, B. G. Mitchell, D. A. Siegel, K. L. Carder, S. A. Garver, M. Kahru, and C. McClain, "Ocean color chlorophyll algorithms for SeaWiFS," J. Geophys. Res. **103**, 24937-24953 (1998).
5. E. M. Louchard, R. P. Reid, C. F. Stephens, C. O. Davis, R. A. Leathers, T. V. Downes, and R. Maffione, "Derivative analysis of absorption features in hyperspectral remote sensing data of carbonate sediments," Opt. Express **10**, 1573-1584 (2002).
6. E. M. Louchard, R. P. Reid, F. C. Stephens, C. O. Davis, R. A. Leathers, and T. V. Downes, "Optical remote sensing of benthic habitats and bathymetry in coastal environments at Lee Stocking Island, Bahamas: A comparative spectral classification approach," Limnol. Oceanogr. **48**, 511-521 (2003).
7. H. M. Dierssen, R. C. Zimmerman, R. A. Leathers, T. V. Downes, and C. O. Davis, "Ocean color remote sensing of seagrass and bathymetry in the Bahamas Banks by high-resolution airborne imagery," Limnol. Oceanogr. **48**, 444-455 (2003).
8. J. L. Mueller et al., "Ocean optics protocols for satellite ocean color sensor validation, Revision 4, Volume III: radiometric measurements and data analysis protocols," National Aeronautical and Space Administration Report 21621 (2003).
9. G. Zibordi and G. M. Ferrari, "Instrument self-shading in underwater optical measurements: experimental data," Appl. Opt. **34**, 2750-2754 (1995).
10. E. Aas and B. Korsbø, "Self-shading effect by radiance meters on upward radiance observed in coastal waters," Limnol. Oceanogr. **42**, 974-980 (1997).
11. J. Piskozub, A. R. Weeks, J. N. Schwarz, and I. S. Robinson, "Self-shading of upwelling irradiance for an instrument with sensors on a sidearm," Appl. Opt. **39**, 1872-1878 (2000).

12. C. D. Mobley, *Light and Water* (Academic Press, New York, 1994).
13. R. A. Leathers and N. J. McCormick, "Algorithms for ocean-bottom albedo determination from in-water natural-light measurements," Appl. Opt. **38**, 3199-3205 (1999).
14. K. S. Baker and R. C. Smith, "Irradiance transmittance through the air-water interface," in Ocean Optics X, R. W. Spinrad, ed., Proc. SPIE **1302**, 556-565 (1990).
15. J. Piskozub, "Effects of surface waves and sea-bottom on self-shading on in-water optical instruments," in Ocean Optics XII, J. Jaffe, ed., Proc. SPIE **2258**, 300-308 (1994).

1. Introduction

When a radiometer is positioned to measure upwelling light, its shadow decreases the magnitude of the local light field, causing measured values of upwelling radiance, and hence remote sensing reflectance, to be too low. The magnitude of the error depends on wavelength, sensor size, water turbidity, and illumination conditions [1], and in shallow water it also depends on the water depth and seafloor reflectivity [2]. The self-shading error has a direct effect on the measurement of atmospheric optical thickness and on remote sensing sensor calibration. Furthermore, because the magnitude of the shading error is wavelength dependent, algorithms that depend on the spectral shape of upwelling radiance to determine water properties, water depth, or water characteristics [3–7] will also return erroneous results. Therefore, proper ocean optics protocols dictate that shading corrections should be routinely applied to all in situ upwelling light measurements [8]. Unfortunately, instrument manufacturers do not typically provide self-shading correction algorithms for their products.

We developed a Monte Carlo code [2] to compute the self-shading of buoyed radiometer data collected in 1999 and 2000 at Lee Stocking Island (LSI), Bahamas [5–7]. The self-shading of upwelling radiometers has also been investigated by other researchers [1, 9–11]; however, none of these investigations consider optically shallow waters such as those at LSI nor do they account for the additional shading caused by a flotation buoy such as that on the Hyper-TSRB.

The objective of this paper is to present a new analytical self-shading correction model for buoyed and unbuoyed upwelling radiometers. We evaluate the model with numerical simulations and then discuss the model's uses and limitations. Although Monte Carlo computations provide a more accurate method for making self-shading corrections, we believe that analytical or semianalytical models are more likely to be implemented by the general community because of the ease of which they can be disseminated and applied.

2. Model derivation

We present separate analytical shading corrections for a sensor optically far from the seafloor and a sensor close to the seafloor and then combine the two into one general correction algorithm. We derive the shading correction for a radiometer far from the seafloor by considering the idealized model shown in Fig. 1, which is a slightly generalized version of the model used by Gordon and Ding [1]. A small sensor with infinitesimally small field of view (FOV) is positioned at a distance z_s below a shading disk of radius r. The shading disk can represent the bottom of either the sensor head (if $z_s = 0$) or a buoy (if $z_s > 0$). The solar illumination is taken to be collimated and the amount of in-water scattering by water is assumed to be small enough to not significantly disturb the collimated nature of downwelling light. The goal is to determine how much the measured upwelling radiance is reduced by the shadow that falls across the sensor's line of sight.

The depth to which the shadow lies across the sensor's line of sight is [1]

$$z_0 = r/\tan\theta_{0w} , \tag{1}$$

where the in-water solar zenith angle θ_{0w} is related to the above-water solar zenith angle θ_0 by [12]

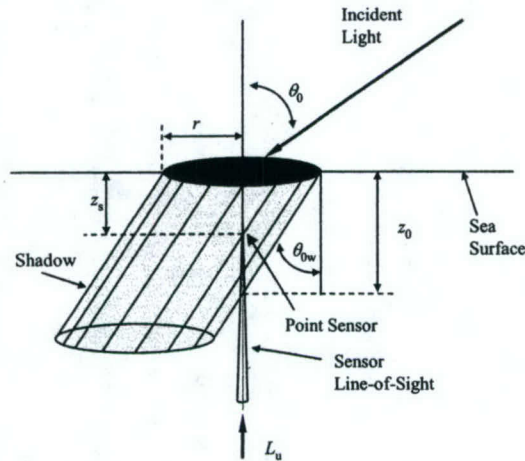$$\theta_{0w} = \sin^{-1}\left(\sin\theta_0/1.338\right). \tag{2}$$

Fig. 1. Shading of an upwelling radiance sensor by a horizontal disk of radius r.

The depth dependence of the true (i.e., unshaded) radiance $L_u{}^t$ can be expressed as

$$L_u{}^t(z) = L_u{}^t(z_s)\exp\left[-K_u(z-z_s)\right], \tag{3}$$

where K_u is a depth-averaged value of the diffuse attenuation coefficient for $L_u(z)$. Because a negligible amount of light is scattered into the detector from within the shaded region, the measured radiance $L_u{}^m$ is equal to the radiance at depth z_0 attenuated back up to the sensor depth z_s,

$$L_u{}^m = L_u{}^t(z_0)\exp\left[-a(z_0-z_s)\right]. \tag{4}$$

Using Eq. (3) to obtain $L_u{}^t(z_0)$ and substituting this into Eq. (4), we obtain

$$L_u{}^m = L_u{}^t(z_s)\exp\left[-(K_u+a)(z_0-z_s)\right]. \tag{5}$$

For collimated light, $K_u \cong a/\cos\theta_{0w}$; substituting this and Eq. (1) into Eq. (5) gives

$$L_u{}^m = L_u{}^t(z_s)\exp\left[-k\,a(r-z_s\tan\theta_{0w})\right], \quad \tan\theta_{0w} < r/z_s, \tag{6}$$

where

$$k = (1/\tan\theta_{0w} + 1/\sin\theta_{0w}). \tag{7}$$

The fractional shading error in deep water is

$$\varepsilon_w = 1 - \frac{L_u{}^m}{L_u{}^t(z_s)} = \begin{cases} 1-\exp\left[-k\,a(r-z_s\tan\theta_{0w})\right], & \tan\theta_{0w} < r/z_s \\ 0, & \tan\theta_{0w} > r/z_s \end{cases}. \tag{8}$$

For self-shading of a sensor head only (i.e., $z_s = 0$), Eq. (8) reduces to

$$\varepsilon_w = \left[1-\exp(-k\,ar)\right]. \tag{9}$$

Equation (9) is the same expression derived by Gordon and Ding [1] except that they derived it using the approximation $K_u = a$ (instead of $K_u = a/\cos\theta_{0w}$), which leads to $k = 2/\tan\theta_{0w}$. The difference between $k = 2/\tan\theta_{0w}$ and $k = (1/\tan\theta_{0w} + 1/\sin\theta_{0w})$ is only significant for large values of θ_{0w}.

In our low-scattering model, the shading due to the sensor head and that due to the buoy are never additive. At small solar zenith angles, the depth of the buoy's shadow below the sensor is deeper than the depth of the sensor-head's shadow, and the sensor head contributes no shading beyond that already caused by the buoy. Conversely, the presence of the buoy contributes no additional shading to that caused by the sensor head at large solar zenith angles. The transition is at $\tan\theta_{0w} = (r_s - r_b)/z_s$, where r_s and r_b are the radii of the buoy and

sensor head, respectively, and z_s is the distance between the bottoms of the two. The total shading of a buoyed radiometer is then simply the larger of the two effects,

$$\varepsilon_w = \begin{cases} 1 - \exp\left[-k\,a\left(r_b - z_s \tan\theta_{0w}\right)\right], & \tan\theta_{0w} < \left(r_s - r_b\right)/z_s \\ 1 - \exp\left[-k\,a\,r_s\right], & \tan\theta_{0w} > \left(r_s - r_b\right)/z_s \end{cases}. \tag{10}$$

Although Fig. 1 shows the shading disk at the sea surface, Eq. (10) is valid for submerged instruments if the illumination is handled correctly; this is discussed below. Also note that the derivation of Eq. (10) assumes that the total water depth z_{bot} is greater than the depth z_0; otherwise, $\varepsilon_w = 1$.

An expression for self-shading close to the seafloor (i.e., when the upwelling light is due primarily to bottom reflection) can be developed using the model shown in Fig. 2. A sensor with finite FOV is located at depth z_s and a shading disk of radius r_d is located at depth z_d. (For the case of self-shading of the sensor head, $z_d = z_s$.) The total water depth is z_{bot}. If the seafloor is horizontal then both the sensor FOV and the shading disk project circles onto the seafloor. For a Lambertian seafloor and a sensor that responds equally to light from all directions within its FOV, the percent shading due to the shadow on the seafloor approximately equals the fraction of the FOV circle that is overlapped by the shading circle. One of four situations exists: the two circles do not overlap; the FOV circle is completely inside the shade circle; the shade circle is completely inside the FOV circle; or the two circles partially overlap. Let the x-axis lie in the horizontal plane such that the positive-x direction is looking away from the sun. The shadow on the seafloor is of radius r_d and is centered at $x_d = (\tan\theta_{0w})(z_{bot} - z_d)$. The FOV on the seafloor is centered at $x = 0$ and has radius $r_{fov} = (\tan\theta_{fov})(z_{bot} - z_s)$, where θ_{fov} is the FOV half-angle. The fractional shading can be expressed mathematically as

$$\varepsilon_B = \begin{cases} 0, & \left(x_d - r_d\right) > r_{fov} \\ 1, & \left(-r_{fov}\right) > \left(x_d - r_d\right) \\ \left(r_d / r_{fov}\right)^2, & \left(x_d + r_d\right) < r_{fov} \\ \dfrac{2}{\pi r_{fov}^2}\left(\displaystyle\int_{x_d - r_d}^{x_{int}} \sqrt{r_d^2 - \left(x - x_d\right)^2}\,dx + \int_{x_{int}}^{r_{fov}} \sqrt{r_{fov}^2 - x^2}\,dx\right), & \begin{cases}\left(-r_{fov}\right) < \left(x_d - r_d\right) < r_{fov} \\ \text{and } r_{fov} < \left(x_d + r_d\right)\end{cases} \end{cases}, \tag{11}$$

where

$$x_d = \tan\theta_{0w}\left(z_{bot} - z_d\right), \quad r_{fov} = \left[\tan\theta_{fov}\left(z_{bot} - z_s\right)\right], \quad \text{and} \quad x_{int} = \frac{r_{fov}^2 - r_d^2 + x_d^2}{2x_d}.$$

The integrals in Eq. (11) can be evaluated analytically:

$$\int_{x_d - r_d}^{x_{int}} \sqrt{r_d^2 - \left(x - x_d\right)^2}\,dx = \frac{x_{int} - x_d}{2}\sqrt{r_d^2 - \left(x_{int} - x_d\right)^2} + \frac{r_d^2}{2}\sin^{-1}\left(\frac{x_{int} - x_d}{r_d}\right) + \frac{\pi r_d^2}{4}$$

and

$$\int_{x_{int}}^{r_{fov}} \sqrt{r_{fov}^2 - x^2}\,dx = \frac{\pi r_{fov}^2}{4} - \frac{x_{int}}{2}\sqrt{r_{fov}^2 - x_{int}^2} - \frac{r_{fov}^2}{2}\sin^{-1}\left(\frac{x_{int}}{r_{fov}}\right).$$

For a buoyed radiometer, we will approximate the overall shading error close to the seafloor with

$$\varepsilon_B = \max(\varepsilon_s, \varepsilon_b), \tag{12}$$

where ε_s is obtained from Eq. (11) with r_d and z_d taken to be the radius and depth of the sensor head and ε_b is obtained from Eq. (11) with r_d and z_d taken to be the radius and depth of the buoy.
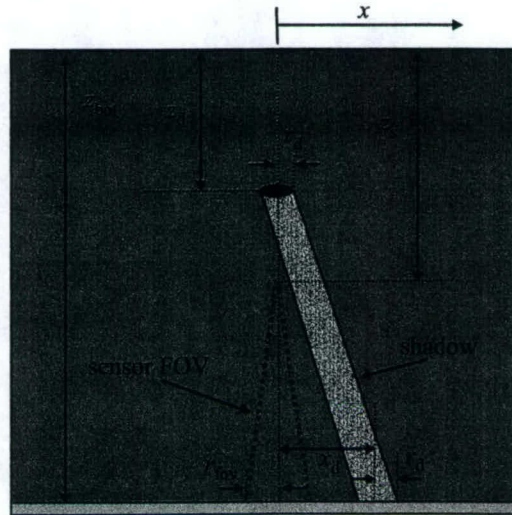
Fig. 2. Model for computing the amount of the overlap between the shadow on the seafloor and the sensor FOV.

Now that we have developed a shading model for a radiometer far from the seafloor [Eq. (10)] and a shading model for a radiometer very close to the seafloor [Eqs. (11) and (12)], the final step is to construct a transition from one to the other. We take the overall fractional error ε to be the weighted sum of the two models based on the relative importance of the signal from the seafloor at the depth of the radiometer, i.e.

$$\varepsilon = \left(\frac{L_{uw}(z_s)}{L_u{}^t(z_s)} \right) \varepsilon_w + \left(\frac{L_{uB}(z_s)}{L_u{}^t(z_s)} \right) \varepsilon_B , \qquad (13)$$

where ε_w is obtained with Eq. (10), ε_B is obtained with Eq. (12), L_{uw} is the portion of $L_u{}^t$ that originates from scattering within the water column and L_{uB} is the portion of $L_u{}^t$ that originates at the seafloor ($L_{uB} + L_{uw} = L_u{}^t$). The ratios ($L_{uw}/L_u{}^t$) and ($L_{uB}/L_u{}^t$) can be computed with a numerical radiative transfer code such as Hydrolight (Sequoia Scientific, Bellevue, Washington). Alternatively, ($L_{uw}/L_u{}^t$) and ($L_{uB}/L_u{}^t$) can be approximated with

$$\frac{L_{uw}(z_s)}{L_u{}^t(z_s)} = \frac{b_b \{1 - \exp[-a \chi z_d]\}}{b_b + (R_b a \mu_{0w} \chi - b_b) \exp[-a \chi z_d]} , \qquad (14)$$

where $z_d = z_{bot} - z_s$, $\chi = (1 + 1/\mu_{0w})$, and R_b is the seafloor albedo ($0 < R_b < 1$). Our derivation of Eq. (14) has been omitted for the sake of brevity. The value of R_b can be chosen either by selecting the appropriate value from published bottom reflectance spectra [6] or by esimating its value from a model of the measured light field [13].

In summary, the total error for a given incident illumination direction is given by Eq. (13), where ε_w is given by Eq. (10), ε_B is given by Eqs. (11) and (12), and the ratios $L_{uw}/L_u{}^t$ and $L_{uB}/L_u{}^t$ are either computed with a radiative transfer code or approximated with Eq. (14).

Equations (10) and (11) were derived for collimated illumination and low in-water scattering. However, these equations can be applied to more general and realistic conditions by computing a weighted average of the shading errors due to light incident on the instrument from various directions, i.e.,

$$\varepsilon = \sum_i w_i \varepsilon_i , \qquad (15)$$

where the weight w_i of each angular bin is proportional to the power of light incident at that directional bin. As a special case of this approach, Gordon and Ding [1] proposed taking the total shading error to be

$$\varepsilon = \varepsilon_{sky} f + (1 - f) \, \varepsilon_{sun}, \tag{16}$$

where ε_{sun} is the shading error computed for direct sunlight, ε_{sky} is the shading error of diffuse skylight, and f is the fraction of the total downwelling irradiance that is skylight. Numerically, the diffuse skylight error is approximately equal to that for direct sunlight at $\theta_0 = 35°$ [1]. Alternatively, values of f can be computed with a radiative transfer code, such as Hydrolight. Example values of f for use in Eq. (16) are provided by Baker and Smith [14]. For a submerged instrument it may also be necessary to account for in-water scattering when estimating the angular distribution of light incident on the instrument. Furthermore, in optically shallow waters it might be necessary to account for internal reflection at the sea surface. In the last two cases, one should estimate θ_{0w} directly for use in Eqs. (10) and (11) rather than with Eq. (2).

3. Assessment

Gordon and Ding [1] used Monte Carlo simulations to develop a semi-analytical model for the self-shading of a cylindrical radiometer far from the seafloor. This model, which we will hereafter refer to as the GD model, is simply Eq. (9) with the value of k replaced with a value determined empirically from their Monte Carlo results. This value of k depends on the illumination conditions and on the size and angular response of the sensor. The GD model was verified in field experiments by Zibordi and Ferrari [9] and by Aas and Korsbø [10] and is endorsed by the ocean optics protocols for SeaWiFS validation [8]. We therefore use this as a starting point for evaluation of our more general analytical model. Table 1 shows values of k obtained three different ways: with $k = 2/\tan\theta_{0w}$ (as derived analytically by Gordon and Ding [1]), with our analytical result of $k = (1/\tan\theta_{0w} + 1/\sin\theta_{0w})$, and from the empirically derived values of the GD model for a point sensor. The values $k = (1/\tan\theta_{0w} + 1/\sin\theta_{0w})$ agree with the numerical results better than do $k = 2/\tan\theta_{0w}$, especially at large solar zenith angles. It seems likely that the difference between the GD values of k for a point source and $k = (1/\tan\theta_{0w} + 1/\sin\theta_{0w})$ is due primarily to the uncertainty in their Monte Carlo results. This assertion is based on the fact that the numerical values are slightly larger than the analytical values, whereas we would expect the opposite because the analytical model ignores the effects of scattering. In any case, our analytical values of k lie in between those of the GD model for a point sensor and those for a finite sensor (not shown in Table 1) and therefore provide a good general-purpose model for the self-shading of a unbuoyed radiometer far from the seafloor.

Table 1. Values of k [Eq. (9)] for a radiance point sensor

θ_0 (deg)	$k = 2/\tan\theta_{0w}$	$k = (1/\tan\theta_{0w} + 1/\sin\theta_{0w})$	k from numerical simulations [1]
10	15.28	15.35	16.58
20	7.56	7.69	8.43
30	4.96	5.16	5.54
40	3.65	3.91	4.18
50	2.86	3.18	3.39
60	2.36	2.72	2.84
70	2.03	2.44	2.48

Our assessment of the rest of our analytical model was performed with simulations from the backward Monte Carlo program described in Leathers et al. [2]. Many of our numerical

computations were done with the Hyper-TSRB in mind. The Hyper-TSRB measures above-water downwelling irradiance (E_d) and underwater upwelling radiance (L_u) at many spectral channels from 400-800 nm, from which remote sensing reflectance spectra can be computed. The upwelling radiance sensor has a radius of 0.045 m and is suspended 0.66 m below the sea-surface. The buoy has a diameter of 0.15 m, and the bottom of the buoy sits 0.12 m below the sea surface and 0.54 m above the upwelling radiance sensor. The angular response of the radiance sensor was provided by Satlantic; the effective FOV is approximately 8.5 deg.

Shown in Figs. 3 and 4 is the self-shading error for the Hyper-TSRB in optically deep water predicted by Eq. (10) and for the sensor head only predicted by Eq. (9). Also shown in Figs. 3 and 4 are values of Hyper-TSRB self-shading error computed with Monte Carlo simulations for $b/a = 1$. It can be seen that the buoy adds a significant amount of shading for solar zenith angles less than 15° but contributes no additional shading beyond that of the sensor head for $\theta_0 > 15°$. Our analytical model gives excellent agreement with the numerical results in all cases except for the combination of small solar zenith angle and high water scattering. (Note that in Figs. 3 and 4 the value of b is large when a is large.) This gives us great confidence in our analytical model for most practical purposes. It should be noted that the case of $\theta_0 < 15°$ is not common except near the equator; more importantly, the actual shading error is so large for the combination of small θ_0 and high water turbidity that measurements should not be collected at these times.

Fig. 3. Predictions of Hyper-TSRB self-shading in deep water versus water absorption: Monte Carlo calculations (triangles); analytical model for the Hyper-TSRB (solid line); and analytical model for the sensor head only (dashed lines). Error values are for direct sunlight from the solar zenith angles indicated. Analytical values assume negligible scattering; numerical results are for $b = a$.

Primarily for academic purposes we note that the disagreement between theory and numerical result at small solar zenith angle in Figs. 3 and 4 is due to the presence of scattering in the numerical simulations. The numerical results converge toward the theoretical values if the amount of scattering is decreased toward zero. As demonstrated by Gordon and Ding [1], scattering does not have a large effect on the self-shading of a unbuoyed radiometer. However, the contribution of the buoy to shading (which is primarily at small solar zenith angles) does depend significantly on the amount of scattering present since the buoy is separated by a fixed geometric distance away from the sensor. The dependence on scattering of Hyper-TSRB self-shading in optically deep water was quantified numerically by Leathers et al. [2]. It is possible to use such numerical results to make a semianalytical model for a

particular instrument that includes the effects of scattering. For example, we can develop a semi-analytical model that accounts for scattering in deep water as follows. From Eq. (10),

$$\varepsilon = 1 - \exp\left[-\left(1 + 1/\cos\theta_{0w}\right)a\left(z_0 - z_s\right)\right], \quad (17)$$

where z_0 is given by Eq. (1). Because the depth of the shadow is reduced by scattering, we can replace z_0 in Eq. (17) with the reduced shade depth

$$z_0' = r_d \exp\left(-k_1 b z_0\right), \quad (18)$$

where r_d is the radius of the shading disk (sensor head or buoy). Shown in Fig. 5 is the self-shading error versus scattering coefficient as computed with Eqs. (17) and (18) with $k_1 = 0.1$. This provides a good model for the shading of the Hyper-TSRB in optically deep water; however, to apply this model to another buoyed instrument it would be necessary to compute a new value of k_1.
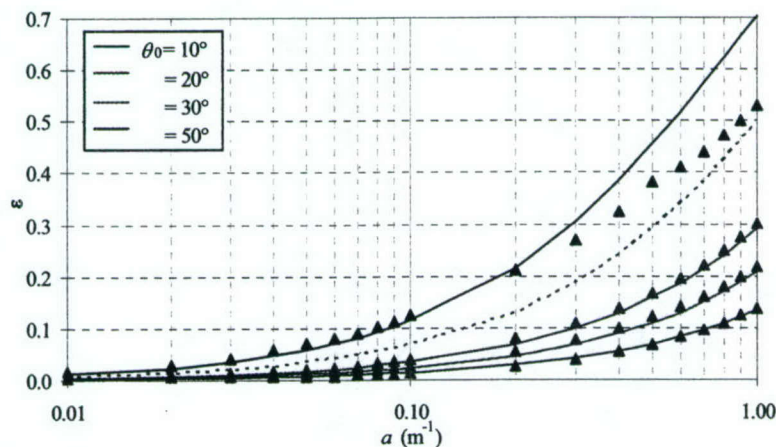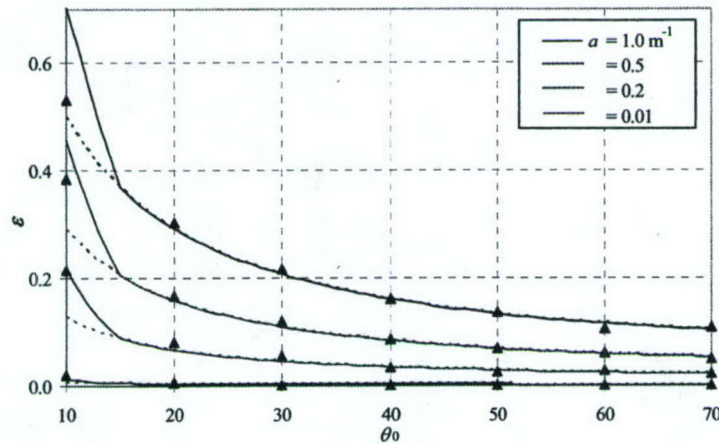

Fig. 4. Predictions of Hyper-TSRB self-shading in deep water versus sun position: Monte Carlo calculations (triangles); analytical model for the Hyper-TSRB (solid line); and analytical model for the sensor head only (dashed lines). Analytical values assume negligible scattering; numerical results are for $b = a$.
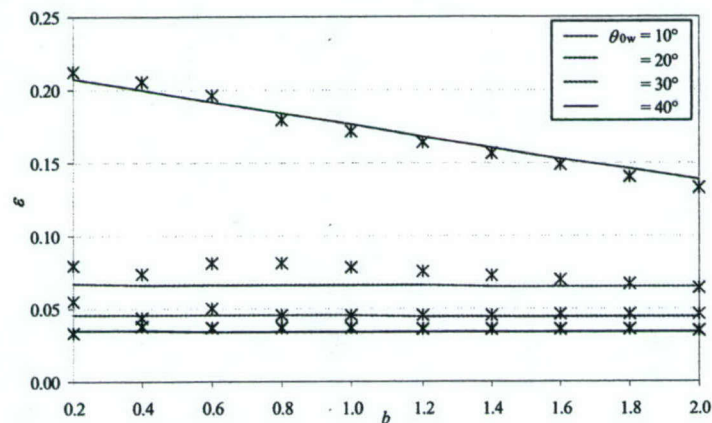
Fig. 5. Hyper-TSRB self-shading error versus scattering coefficient for $a = 0.02$ m^{-1}. Semi-analytical values (solid lines) were obtained with Eqs. (17) and (18) with $k_1 = 0.1$, and numerical results (asterisks) were computed with Backward Monte Carlo.

Figure 6 shows the Hyper-TSRB self-shading error plotted versus total water depth (z_{bot}) as computed by the full analytical model of Eqs. (13) and (14). Values are for $R_b = 0.2$ and $a = 0.2 \text{ m}^{-1}$ and for several different sun positions. Note that the Hyper-TSRB upwelling radiance sensor is 0.66 m below the surface, so the distance from the sensor to the seafloor is ($z_{bot} - 0.66$). Also shown in Fig. 6 are Hyper-TSRB self-shading error results from Monte Carlo simulations for $b/a = 2$. In very shallow water the radiance measurement is dominated by the component of light being reflected off the seafloor. If the instrument is very close to the seafloor, it mostly sees its own shadow. As the water depth is increased (i.e., the instrument is moved further from the bottom), the shading error in the radiance reflected off the bottom decreases, as does the overall shading error. However, as the water depth is further increased, the water-column component of the upwelling radiance begins to dominate and the overall shading error increases toward the optically deep values. The existence of a shading minimum located a short distance from the seafloor has also been found to occur for upwelling irradiance sensors [15].
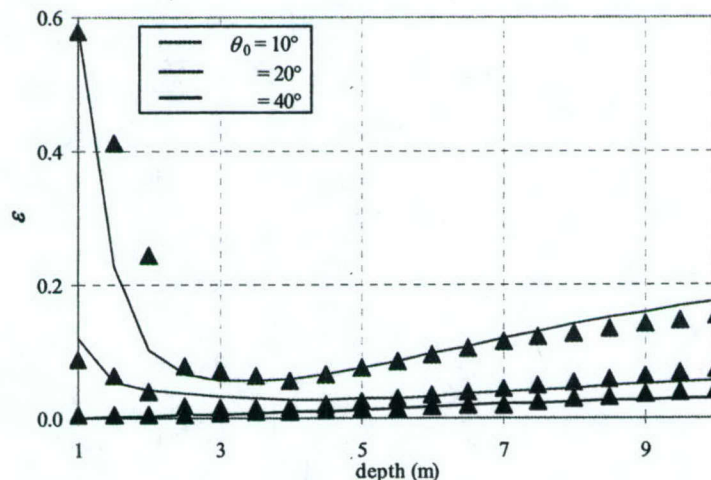
Fig. 6. Hyper-TSRB shading error as predicted with the analytical model compared with MC results (triangles). Results shown are for $a = 0.2 \text{ m}^{-1}$, $b = 0.4 \text{ m}^{-1}$, $R_b = 0.2$, FOV half-angle = 20°, and the indicated values of the solar zenith angle. The indicated depth is the total water depth; the sensor is 0.66 m below the sea surface.

The discrepancies in Fig. 6 between our analytical and numerical results at very small water depths is due primarily to the effects of internal reflection at the sea surface. When the water is very shallow, some of the sunlight experiences multiple reflections between the seafloor and the bottom of the sea surface, making the overall illumination on the instrument less collimated. This is taken fully into account in our Monte Carlo calculations, but not at all in the analytical results shown in Fig. 6. One can accommodate internal reflection in the analytical model in the same way that atmospheric scattering is accounted for [i.e., Eq. (15)]; however, this requires an estimate of the magnitude of the deviation of the in-water light from collimated.

4. Conclusions

Most commercially available instruments for measuring in-water upwelling radiance are large enough (i.e., with radii on the order of a few centimeters) that they suffer from significant self-shading error over at least some portion of the measured spectrum. The amount of error

depends on instrument dimensions, water optical properties, sun position, and atmospheric conditions, and in optically shallow water also depends on sensor FOV, water depth, and seafloor optical properties. Because radiometer self-shading is minimal when the water absorption coefficient is small, there may be a tendency to ignore its effect in optically clear waters. However, even in the clearest of waters the magnitude of the absorption coefficient is greater than 0.2 m^{-1} for wavelengths $\lambda > 600$ nm and greater than 0.65 m^{-1} for $\lambda > 700$ nm [12], which gives deep-water Hyper-TSRB shading errors of $\varepsilon > 20\%$ and $\varepsilon > 50\%$, respectively, for $\theta_0 = 10°$ and $\varepsilon > 5\%$ and $\varepsilon > 15\%$, respectively, for $\theta_0 = 30°$ [Eq. (10)].

The self-shading error for unbuoyed radiometers in optically deep waters can be well estimated with the semianalytical model of Gordon and Ding [1]. We have provided analytical justification for this model and have extended it to include the effects of a buoy on instruments such as the Hyper-TSRB. We have also provided a semianalytical model for the Hyper-TSRB in deep water that takes scattering into account. For most practical purposes, however, the effects of scattering can be ignored in optically deep water.

It is important to note that the Gordon and Ding model cannot be applied in situations where the seafloor has a significant effect on the measured radiance. We have developed an analytical model for estimating the self-shading of a buoyed on unbuoyed radiometer close to the seafloor [Eqs. (11) and (12)] and linked it with the deep-water model with Eq. (13). It should be noted that the shallow-water and deep-water models do not bound the shading error; Eq. (13) may exhibit an minimum versus depth.

The error values provided Eqs. (10) and Eq. (11) are for a collimated light incident at a particular direction. To compute the overall error for particular illumination conditions, it is necessary to properly weigh the error values from all directions [e.g., Eq. (16)], and in very shallow water it may be necessary to take internal reflection at the sea surface into account.

In general, the self-shading error can be more accurately determined with Monte Carlo calculations than with an analytical model. However, the analytical approach is more general and is easier to disseminate and implement. The disadvantage of the numerical approach is that it requires a specialized computer code and that a large number of computations must be performed for each instrument. It is impractical to expect experimental oceanographers to write Monte Carlo codes for this purpose; however, it may the reasonable to expect instrument manufacturers to begin providing self-shading correction look-up tables or software with their products.

A great utility of the analytical model is its ability to predict the amount of shading that will be encountered while an experiment is in its planning stage. Experiments should be planned so as to best avoid the collection of upwelling radiance measurements at times when self-shading is greatest. For a given suite of instrumentation, only the time of deployment (e.g., the position of the sun) can be adjusted, but this may be sufficient. If an experiment cannot accommodate the time restrictions, then it may be necessary to invest in the development of smaller sensors or deployment packages for these experiments. The analytical model developed in this paper also provides a tool for instrument design; the effects of sensor-head radius, buoy radius, and buoy position on self-shading are all easily computed. Finally it should be noted that self-shading prediction and correction (by either analytical model or empirical data) requires considerable knowledge of the environment (e.g., water properties, water depth, bottom albedo, and atmospheric conditions). Our analytical model can be used to compute the sensitivity of self-shading to uncertainties in the environmental parameters given a particular instrument's dimensions.

Appendix B.

An analytical model for subsurface irradiance and remote sensing reflectance in deep and shallow case-2 waters

A. Albert

German Aerospace Center (DLR), Remote Sensing Technology Institute, D-82230 Wessling,
Germany
andreas.albert@dlr.de

C.D. Mobley

Sequoia Scientific Inc., 2700 Richards Road, Suite 107, Bellevue, WA 98005 USA
mobley@sequoiasci.com

Abstract: Subsurface remote sensing signals, represented by the irradiance reflectance and the remote sensing reflectance, were investigated. The present study is based on simulations with the radiative transfer program Hydrolight using optical properties of Lake Constance (German: Bodensee) based on in-situ measurements of the water constituents and the bottom characteristics. Analytical equations are derived for the irradiance reflectance and remote sensing reflectance for deep and shallow water applications. The input of the parameterization are the inherent optical properties of the water - absorption $a(\lambda)$ and backscattering $b_b(\lambda)$. Additionally, the solar zenith angle θ_s, the viewing angle θ_v, and the surface wind speed u are considered. For shallow water applications the bottom albedo R_B and the bottom depth z_B are included into the parameterizations. The result is a complete set of analytical equations for the remote sensing signals R and R_{rs} in deep and shallow waters with an accuracy better than 4%. In addition, parameterizations of apparent optical properties were derived for the upward and downward diffuse attenuation coefficients K_u and K_d.

OCIS codes: (010.4450) Ocean optics; (010.7340) Water; (280.0280) Remote sensing

References and links

1. H.J. Gordon, O.B. Brown, and M.M. Jacobs, "Computed relationships between the inherent and apparent optical properties of a flat homogeneous ocean," Appl. Opt. **14**, 417-427 (1975).
2. L. Prieur, *Transfers radiatifs dans les eaux de mer*, PhD thesis (Doctorat d'Etat, Univ. Pierre et Marie Curie, Paris, 1976).
3. H.R. Gordon and A.Y. Morel, *Remote assessment of ocean color for interpretation of satellite visible imagery: a review* (Springer, New York, 1983), Vol. 4.
4. H.R. Gordon, O.B. Brown, R.H. Evans, J.W. Brown, R.C. Smith, K.S. Baker, and D.K. Clark, "A semianalytic radiance model of ocean color", J. Geoph. Res. **93**, 10909-10924 (1988).
5. J.T.O. Kirk, "Dependence of relationship between inherent and apparent optical properties of water on solar altitude," Limnol. Oceanogr. **29**, 350-356 (1984).
6. S. Sathyendranath and T. Platt, "Analytic model of ocean color," Appl. Opt. **36**, 2620-2629 (1997).
7. A.G. Dekker, H.J. Hoogenboom, L.M. Goddijn, and T.J.M. Malthus, "The relation between inherent optical properties and reflectance spectra in turbid inland waters," Rem. Sens. Rev. **15**, 59-74 (1997).
8. T. Heege, *Flugzeuggestützte Fernerkundung von Wasserinhaltsstoffen im Bodensee*, PhD thesis (Remote Sensing Technology Institute, German Aerospace Center DLR, 2000).

9. T.T. Bannister, "Model of the mean cosine of underwater radiance and estimation of underwater scalar irradiance," Limnol. Oceanogr. **37**, 773-780 (1992).
10. D.R. Lyzenga, "Passive remote sensing techniques for mapping water depth and bottom features," Appl. Opt. **17**, 379-383 (1978).
11. J. Joseph, "Untersuchungen über Ober- und Unterlichtmessungen im Meere und über ihren Zusammenhang mit Durchsichtigkeitsmessungen," Dt. Hydrogr. Z. **3**, 324-335 (1950).
12. W.D. Philpot and S.G. Ackleson, "Remote sensing of optically shallow, vertically inhomogeneous waters: a mathematical model", Delaware Sea Grant Collage Program (DEL-SG-12-81), 283-299 (1981).
13. S. Maritorena, A. Morel, and B. Gentili, "Diffuse reflectance of oceanic shallow waters: influence of water depth and bottom albedo", Limnol. Oceanogr. **39**, 1689-1703 (1994).
14. T. Ohde and H. Siegel, "Correction of bottom influence in ocean colour satellite images of shallow water areas of the Baltic Sea," Int. J. Rem. Sens. **22**, 297-313 (2001).
15. Z. Lee, K.L. Carder, C.D. Mobley, R.G. Steward, and J.S. Patch, "Hyperspectral remote sensing for shallow waters. 1. A semianalytical model," Appl. Opt. **37**, 6329-6338 (1998).
16. Z. Lee, K.L. Carder, C.D. Mobley, R.G. Steward, and J.S. Patch, "Hyperspectral remote sensing for shallow waters: 2. Deriving bottom depths and water properties by optimization," Appl. Opt. **38**, 3831-3843 (1999).
17. C.D. Mobley, B. Gentili, H.R. Gordon, Z. Jin, G.W. Kattawar, Á. Morel, P. Reinersman, K. Stamnes, and R.H. Stavn, "Comparison of numerical models for computing underwater light fields," Appl. Opt. **32**, 7484-7504 (1993).
18. C.D. Mobley, *Light and water - radiative transfer in natural waters* (Academic Press, San Diego, 1994).
19. P. Gege, "Characterization of the phytoplankton in Lake Constance for classification by remote sensing," Arch. Hydrobiol. Adv. Limnol. **53**, 179-193 (1998).
20. H. Buiteveld, J.H.M. Hakvoort, and M. Donze, "The optical properties of pure water," in *Ocean Optics XII*, Proc. SPIE 2258, 174-183 (1994).
21. A. Bricaud, A. Morel, and L. Prieur, "Absorption by dissolved organic matter of the sea (yellow substance)in the UV and visible domains," Limnol. Oceanogr. **26**, 43-53 (1981).
22. P. Gege, *Lake Constance: yellow substance measurements in 1998* Technical Report (Remote Sensing Technology Institute for Optoelectronics, German Aerospace Center DLR, 1999).
23. T.J. Petzold, *Volume scattering functions for selected ocean waters* (Dowden, Hutchinson & Ross, Stroudsberg, 1977), pp. 152-174.
24. D. Pozdnyakov, A. Lyaskovsky, H. Grassl, and L. Pettersson, "Numerical modelling of transspectral processes in natural waters: implications for remote sensing," Int. J. Rem. Sens. **23**, 1581-1607 (2002).
25. S.K. Hawes, K.L. Carder, and G.R. Harvey, "Quantum fluorescence efficiencies of fulvic and humic acids: effects on ocean color and fluorometric detection," in *Ocean Optics XI*, Proc. SPIE 1750,, 212-223 (1992).
26. T. Heege (Remote Sensing Technology Institute, German Aerospace Center DLR, Personal communication, 2003).
27. K. Bochter and C. Wallhäußer, "New instrument for simultaneous measurement of the daylight field's optical properties above and under water," in *Ocean Optics XIII*, Proc. SPIE 2963, 631-636 (1997).
28. W.W. Gregg and K.L. Carder, "A simple spectral solar irradiance model for cloudless maritime atmospheres," Limnol. Oceanogr. **35**, 1657-1675 (1990).
29. C. Cox and W. Munk, "Statistics of the sea surface derived from sun glitter," J. Mar. Res. **13**, 198-227 (1954).
30. C. Cox and W. Munk, "Measurement of the roughness of the sea surface from photographs of the sun's glitter," J. Opt. Soc. Am. **44**, 838-850 (1954).
31. H.R. Gordon, "Can the Lambert-Beer law be applied to the diffuse attenuation coefficient of ocean water?," Limnol. Oceanogr. **34**, 1389-1409 (1989).
32. J.T.O. Kirk, "The upwelling light stream in natural waters," Limnol. Oceanogr. **34**, 1410-1425 (1989).

1. Introduction

The concentration of water constituents can be derived by optical remote sensing making use of the spectral shape of the reflected sunlight. The models of [1], [2], or [3] for the irradiance reflectance and remote sensing reflectance, R and R_{rs}, use as parameters the absorption $a(\lambda)$ and backscattering coefficient $b_b(\lambda)$:

$$R_\infty = f^\circ \frac{b_b}{a+b_b} \equiv f^\circ x \qquad (1)$$

$$R_{rs,\infty} = f^\uparrow \frac{b_b}{a+b_b} \equiv f^\uparrow x = \frac{f^\circ}{Q} x \qquad (2)$$

The equations are valid just below the water surface. The higher the backscattering, the higher the reflectance and the higher the absorption, the lower the reflectance. f° is the proportionality factor for the irradiance reflectance and $f^\uparrow$ for the remote sensing reflectance of an infinitely deep water body (index ∞). The Q-factor is defined as the ratio of the upwelling irradiance and the upwelling radiance: $Q = \frac{E_u}{L_u}$. For an isotropic upwelling radiance distribution, $Q = \pi$ sr. Thus, the Q-factor is a measure of the anisotropy of the light field distribution. In natural waters, Q is typically around 5 sr. Using the definitions of the irradiance reflectance and remote sensing reflectance, $R = \frac{E_u}{E_d}$ and $R_{rs} = \frac{L_u}{E_d}$, the Q-factor is also the ratio of the irradiance reflectance to the remote sensing reflectance according to Eq. (2).

These approximations are valid for infinitely deep water, where only the water body contributes to the reflected signal. For open ocean case-1 waters, constant proportionality factors are commonly used and are sufficient for many applications, for example $f^\circ = 0.33$ [1] and $f^\uparrow = 0.095$ [4]. Due to the influences of the sun and surface geometry on the reflectances, a parameterization of the factors can be developed including these aspects and the inherent optical properties as well [5, 6]. But in case-2 waters, the factors f° and $f^\uparrow$ are not constant and can vary in time and location [7]. [8] used for his determination at Lake Constance (German: Bodensee) a combination of the model of [5] and [9].

In addition, if remote sensing data are analyzed including optically shallow waters, the bottom depth z_B and the bottom albedo R_B have to be taken into account [10]. Following [11], different authors including [12], [13], or [14] have formulated approximations of the irradiance reflectance for shallow water. Their equations result from a two-flow irradiance approximation including the bottom influences:

$$R = R_\infty \left(1 - e^{-2Kz_B}\right) + R_B e^{-2Kz_B}$$

K is the diffuse attenuation coefficient of the water column and is equal for the downward and upward directions. According to [15], this equation can be transformed to the remote sensing reflectance R_{rs} as follows:

$$R_{rs} = R_{rs,\infty} \left(1 - e^{-2Kz_B}\right) + \frac{R_B}{\pi} e^{-2Kz_B}$$

However, in reality the diffuse attenuation coefficients of the upwelling and downwelling light are not equal. To get a more accurate expression the effective attenuation coefficient is divided into an upwelling and a downwelling part. The upwelling part distinguishes between radiation reflected in the water column (index W) and from the bottom (index B). This results in the following equations, as mentioned in [15] and [16]:

$$R = R_\infty \left(1 - e^{-(K_d + K_{u,W})z_B}\right) + R_B e^{-(K_d + K_{u,B})z_B} \tag{3}$$

$$R_{rs} = R_{rs,\infty} \left[1 - \exp\left\{-\left(K_d + \frac{K_{u,W}}{\cos\theta_v}\right)z_B\right\}\right]$$
$$+ \frac{R_B}{\pi} \exp\left\{-\left(K_d + \frac{K_{u,B}}{\cos\theta_v}\right)z_B\right\} \tag{4}$$

The viewing angle just below the water surface, θ_v, is included in Eq. (4) in the upward attenuation due to the dependence of the upwelling radiance on the viewing position.

Based on these equations new analytical parameterizations were developed for the reflectances of deep and shallow water, the upwelling, and the downwelling attenuation coefficients to obtain an invertable equation for remote sensing data. Simulations were made with the well-established and validated radiative transfer program Hydrolight (version 3.1) [17, 18] for case-2 waters and the results fitted to Eq. (3) and (4). The program code was optimized for

the test site Lake Constance, located in southern Germany at the borders with Switzerland and Austria. The optical properties of Lake Constance were investigated by [19] and [8] and were included into the source code of Hydrolight. The simulations with Hydrolight were performed not only over the natural range of the concentrations of the water constituents found for Lake Constance, but also below and above this range to cover a more general range of concentrations. This extends the validity of the developed parameterizations for a wide number of case-2 waters.

2. Radiative transfer model

For the forward simulation of the underwater light field the radiative transfer program Hydrolight (version 3.1) was used. The model is explained in detail by [17] and [18]. The optical properties are selected for case-2 waters, such as the test site at Lake Constance, and are given for three kinds of water constituents: phytoplankton (index P), suspended matter (index X), and gelbstoff (index Y). Gelbstoff is also known as Colored Dissolved Organic Matter (CDOM), yellow substance, or gilvin. Thus, the total absorption and backscattering coefficients, $a(\lambda)$ and $b_b(\lambda)$, are the sums of all contributions of each water constitutent and pure water (index W) itself:

$$a(\lambda) = a_W(\lambda) + a_P(\lambda) + a_X(\lambda) + a_Y(\lambda)$$
$$b_b(\lambda) = b_{b,W}(\lambda) + b_{b,P}(\lambda) + b_{b,X}(\lambda) + b_{b,Y}(\lambda)$$

Due to the symmetric scattering properties of water, the backscattering coefficient of pure water can be determined from the scattering coefficient b_W: $b_{b,W} = \frac{1}{2}b_W$. The absorption $a_W(\lambda)$ and scattering coefficient $b_W(\lambda)$ of pure water are taken from [20]. The absorption and backscattering coefficients of phytoplankton and suspended matter are the product of the specific absorption and backscattering coefficients and the concentrations. The specific absorption of phytoplankton $a_P^*(\lambda)$ is given after [8] by the mean value of measurements of [19] at Lake Constance. Absorption of suspended matter was investigated for Lake Constance by [8]. He found no specific absorption and therefore a_X is set to zero. The absorption of gelbstoff is approximated by an exponential function [21] with an exponent $S = 0.014$ nm^{-1} at a reference wavelength λ_0 of 440 nm after [22]. The scattering in the water is mainly driven by the amount of suspended matter. The influence of the particulate fraction of phytoplankton on the scattering is included in the value of the scattering and backscattering coefficients of suspended matter as investigated by [8] and therefore, $b_{b,P} = 0$. There was also no dependence of the scattering and backscattering coefficients found at the wavelengths between 400 and 800 nm. Hence, the constant value of the specific backscattering coefficient of suspended matter $b_{b,X}^* = 0.0086$ m^2/g obtained for Lake Constance was used. The ratio of the specific scattering to backscattering coefficient is 0.019 [8], which is the same as found by [23] in San Diego harbor. Therefore, this phase function was chosen for all simulations. Gelbstoff is assumed not to scatter light because its pigments are totally dissolved in the water. Finally, the following equations are obtained for the absorption and the backscattering coefficients:

$$a(\lambda) = a_W(\lambda) + a_P^*(\lambda)C_P + a_Y(\lambda_0)e^{-S(\lambda-\lambda_0)} \qquad (5)$$
$$b_b(\lambda) = \frac{1}{2}b_W(\lambda) + b_{b,X}^*C_X \qquad (6)$$

C_P is the concentration of phytoplankton, which is given as the sum of chlorophyll-a and phaeophytin-a concentration in units of μg/l. C_X is the concentration of suspended matter in units of mg/l.

The impact of inelastic processes in natural water was recently investigated by [24] and found to contribute significantly to the irradiance reflectance and remote sensing reflectance. Hence,

the fluorescence of chlorophyll and gelbstoff as well as Raman scattering were included in all simulations using the default efficiencies of Hydrolight (version 3.1). The quantum efficiency of chlorophyll fluorescence was set to 2% and the emission function was approximated by a Gaussian function centered at the wavelength 685 nm with 10.6 nm full width at half maximum. The fluorescence of gelbstoff was described by the spectral fluorescence quantum efficiency function defined by [25] between 310 and 490 nm. The quantum efficiency took values of about 0.9 to 1.9% in this wavelength interval. The Raman scattering was approximated using a wavenumber redistribution function expressed by the sum of four Gaussian functions representing the number of shifts for a scattered photon. For more details see [18].

The water constituents are in general not homogeneously distributed with depth in natural waters. Thus, to match on average the real situations of the test site Lake Constance, depth profiles of the water constituents were included in all the simulations. More than 500 depth profiles were measured at Lake Constance between 1986 and 1996. The data were analyzed and mean profiles were determined for phytoplankton and suspended matter [8, 26]. The minimum concentration of phytoplankton was 1.0 $\mu g/l$ used for determining the depth profile. The dependence of the concentration on the depth z can be expressed as

$$C(z) = C_0 + C_{max} \exp\left\{-\frac{1}{2}\left(\frac{|z - z_{max}|}{\sigma}\right)^n\right\}$$ (7)

where $C(z)$ is the concentration of phytoplankton or suspended matter. For gelbstoff, no depth dependence was found. The values of the coefficients C_0, z_{max}, σ, and n are listed in table 1. If, for example, a constant value of the concentration for all depths is used, the irradiance reflectance is underestimated by 12 to 15% for concentrations of 2 to 5 $\mu g/l$ phytoplankton and 2 to 5 mg/l suspended matter.

Table 1. Values of the constant factors of phytoplankton and suspended matter for the depth profile in Eq. (7).

	C_0	z_{max} (m)	σ (m)	n
Phytoplankton	1.0 $\mu g/l$	2.9	9.6	3.0
Suspended matter	0.9 mg/l	12.9	10.7	2.3

For the simulations from 400 to 750 nm with steps of 5 nm, the concentrations of the water constituents at the surface were varied beyond their natural ranges at Lake Constance (see figures 1 and 2). The values are given in table 2. To get a suitable depth profile for the lowest concentrations of phytoplankton and suspended matter the coefficient C_0 in table 1 was adjusted to 0.5 $\mu g/l$ and 0.5 mg/l respectively.

Table 2. Concentrations of the water constituents for the simulations with Hydrolight.

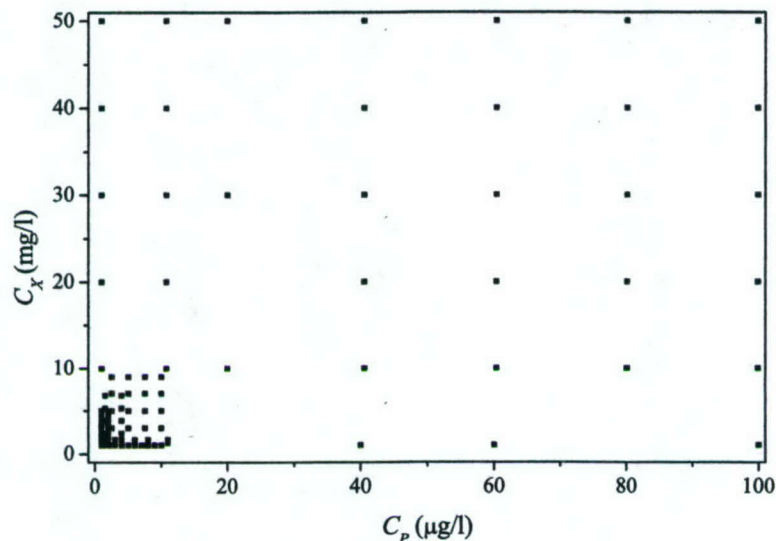| C_P ($\mu g/l$)	0.5	1.0	1.5	2.0	3.0	5.0	7.0	10.0
	20.0	40.0	60.0	80.0	100.0			
C_X (mg/l)	0.5	1.0	1.5	2.0	3.0	4.0	5.0	6.0
	7.0	9.0	10.0	30.0	50.0			
$a_Y(\lambda_0)$ (m^{-1})	0.05	0.10	0.15	0.20	0.30	0.40	0.50	0.60
	0.70	0.80	0.90	1.00	1.30	2.50	4.00	5.00

Fig. 1. Distribution of the concentration of suspended matter against phytoplankton for the simulations with Hydrolight.

For the bottom albedo, spectra of sand and green algae included in Hydrolight were used. Additionally, bottom albedo spectra were measured at Lake Constance for sediment and macrophyte covered beds with the Hydrological Spectral Radiometer HYDRA [27]. The sediment was gray colored mud consisting of about 50% inorganic particles and 50% organic matter typically for Lake Constance. The average particle size is around 10 μm. The reflectance of the macrophyte was measured above a patch of the species *Potamogeton Pectinatus* L. with senescent leaves. The bottom reflectances used for the simulations are shown in figure 3. Bottom depth was set to 1, 3, 6, 10, 20, 30 m, and infinitely deep water. For simulating the sun and sky conditions the model of [28] included in Hydrolight was used. Clear sky conditions were chosen with varying subsurface sun zenith angle θ_s. The angles were 8, 14, 21, 27, 34, 39, 43, and 46°. The forward simulations were performed for values of the surface wind speed u of 0, 5, and 10 m/s using the sea surface statistical model incorporated into Hydrolight. This surface representation is based on the wave-slope wind-speed laws of [29, 30] and thus includes both gravity and capillary wave effects.

Altogether, over 1400 spectra were simulated. The output of the Hydrolight simulations is given for different subsurface viewing angles θ_v ranging between 8° and 46° in the same manner as the sun zenith angle.

3. Results

The output of Hydrolight of the irradiance reflectance and remote sensing reflectance, R and R_{rs}, were investigated to find parameterizations for the inherent optical properties as well as for the sun and viewing geometry using Eq. (3) and (4). The unknown variables in these equations are the irradiance reflectance and remote sensing reflectance of the water body, R_∞ and $R_{rs,\infty}$, and the diffuse attenuation coefficients K_d, $K_{u,W}$, and $K_{u,B}$. For each of these unknown
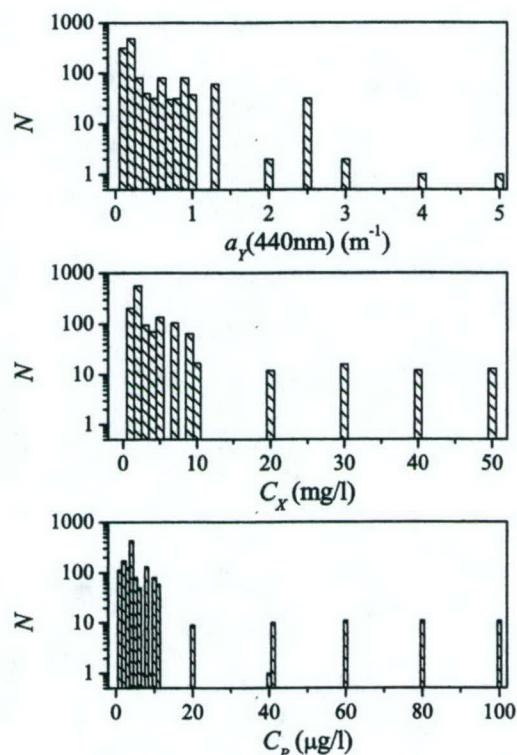
Fig. 2. Distribution of the concentration values of gelbstoff (top), suspended matter (center), and phytoplankton (bottom) for the simulations with Hydrolight.

factors new parameterizations were developed based on the inherent optical properties, the solar and viewing angles, and the surface wind speed. Wavelength dependence was included in the inherent optical properties. For all simulations chlorophyll and gelbstoff fluorescence was considered as mentioned above. For the determination of the parameterizations, wavelengths around the strongly peaked fluorescence emission of chlorophyll from 660 to 715 nm were excluded to give a better spectral fit. The parameterizations were generated by fitting the simulated values using the Levenberg-Marquardt multivariate optimization technique yielding regression coefficients. These regression coefficients allow calculation of the reflectances and attenuation coefficients using analytical equations. The mean relative error $\overline{\delta}$ documents the accuracy of the analytical parameterizations and was estimated by

$$\overline{\delta} = \frac{X - X_0}{X_0} = \frac{\Delta X}{X_0},$$

where X represents the value calculated by the parameterization and X_0 the value of the simulation.

Fig. 3. Bottom reflectance spectra used for the forward simulations in Hydrolight.

3.1. Deep water

3.1.1. Irradiance reflectance

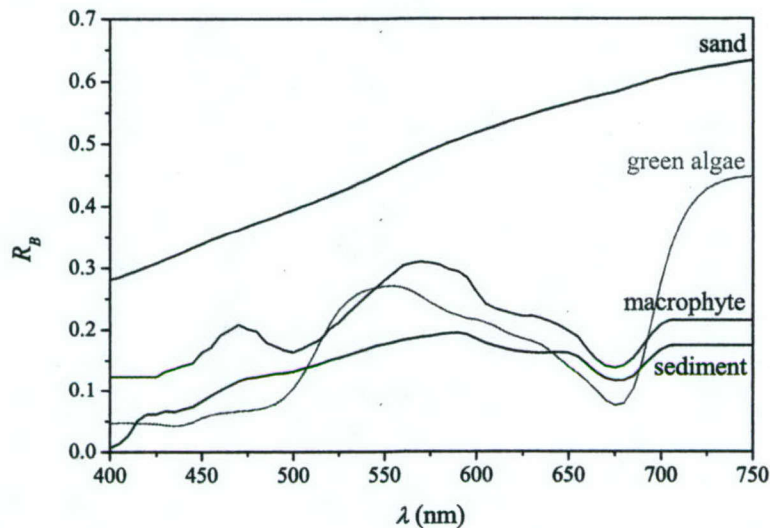The underwater irradiance reflectance for deep water R_∞ at depth $z = 0$ is parameterized using Eq. (1). The factor f° was analyzed for its dependence on x, u, and θ_s. The simulations yield a non-linear dependence on the factor x (Fig. 4) and the subsurface solar zenith angle θ_s (Fig. 5 right) and a linear dependence on the surface wind u (Fig. 5 left). For the investigation of the dependence on surface wind, additional calculations were made for wind speed values ranging from 0 to 30 m/s in steps of 1 m/s. The following parameterization was found to be suitable:

$$
\begin{aligned}
R_\infty &= f^\circ(x, \theta_s, u)x = f^\circ(x)f^\circ(\theta_s)f^\circ(u)x \\
&= p_1 \left(1 + p_2 x + p_3 x^2 + p_4 x^3\right) \left(1 + p_5 \frac{1}{\cos\theta_s}\right)(1 + p_6 u)x
\end{aligned} \tag{8}
$$

Using fewer coefficients for the factor x results in a significantly lower correlation. The coefficients p_1 to p_6 were determined using $N = 22184$ model results. The results of the regression are listed in table 3. The errors of using a constant factor f° is illustrated by figure 4. The dashed line corresponds to the value of $f^\circ = 0.33$ by [1]. For high values of x, which means high backscattering or high concentration of suspended matter, the error increases up to 100%. With the new parameterization the error is reduced significantly. Figure 6 shows, on the left hand side, the calculated plotted against the simulated values. The black crosses are the estimated values with Eq. (8) and the blue points are the values derived by the previous model of [8]. The distribution of the relative error $\overline{\delta}$ between the simulated and predicted values of R_∞ with Eq. (8) (Fig. 6 right) shows a normal distribution with a mean value of 0.04 while the mean error using a constant $f^\circ = 0.33$ is -0.25. The new parameterization gives also much better results than models of [5] and [6] which include the sun zenith angle to estimate the factor f° (graph not shown). The previous model of [8] for Lake Constance results in a mean relative error of 0.08

(Fig. 6 right). But for irradiance reflectances greater than 20% the mean relative error is 0.22. For these situations of high backscattering due to high amount of suspended matter, the new parameterization results in a mean relative error below 1%.
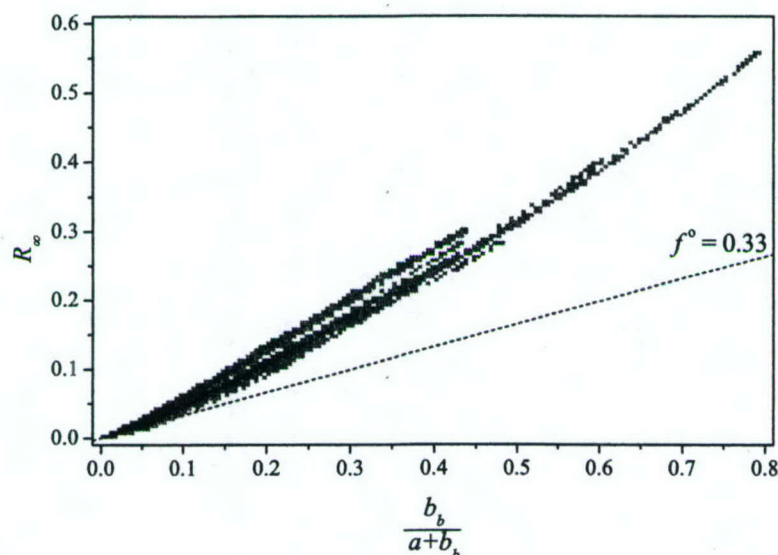

Fig. 4. Irradiance reflectance for infinitely deep water simulated with Hydrolight ($N = 22184$) depending on $x = \frac{b_b}{a+b_b}$ and the approximation of [1] for a factor $f^\circ = 0.33$ (dashed line).

The advantage of the new parameterization is the separation of the dependences on the inherent optical properties and the sun and surface geometry. This allows the influence of the variables on the remote sensing signal to be analyzed separately. The surface wind speed has the weakest influence. If it is neglected, the error is below 1%. The influence of the sun position is greater: the variation of the irradiance reflectance is about 15% for a subsurface solar zenith angle from 0 to 25° and about 30% for 0 to 40°.

3.1.2. Remote sensing reflectance

The determination of the remote sensing reflectance from the irradiance reflectance is possible using the Q-factor, $R_{rs,\infty} = \frac{R_\infty}{Q}$. The Q-factor is determined by the angular distribution of the light field under water. Therefore, a parameterization of $Q = Q(\theta_s, \theta_v, u)$ seemed to be suitable. All data points were analyzed, but no suitable parameterization was found. The reason is that the angular distribution of Q is controlled also significantly by the inherent optical properties and their concentrations: $Q = Q(\theta_s, \theta_v, u, x)$. Thus, an equation for the remote sensing reflectance in deep water was established that is similar to the equation for the irradiance reflectance, but with different values of the coefficients. The factor $f^\uparrow$ is derived as a function of separated variables. In addition to the dependences on x, θ_s, and u the remote sensing reflectance varies with the subsurface viewing angle θ_v. Simulations using different values of θ_v are shown in Fig. 7. The data points can be fitted with a function proportional to $\frac{1}{\cos\theta_v}$. The variation of the remote sensing reflectance is about 10% for a subsurface viewing angle from 0 to 25°. This is
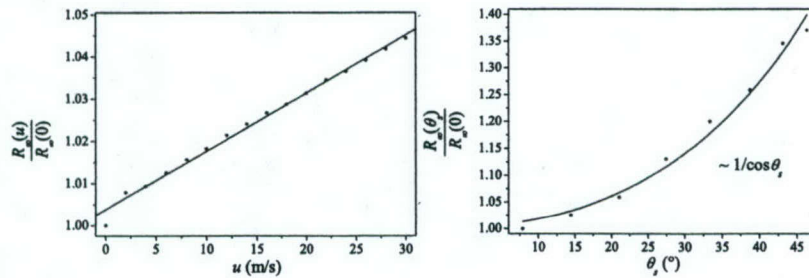
Fig. 5. Dependence of the irradiance reflectance for infinitely deep water on surface wind (left) and subsurface solar zenith angle (right). The concentrations of the water constituents are $C_P = 3$ µg/l, $C_X = 3$ mg/l, and $a_Y(\lambda_0) = 0.2 \text{m}^{-1}$.
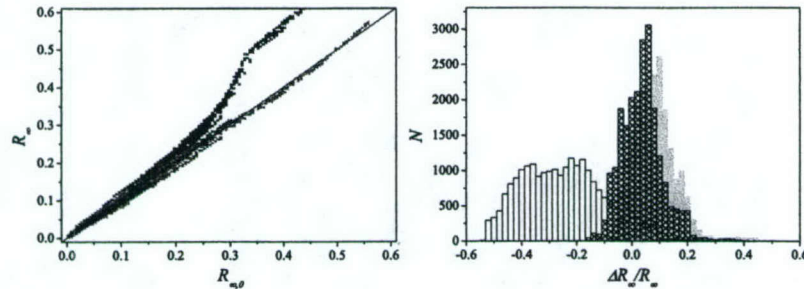
Fig. 6. Left: irradiance reflectance calculated by Eq. (8) (black crosses) and by the model of [8] (blue points) against the simulated values for infinitely deep water. The 1:1 line is plotted in red. Right: distribution of the relative errors for the approximation of [1] (white bars), [8] (gray bars), and of the new parameterization of Eq. (8) (cross hatched bars).

accounted for using the following parameterization:

$$
\begin{aligned}
R_{rs,\infty} &= f^\uparrow(x,\theta_s,u,\theta_v)x = f^\uparrow(x)f^\uparrow(\theta_s)f^\uparrow(u)f^\uparrow(\theta_v)x \\
&= p_1\left(1 + p_2x + p_3x^2 + p_4x^3\right) \\
&\quad \times \left(1 + p_5\frac{1}{\cos\theta_s}\right)(1 + p_6u) \\
&\quad \times \left(1 + p_7\frac{1}{\cos\theta_v}\right)x
\end{aligned}
\tag{9}
$$

The results of the regression are listed in table 3. $N = 177472$ model results were used to calculate the coefficients of the equation. Figure 8 shows the calculated values plotted against the simulated. The mean relative error is about 0.02.
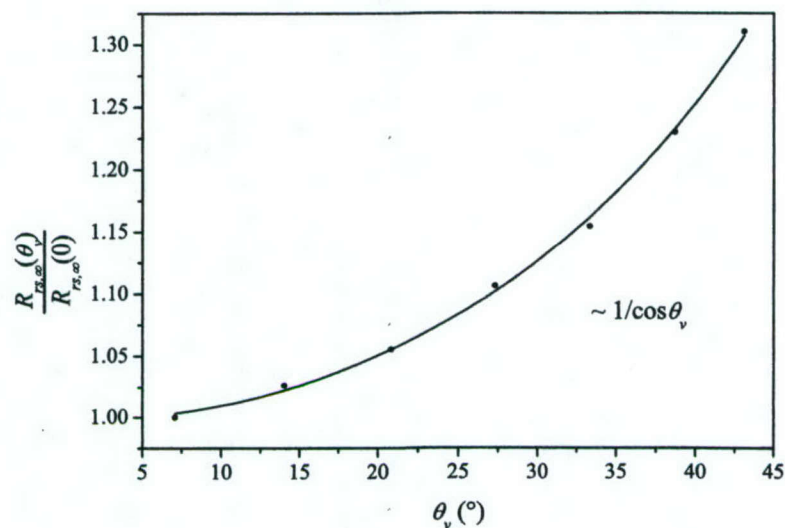
Fig. 7. Dependence of the remote sensing reflectance for infinitely deep water on the subsurface viewing angle θ_v. The concentrations of the water constituents are $C_P = 3$ μg/l, $C_X = 3$ mg/l, and $a_Y(\lambda_0) = 0.2\text{m}^{-1}$.

Table 3. Coefficients for the irradiance reflectance of deep water for Eq. (8) and for the remote sensing reflectance of deep water for Eq. (9).

	R_∞ of Eq. (8)	$R_{rs,\infty}(\text{sr}^{-1})$ of Eq. (9)
p_1	0.1034 ± 0.0014	$0.0512 \pm 0.0001 \text{ sr}^{-1}$
p_2	3.3586 ± 0.0305	4.6659 ± 0.0174
p_3	-6.5358 ± 0.0808	-7.8387 ± 0.0434
p_4	4.6638 ± 0.0649	5.4571 ± 0.0345
p_5	2.4121 ± 0.0443	0.1098 ± 0.0018
p_6 (s/m)	-0.0005 ± 0.0001	-0.0044 ± 0.0000
p_7	-	0.4021 ± 0.0020

3.2. Diffuse attenuation coefficient

The reflectances of deep water are the input for the shallow water Eq. (3) and (4). To employ these equations it is necessary to estimate the diffuse attenuation coefficients. The diffuse attenuation describes the loss of up- and downwelling irradiance within a thin layer in the water. This loss depends on absorption, scattering, and the isotropy of the light field. The latter is parameterized by the mean cosine $\overline{\mu}$. For a totally isotropic light distribution $\overline{\mu}$ is 0 and for a collimated beam in direction θ the mean cosine has the value $\overline{\mu} = \cos\theta$ (see [18] for example). In clear sky conditions, just below the water surface the distribution of the light is mainly affected by the direct beam of the sun. Thus, the mean cosine is approximately the cosine of the subsurface solar zenith angle θ_s in the upper water layers.
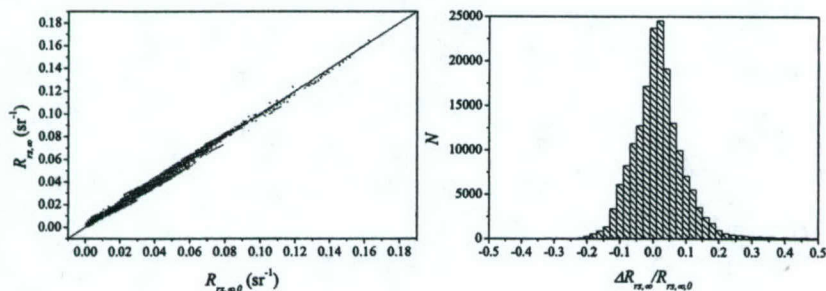
Fig. 8. Left: remote sensing reflectance calculated by Eq. (9) against the simulated values for infinitely deep water. The 1:1 line is plotted in red. Right: distribution of the relative errors.

3.2.1. Downward diffuse attenuation

K_d depends on the absorption and backscattering as well as on the solar zenith angle as shown in figure 9 (left). After [31], the parameterization for K_d is

$$K_d = \kappa_0 \frac{a + b_b}{\cos \theta_s} \tag{10}$$

The simulated values of K_d range from about 0.1 m^{-1} to 10.6 m^{-1} with a mean value of 0.7 m^{-1}. The regression of $N = 72558$ data points gives a value of $\kappa_0 = 1.0546 \pm 0.0001$. The mean relative error is $\overline{\delta} = -0.01$. The distribution of the relative errors is shown in figure 9 (right).
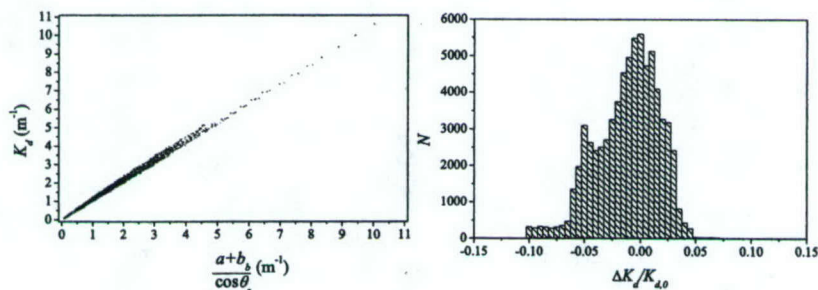
Fig. 9. Downward diffuse attenuation coefficient of 72558 simulations with Hydrolight. Left: dependency on $\frac{a+b_b}{\cos \theta_s}$. Right: distribution of the relative errors between calculated and simulated values.

3.2.2. Upward diffuse attenuation

The investigation on the upwelling diffuse attenuation coefficient is first done for the infinitely deep water body to find the best parameterization. Figure 10 shows the dependence of K_u on

absorption and backscattering (left) and on the subsurface solar zenith angle (right). The graph on the right hand side indicates the following dependence of K_u on the subsurface solar zenith angle θ_s: $K_u \propto \frac{1}{\cos \theta_s}$. On the left hand side the dependence on absorption and backscattering is plotted. The colors indicate the concentration of suspended matter C_X which is directly linked to the backscattering coefficient as described in Eq. (6). Generally, a linear dependence on the sum of absorption and backscattering can be assumed: $K_u \propto (a + b_b)$. However, for concentrations of suspended matter of $C_X < 3.0$ mg/l the relationship differs increasingly from a linear dependence. The upward diffuse attenuation coefficient takes higher values for a lower amount of scattering particles in the water. This is because few photons are scattered upwards, resulting in an anisotropic light field [32]. To correct for this effect an additional term is included depending on $x = \frac{b_b}{a+b_b}$. The following equation for the upward diffuse attenuation coefficient shows the best fit when used in Eq. (3) and (4).

$$K_u = (a+b_b)(1+x)^{\kappa_1} \left(1 + \kappa_2 \frac{1}{\cos \theta_s}\right) \tag{11}$$

For the simulations of an infinitely deep water body the mean relative error was $\overline{\delta} = 0.13$ for $N = 22184$ points. To separate the influence of photons reflected by the water column and the bottom, two different upward diffuse attenuation coefficients, $K_{u,W}$ and $K_{u,B}$, are used for shallow water applications. Thus, four coefficients $\kappa_{i,W}$ and $\kappa_{i,B}$ with $i = 1, 2$ were determined by fitting the entire Eq. (3) and (4). The results of the regression are given in table 4. Since the output of Hydrolight is the total upward diffuse attenuation coefficient, which is not the sum of $K_{u,W}$ and $K_{u,B}$, no mean relative errors can be specified.
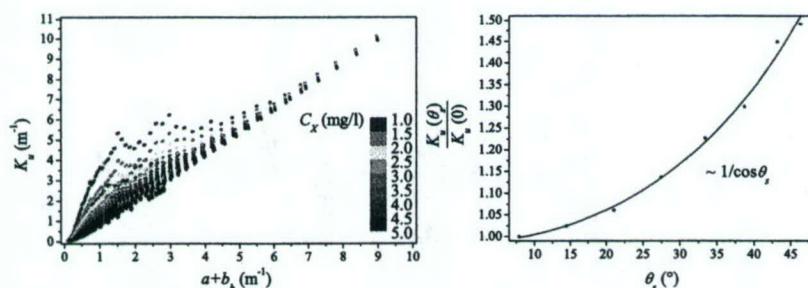
Fig. 10. Dependency of the upward diffuse attenuation coefficient on the sum of absorption and backscattering (left) and subsurface solar zenith angle (right). The points on the left are for $\theta_s = 8°$ with colors representing the concentration of suspended matter and the curve on the right is for $C_P = 1$ μg/l, $C_X = 1$ mg/l, and $a_Y(\lambda_0) = 0.2 \text{m}^{-1}$.

3.3. Shallow water

Putting all the above results together the shallow water reflectances can be calculated using Eq. (3) and (4). Additional coefficients A_1 and A_2 are introduced to adapt the equations to the simulated situations.
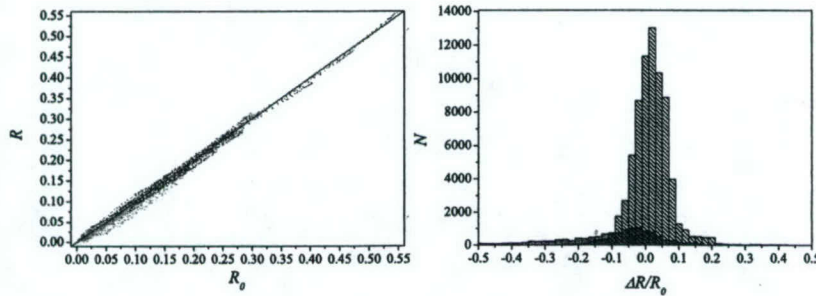
Fig. 11. Irradiance reflectance of shallow water. Comparison of simulated values R_0 and estimated values R (left) with the 1:1 line in red; the green points are the values for wavelengths from 660 to 715 nm. Distribution of the relative error between simulated and estimated irradiance reflectances.

3.3.1. Irradiance reflectance

With the new parameterizations of the diffuse attenuation coefficients and the factors A_1 and A_2, the irradiance reflectance can be expressed by

$$
\begin{aligned}
R &= R_\infty \left[1 - A_1 \exp\left\{ -\left(\frac{\kappa_0}{\cos\theta_s} + (1+x)^{\kappa_{1,W}} \left(1 + \frac{\kappa_{2,W}}{\cos\theta_s} \right) \right) (a + b_b) z_B \right\} \right] \\
&+ A_2 R_B \exp\left\{ -\left(\frac{\kappa_0}{\cos\theta_s} + (1+x)^{\kappa_{1,B}} \left(1 + \frac{\kappa_{2,B}}{\cos\theta_s} \right) \right) (a + b_b) z_B \right\}
\end{aligned}
\tag{12}
$$

The values of A_1 and A_2 were determined by fitting $N = 72558$ simulated data points. The resulting coefficients are listed in Table 4. In Fig. 11 the estimated irradiance reflectance, R, is plotted against the simulated reflectance, R_0, for all cases. The distribution of the relative error - with a mean error of $\overline{\delta} = 0.02$ - is also shown in Fig. 11. For comparison, the original Eq. (3) of [13] using Eq. (8) for the irradiance reflectance of the water column gives a relative mean error of $\overline{\delta} = 0.06$.

The green points in Figure 11 are the values for wavelengths from 660 to 715 nm. Although these wavelengths were excluded for algorithm development due to the influence of chlorophyll fluorescence, the estimation with Eq. (12) using the parameters of Table 4 is in fair agreement with the simulated values. The mean relative error for these wavelengths is $\overline{\delta} = -0.12$. This means that the new parameterization can be applied also to these wavelengths with an underestimation of about 12%.

The spectral shape of three examples is shown in Fig. 12 in a range from 400 to 750 nm with the relative errors compared to the simulations of Hydrolight. The numbers in the figure correspond to the following conditions:

1. Bottom type is sediment at a depth of $z_B = 5$ m; the concentration of the water constituents are phytoplankton $C_P = 10.8 \, \mu g/l$, suspended matter $C_X = 50.0$ mg/l, and gelbstoff $a_Y(440\text{nm}) = 0.2 \, \text{m}^{-1}$; the subsurface solar zenith angle is $\theta_s = 27°$; the wind speed is $u = 1$ m/s.

2. Macrophytes at $z_B = 6$ m; $C_P = 2.5 \, \mu g/l$, $C_X = 7.0$ mg/l, and $a_Y(440\text{nm}) = 0.3 \, \text{m}^{-1}$; $\theta_s = 33°$; $u = 0$ m/s.

3. Sediment at $z_B = 5$ m; $C_P = 1.0$ µg/l, $C_X = 1.0$ mg/l, and $a_Y(440\text{nm}) = 0.05$ m^{-1}; $\theta_s = 27°$; $u = 1$ m/s.

The agreement between simulation and calculation with Eq. (12) is very good in each case. The relative error (Fig. 12: right) is below 5% over the entire spectral range, except for wavelengths around 685 nm. This is due to the fluorescence of chlorophyll which is not parameterized in these analytical equations. The differences in the other parts of the spectra are mainly caused by the fluorescence of gelbstoff which affects mostly the green part of the visible spectrum [24].
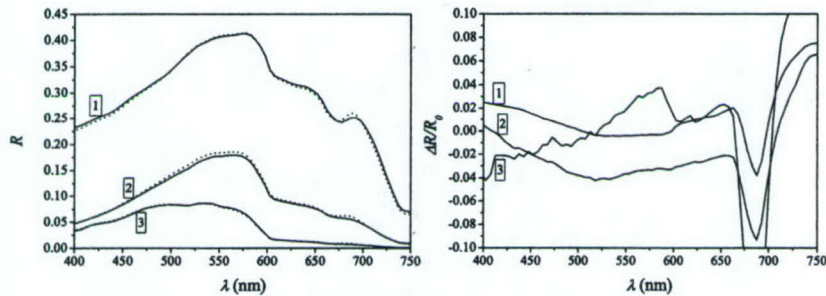
Fig. 12. Irradiance reflectance of shallow water for the spectral range from 400 to 750 nm for three different cases. Left: comparison of simulated (dotted lines) and estimated values (solid lines); right: relative errors. The numbers refer to the following situations: (1) sediment at $z_B = 5$ m, $C_P = 10.8$ µg/l, $C_X = 50.0$ mg/l, $a_Y(440\text{nm}) = 0.2$ m^{-1}, $\theta_s = 27°$, $u = 1$ m/s; (2) macrophytes at $z_B = 6$ m, $C_P = 2.5$ µg/l, $C_X = 7.0$ mg/l, $a_Y(440\text{nm}) = 0.3$ m^{-1}, $\theta_s = 33°$, $u = 0$ m/s; (3) sediment at $z_B = 5$ m, $C_P = 1.0$ µg/l, $C_X = 1.0$ mg/l, $a_Y(440\text{nm}) = 0.05$ m^{-1}, $\theta_s = 27°$, $u = 1$ m/s.

3.3.2. Remote sensing reflectance

The remote sensing reflectance R_{rs} can be expressed with a similar approximation as the irradiance reflectance, but with an additional dependence on the subsurface viewing angle θ_v.

$$
\begin{aligned}
R_{rs} = & \; R_{rs,\infty}\left[1 - A_1 \exp\left\{-\left(\kappa_0\frac{\cos\theta_v}{\cos\theta_s} + (1+x)^{\kappa_{1,W}}\left(1+\frac{\kappa_{2,W}}{\cos\theta_s}\right)\right)\frac{a+b_b}{\cos\theta_v}z_B\right\}\right] \\
& + A_2\frac{R_B}{\pi}\exp\left\{-\left(\kappa_0\frac{\cos\theta_v}{\cos\theta_s} + (1+x)^{\kappa_{1,B}}\left(1+\frac{\kappa_{2,B}}{\cos\theta_s}\right)\right)\frac{a+b_b}{\cos\theta_v}z_B\right\}
\end{aligned}
\tag{13}
$$

The results of the regression analysis of $N = 580464$ numbers of observations are listed in Table 4 below. Figure 13 shows the estimated against the simulated values and the relative error, with a mean error of $\bar{\delta} = 0.03$. For comparison, the equation of [15] gives a relative mean error of -0.09.

As mentioned for the case of the irradiance reflectance, the green points in Fig. 13 are the values for wavelengths from 660 to 715 nm. The correlation between the estimated and simulated values are very good here as well. The mean relative error for these wavelengths is $\bar{\delta} = -0.13$. This means that the new parameterization can be applied also to these wavelengths with an underestimation of about 13%.

Table 4. Coefficients for the irradiance and remote sensing reflectance of Eq. (12) and (13) for shallow water.

	R of Eq. (12)	$R_{rs}(\text{sr}^{-1})$ of Eq. (13)
A_1	1.0546 ± 0.0038	1.1576 ± 0.0014
κ_0	1.0546 ± 0.0001	1.0546 ± 0.0001
$\kappa_{1,W}$	1.9991 ± 0.0305	3.5421 ± 0.0152
$\kappa_{2,W}$	0.2995 ± 0.0122	-0.2786 ± 0.0030
A_2	0.9755 ± 0.0013	$1.0389 \pm 0.0004 \text{ sr}^{-1}$
$\kappa_{1,B}$	1.2441 ± 0.0209	2.2658 ± 0.0076
$\kappa_{2,B}$	0.5182 ± 0.0036	0.0577 ± 0.0009
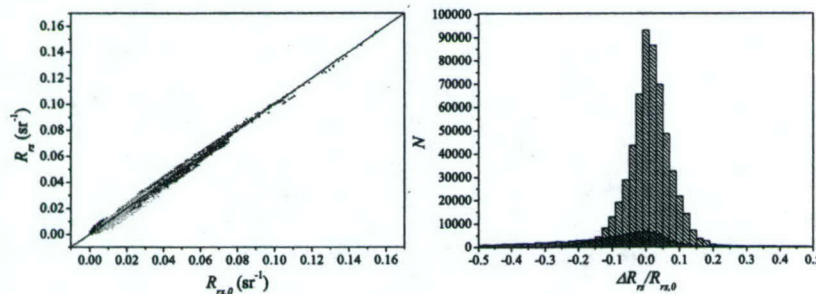
Fig. 13. Remote sensing reflectance of shallow water. Comparison of simulated values $R_{rs,0}$ and estimated values R_{rs} (left) with the 1:1 line in red; the green points are the values for wavelengths from 660 to 715 nm. Distribution of the relative error between simulated and estimated remote sensing reflectances.

The spectral shape of the remote sensing reflectance is shown in Fig. 14 in the same way as explained for the irradiance reflectance. Two graphs are included in the figure, one for a subsurface viewing angle of $\theta_v = 7°$ and one for $\theta_v = 27°$. The calculated values of the remote sensing reflectance agree very well with the simulations. The relative error is below 5% except for situation number 3, where the error is about 10% around 600 nm. The reason for the discrepancies is the same as for the irradiance reflectance, namely gelbstoff fluorescence.

4. Conclusions

New parameterizations of the irradiance reflectance and the remote sensing reflectance in deep and shallow waters were developed using only the inherent optical properties of the water, the viewing and solar zenith angle, and the surface wind speed. Additionally, a new parameterization for the upward diffuse attenuation coefficient was developed. The new model separates the dependences on inherent optical properties, wind speed, viewing, and solar zenith angle. Thus, their influences can be analyzed very easily. The irradiance reflectance and remote sensing reflectance can be calculated much faster using the analytical equations than with Hydrolight or Monte Carlo methods. The estimations of the irradiance reflectance and remote sensing reflectance agree significantly better with the simulations of Hydrolight than estimations with
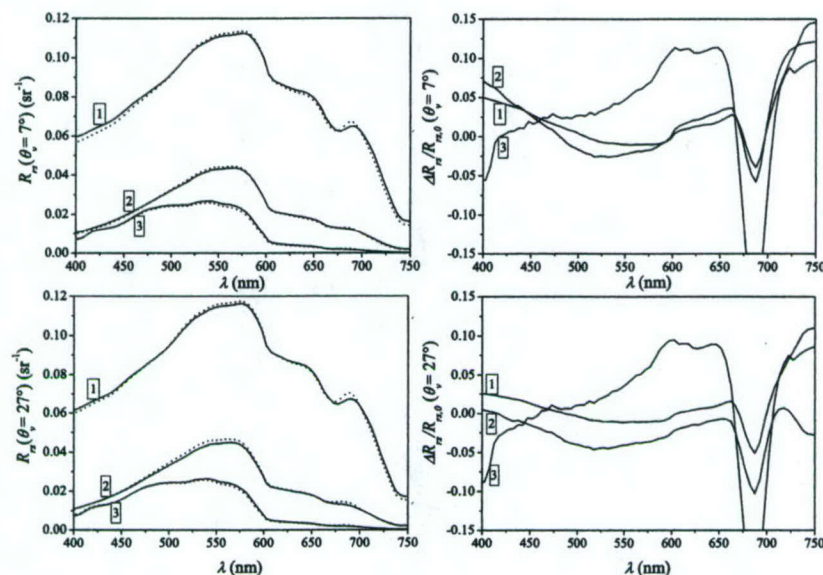
Fig. 14. Remote sensing reflectance of shallow water for the spectral range from 400 to 750 nm for three different cases and for a subsurface viewing angle of $\theta_v = 7°$ on the top and $\theta_v = 27°$ on the bottom. The left part shows the comparison of simulated (dotted lines) and estimated values (solid lines) and the right side the relative errors. The numbers refer to the following situations: (1) sediment at $z_B = 5$ m, $C_P = 10.8$ $\mu g/l$, $C_X = 50.0$ mg/l, $a_Y(440nm) = 0.2$ m^{-1}, $\theta_s = 27°$, $u = 1$ m/s; (2) macrophytes at $z_B = 6$ m, $C_P = 2.5$ $\mu g/l$, $C_X = 7.0$ mg/l, $a_Y(440nm) = 0.3$ m^{-1}, $\theta_s = 33°$, $u = 0$ m/s; (3) sediment at $z_B = 5$ m, $C_P = 1.0$ $\mu g/l$, $C_X = 1.0$ mg/l, $a_Y(440nm) = 0.05$ m^{-1}, $\theta_s = 27°$, $u = 1$ m/s.

existing equations. The mean error is about 2-3%. A maximum error of about 15% occurs at a wavelength of 685 nm owing to the fluorescence of chlorophyll which is not included in the system of equations presented here. The spectral shape of the simulations with Hydrolight fits very well with the new parameterizations. The relative error at a given wavelength is below 5% for the irradiance reflectance and below 10% for the remote sensing reflectance from 400 to 750 nm. Main error sources are the fluorescence of chlorophyll and gelbstoff.

Seasonal changes of the specific optical properties of the water constituents of Lake Constance were investigated previously. The variability of the specific absorption of phytoplankton was analyzed by [19]. He has separated five different algae classes, which allow to model changes of the optical properties of phytoplankton in deep water from 1990 through 1992. The impact on reflectance spectra is small compared to concentration changes. The specific backscattering of suspended matter was determined by [8]. He observed an accuracy of about 25% for the estimated concentration of suspended matter from airborne remote sensing data compared to in situ measurements, indicating a low variability of the specific backscattering coefficient of suspended matter. The gelbstoff exponent S varies about 8% after [22].

With the new parameterizations a set of equations was found for case-2 waters, like Lake Constance. This improves upon existing equations for determining the concentration of the water constituents, bottom depth, and bottom types using by inversion techniques. The analytical

equations provide a fast method to process a large set of remote sensing data from hyperspectral airborne and spaceborne sensors. The next step is to implement analytical equations of the fluorescence of chlorophyll and gelbstoff and to test the equations using an independent dataset from Lake Constance and other locations. Inclusion of surface effects and bidirectional bottom effects are also planned.

Acknowledgments

Propagation and Perception of Bioluminescence: Factors Affecting Counterillumination as a Cryptic Strategy

SÖNKE JOHNSEN[1,*], EDITH A. WIDDER[2], AND CURTIS D. MOBLEY[3]

[1]*Biology Department, Duke University, Durham, North Carolina 27708;*
[2]*Marine Science Division, Harbor Branch Oceanographic Institution, Ft. Pierce, Florida 34946;*
and [3]*Sequoia Scientific Inc., Bellevue, Washington 98005*

Abstract. Many deep-sea species, particularly crustaceans, cephalopods, and fish, use photophores to illuminate their ventral surfaces and thus disguise their silhouettes from predators viewing them from below. This strategy has several potential limitations, two of which are examined here. First, a predator with acute vision may be able to detect the individual photophores on the ventral surface. Second, a predator may be able to detect any mismatch between the spectrum of the bioluminescence and that of the background light. The first limitation was examined by modeling the perceived images of the counterillumination of the squid *Abralia veranyi* and the myctophid fish *Ceratoscopelus maderensis* as a function of the distance and visual acuity of the viewer. The second limitation was addressed by measuring downwelling irradiance under moonlight and starlight and then modeling underwater spectra. Four water types were examined: coastal water at a depth of 5 m and oceanic water at 5, 210, and 800 m. The appearance of the counterillumination was more affected by the visual acuity of the viewer than by the clarity of the water, even at relatively large distances. Species with high visual acuity (0.11° resolution) were able to distinguish the individual photophores of some counterilluminating signals at distances of several meters, thus breaking the camouflage. Depth and the presence or absence of moonlight strongly affected the spectrum of the background light, particularly near the surface. The increased variability near the surface was partially offset by the higher contrast attenuation at shallow depths, which reduced the sighting distance of mismatches. This research has implications for the study of spatial resolution, contrast sensitivity, and color discrimination in deep-sea visual systems.

Introduction

Counterillumination is a common form of crypsis in the open ocean (Latz, 1995; Harper and Case, 1999; Widder, 1999). Its prevalence is due to the fact that, because the downwelling light is orders of magnitude brighter than the upwelling light, even an animal with white ventral coloration appears as a black silhouette when viewed from below (Johnsen, 2002). This is particularly disadvantageous because an object is detectable at a far greater distance when viewed from below than when viewed from any other angle (Mertens, 1970; Johnsen, 2002). Aside from extremely transparent tissue, which is not easy to achieve in larger species with complex tissues, the way to overcome this disadvantage is for the ventral surface to emit light that matches the downwelling light in intensity, spectrum, and angular distribution. Indeed, this solution is nearly ubiquitous in nontransparent mesopelagic species, particularly in crustaceans, fish, and squid (Young and Roper, 1976; Herring, 1977, 1985; Widder, 1999).

Counterilluminating species have evolved complex strategies to match the intensity, spectrum, and angular distribution of the downwelling light (Denton *et al.*, 1972; Young and Mencher, 1980; Herring, 1983; Widder, 1999). One aspect that is poorly understood, however, is the spatial distribution of the photophores (Young and Roper, 1976). While some species (*e.g.*, the cookie cutter shark *Isistius*

Abbreviations: MTF, modulation transfer function; OTF, optical transfer function; PSF, point spread function.

1

brasiliensis) have many small photophores that evenly illuminate the ventral surface, most have a smaller number of isolated photophores that produce uneven illumination (*e.g.,* Fig. 2d). Thus, even if the photophores match the spectrum and intensity of the downwelling light perfectly, the counterilluminator will be visible when viewed at a distance that allows these individual sources to be discerned. To investigate this problem, the effects of the intervening water and the viewer's visual acuity on the perceived image of the counterillumination must be understood.

This study examines the effects of underwater light scattering and visual acuity on the perceived images of counterillumination signals. The effects are modeled with Monte Carlo methods and image transfer theory, using data collected from water types ranging from shallow coastal water to the deep mesopelagic zone (800 m). Three visual systems, with high, medium, and low acuity, are also examined. The goal is to determine under which conditions counterilluminators are still visible and what implications this has for both camouflage and visual detection under low-light conditions.

Materials and Methods

General principles of image transfer

The perceived image of a counterilluminating animal viewed from a distance is affected by three factors: absorption and scattering by the water and the acuity of the viewer's eye. The water and associated particulates potentially dim and blur the image, and the acuity of the eye determines the resolution of the perceived image.

The effect of the first factor is generally modeled in the following way. First, the optical effects of the water on the image of a point source are calculated. The image of a point source is known as the point spread function (PSF) (Mertens and Replogle, 1977). The point source is then convolved with a given image to determine the appearance of the image after it passes through the water. In a convolution, each point in the image is replaced by its product with the point spread function (Fig. 1). Fortunately, this computationally expensive procedure can be streamlined using the convolution theorem, which states that for any two images I_1 and I_2, the convolution of I_1 with I_2 is equal to the inverse Fourier transform of the product of the Fourier transforms of the two images: that is,

$$I_1 * I_2 = \mathcal{F}^{-1}[\mathcal{F}(I_1) \cdot \mathcal{F}(I_2)], \quad \text{(Fig. 1)} \quad \text{(Equation 1)}$$

where * denotes convolution, and $\mathcal{F}(I)$ and $\mathcal{F}^{-1}(I)$ are the Fourier and inverse Fourier transforms of an image I (Goodman, 1996). Let I_1 be the image of the counterillumination, and I_2 be the point spread function. Substituting into equation (1) gives

$$\text{image} * \text{PSF} = \mathcal{F}^{-1}[\mathcal{F}(\text{image}) \cdot \mathcal{F}(\text{PSF})]. \quad \text{(Equation 2)}$$

The Fourier transform of the point spread function is gen-
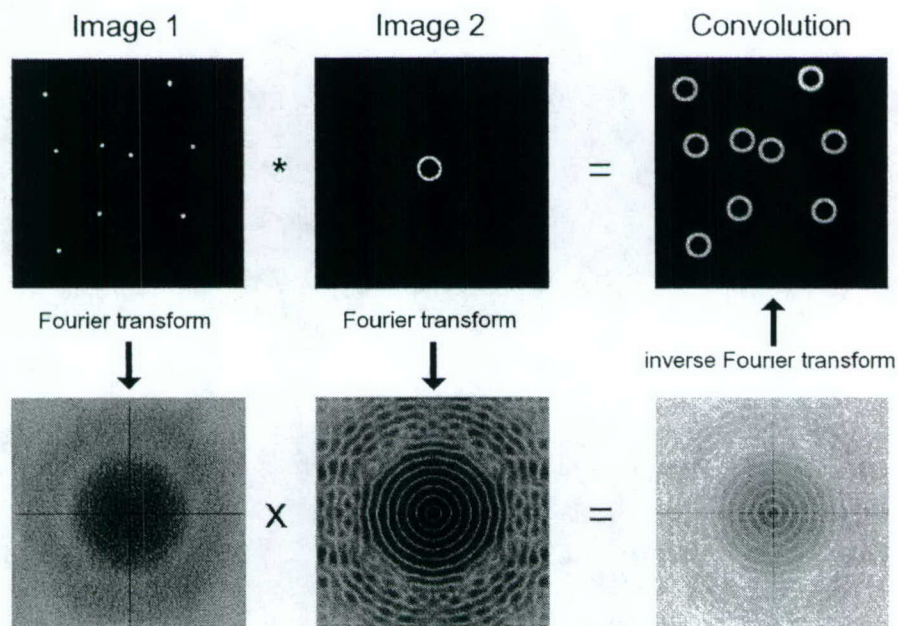
Figure 1. The convolution of image 1 and image 2 (denoted by the "*" operator) can be calculated by multiplying the Fourier transforms of the two images and then calculating the inverse Fourier transform of the product.

erally referred to as the optical transfer function (OTF). Due to the convolution theorem, the OTF of a whole system is simply the product of the OTFs of the various components in the system (Goodman, 1996). Thus, for this study

$$\text{image}_{\text{final}} = \mathscr{F}^{-1}[\mathscr{F}(\text{image}_{\text{initial}}) \cdot \text{OTF}_{\text{water}} \cdot \text{OTF}_{\text{eye}}],$$

(Equation 3)

where $\text{image}_{\text{final}}$ is the perceived image and $\text{OTF}_{\text{water}}$ and OTF_{eye} are the optical transfer functions of the water and eye respectively. A final, convenient implication of the convolution theorem is that the OTF of x meters of optically homogeneous water is equal to the OTF of 1 meter of water to the xth power. Thus, one need only calculate the PSF for one distance. This property, known as the linearity assumption, does not hold in extreme cases (*e.g.*, very large x), but is appropriate for the situations examined in this study (Jaffe, 1992). The equation for underwater image transfer is then

$$\text{image}_{\text{final}}(x) = \mathscr{F}^{-1}[\mathscr{F}(\text{image}_{\text{initial}}) \cdot (\text{OTF}_1)^x \cdot \text{OTF}_{\text{eye}}],$$

(Equation 4)

where $\text{image}_{\text{final}}(x)$ is the perceived image viewed from a distance of x meters, and OTF_1 is the optical transfer function of the water over a distance of 1 meter.

Although Eq. (4) correctly describes the propagation of a two-dimensional image, it requires modification when used in the context of counterillumination, because the background radiance is affected by the entire three-dimensional light field and changes as the viewer moves down and away from its target. From Mertens (1970), the degradation of contrast of a large image underwater (*i.e.*, the OTF at zero spatial frequency) is

$$\text{OTF}(0) = \frac{C_x}{C_0} = e^{-(c - K_L)x}, \quad \text{(Equation 5)}$$

where C_x and C_0 are contrast at x and 0 meters viewing distance, c is the beam attenuation coefficient, and K_L is the attenuation coefficient of the background radiance. In the case of upward viewing, K_L equals K_{Ld}, the attenuation coefficient of direct downward radiance (Johnsen, 2002).

The correct OTF for objects being viewed from below is obtained by normalizing the original OTF so that $\text{OTF}(0)$ equals $e^{-(c - K_{Ld})x}$ (Mertens, 1970). Thus the final equation for the propagation of images viewed from below is

$$\text{image}_{\text{final}}(x)$$
$$= \mathscr{F}^{-1}\left[\mathscr{F}(\text{image}_{\text{initial}}) \cdot \left(e^{-(c - K_{Ld})} \cdot \frac{\text{OTF}_1}{\text{OTF}_1(0)} \right)^x \cdot \text{OTF}_{\text{eye}} \right].$$

(Equation 6)

The OTF is a complex-valued function and difficult to interpret. Therefore, its magnitude, known as the modula-

tion transfer function (MTF), is often also calculated. The MTF is quite useful because it gives the fraction of remaining image contrast as a function of spatial frequency. For example, $\text{MTF}(4) = 0.5$ implies that 50% of the original image contrast remains for detail that has a spatial frequency of 4 cycles per degree.

Images examined

Images of the ventral bioluminescence of two counter-illuminating species were used: (1) the enoploteuthid squid *Abralia veranyi* (Rüppell, 1844) (eye-flash squid), and (2) the myctophid fish *Ceratoscopelus maderensis* (Gunther, 1864) (horned lanternfish) (Fig. 2A, B). The two were chosen to provide a range of photophore spacing. Counter-illumination in *A. veranyi* is finely detailed; that of *C. maderensis* is relatively coarse (Fig. 2C, D). *A. veranyi* was collected at depth, using the *Johnson-Sea-Link* research submersible fitted with 11-liter acrylic plastic cylinders with hydraulically activated, sliding lids. *C. maderensis* was collected at night, using an opening/closing Tucker trawl (4.3-m² opening, ¼ inch knotless nylon mesh) fitted with a thermally insulated collecting container. Specimens were manually stimulated to bioluminesce, and then were recorded with a Dage ISIT image-intensified video camera (*A. veranyi*) or Intevac GenIISys image intensifier system and CCD video camera (*C. maderensis*). Images that show how the counterilluminating animals appear from below (Fig. 2E, F) were created by combining the bioluminescence images with silhouettes of the animals obtained from normal illumination photographs (taken immediately after the intensified images). Non-illuminating portions of the animals are shown as black because this is how they appear against the downwelling light (Johnsen, 2002). The natural posture of *A. veranyi* is unknown. Although observers in submersibles generally find mesopelagic squid with their fins folded and their arms and tentacles placed over their heads (Vecchione and Roper, 1991; Fig. 2A), this is may be a response to the perceived threat from the submersible. In the silhouette chosen, the fins and appendages were extended to examine their effect on visibility.

The backgrounds were set to a brightness equal to the average brightness of the counterilluminating animal (minus the fins, arms, and tentacles in the case of the squid). Because these relative values allow the animal to blend with the background most easily, it is assumed that they approximately match what would be observed in the field. The backgrounds for the *C. maderensis* images are darker because the average brightness of the animal is darker (due to the wider spacing of the photophores). Note that these figures show *relative* brightnesses, chosen to maximize visibility on the printed page. The *absolute* brightnesses are of
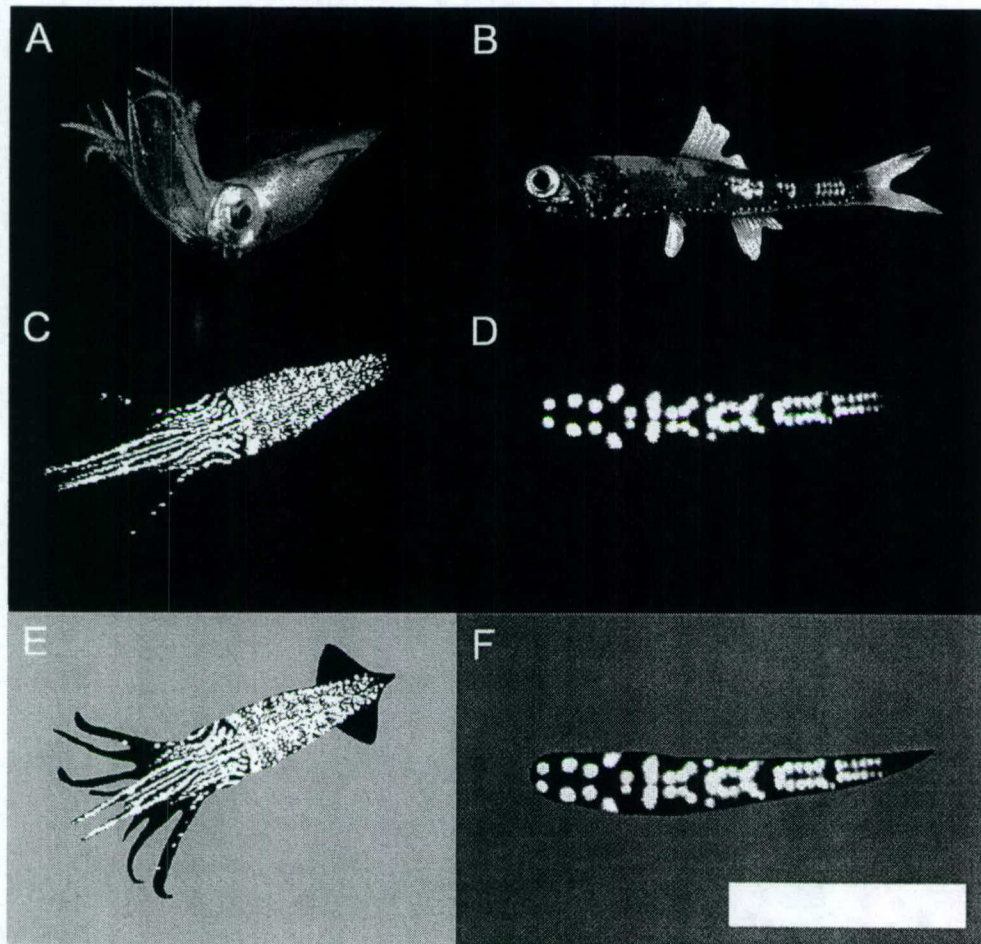
Figure 2. (A) The eye-flash squid *Abralia veranyi.* (B) The horned lanternfish *Ceratoscopelus maderensis.* (C) Counterillumination of *A. veranyi.* (D) Counterillumination of *C. maderensis.* (E) Counterillumination of *A. veranyi* as viewed from below against the downwelling light. (F) Counterillumination of *C. maderensis* as viewed from below against the downwelling light. Scale bar is 5 cm. Background in (E) and (F) is set to the average brightness of the counterilluminating animal. Panel B courtesy of Marine Biological Laboratory Digital Archive, Flescher Fish Collection.

course much dimmer (far beyond the reach of printed paper) and can only be seen by the dark-adapted eye.

The intensified images are not perfect representations of the actual counterillumination. The resolution of the images is low, and the photophore signals are slightly expanded due to "blooming" of the image at the detector array. In addition, although counterillumination is more stable than other bioluminescent signals, the images are static representations of potentially variable light emission. Indeed, a subset of the ventral photophores in *A. veranyi* was not lit in the studied image (Herring *et al.,* 1992). This relatively low number of small photophores most likely would not change a spatial distribution that is already quite uniform. However, they may play a role in spectral changes. In *C. maderensis,* all the ventral photophores were emitting during the image exposure.

Calculation of point spread functions and attenuation coefficients

The PSFs in this study were determined using Monte Carlo software (BSFPSF ver. 1.1., developed by CDM). Five million simulated photons were tracked from an isotropic point source (of unit power) to their point of intersection with a sphere of radius 1 m. Although a PSF is defined as the image of a cosine point source, the use of an isotropic point source achieves the same result because scattering in natural waters is primarily in a forward direction (Mertens and Replogle, 1977; confirmed by preliminary calculations). Due to the symmetry of an isotropic point source, calculations could be completed in far less time than if a cosine point source were used.

The radiance distribution of the simulated photons at the

intersection with the 1-m sphere is the PSF. The three factors (besides distance) affecting the PSF are (1) the absorption coefficient a, (2) the scattering coefficient b, and (3) the phase function γ. The first and second factors specify how often a photon is absorbed or scattered by the water and associated particulates. The third factor specifies the angular distribution of the scattered light. Absorption and attenuation coefficients were obtained for four water types: (1) coastal water at 5-m depth, (2) oceanic water at 5-m depth, (3) oceanic water at 210-m depth, and (4) oceanic water at 800-m depth (Table 1). Absorption and scattering coefficients for coastal water were obtained by Dr. Heidi Sosik (Woods Hole Oceanographic Institution, Woods Hole, MA) using a dual-path, multiband absorption/attenuation meter (ac-9, WETLabs Inc.) at a site 80 km from the coast of Portsmouth, New Hampshire (42°47′N 70°05′W, 1106 local time, 30 June 2000) (see Johnsen and Sosik, 2003, for details). Optical coefficients in oceanic water (Jerlov type I) at 5 m and 210 m were obtained by Drs. Andrew Barnard, Scott Pegau, and Ronald Zaneveld (College of Oceanic and Atmospheric Sciences, Oregon State University, Corvallis, Oregon) using the same equipment in the equatorial Pacific (1005 local time, 30 April 1996; 0°0′N 177°21′W). Optical coefficients in oceanic water at 800-m depth were obtained from Capone et al. (2002). In all cases, absorption and beam attenuation coefficients were measured at 412, 440, 488, 510, 532, 555, 650, and 676 nm. Although point spread functions were calculated for all eight wavelengths, for clarity only those at 412, 488, 555, and 650 nm are analyzed and discussed in this study. While the 5-m coastal measurement is somewhat specific to measurement site, the three oceanic measurements are typical of most oceanic waters, particular those at 210 and 800 m.

Because the ac-9 absorption-attenuation meter has detectors of finite size, light scattered over small angles was collected by the detector and incorrectly interpreted as unscattered. Thus, scattering was underestimated by a small amount. If one assumes that the scattering matches Petzold's phase function, then the scattering coefficient is underestimated by approximately 20%. Again, preliminary results showed that this had negligible effect on the blurring of the image, though it would have resulted in slightly

greater attenuation of the contrast of the whole image. The ac-9 meter also does not measure certain factors that may influence image propagation, such as marine snow and refractive index inhomogeneities. The large particles of marine snow will limit the long-range visibility of small objects by direct occlusion, and refractive index inhomogeneities may slightly increase scattering at very small angles (below the resolution limit of the visual systems examined) (Bogucki et al., 1998).

The phase function γ was chosen to be the commonly used "average particle" function (Mobley et al., 1993) based on measurements by Petzold (1977). In productive coastal waters, most of the light is scattered by living phytoplankton, which have a backscatter fraction of 0.01 or less (e.g., Ulloa et al., 1994). However, in clear oceanic water, isotropic scattering by the water itself is a significant fraction of the total scattering, and the total backscatter fraction can be as large as 0.04 (Mobley, 1994). We chose Petzold's average particle phase function (Mobley et al., 1993), which has a backscatter fraction of 0.018, about midway between the two extremes. Preliminary results showed that, because scattered light was extremely dim compared to the unscattered direct beam, the choice of phase function made no notable difference.

PSF values were calculated up to 10°, at 0.05° intervals. Although the PSF from 0 to 1° was calculated using Monte Carlo methods, computational limits (due to the small size of the angular bins receiving scattered photons) prevented accurate calculations at substantially higher angles for the given number of initial photons. Therefore, the PSF from 1° to 10° was estimated by fitting the PSF from 0.45° to 1° to a power function and then extrapolating by 0.05° increments up to an angle of 10° (see Voss, 1991, for justification).

The optical transfer functions of the eyes were modeled as the Gaussian curve:

$$\text{OTF}(\nu) = e^{-3.56 \cdot (R\nu)^2} \qquad \text{(Equation 7)}$$

where ν is the spatial frequency (in cycles/degree) and R is the spatial resolution (Warrant, 1999). This function, often used to model the OTF of visual systems, results in a barely

Table 1

Absorption and scattering coefficients (a and b respectively) used in the Monte Carlo calculation of point spread functions

Wavelength (nm)	Coastal water at 5-m depth		Oceanic water at 5-m depth		Oceanic water at 210-m depth		Oceanic water at 800-m depth	
	a	b	a	b	a	b	a	b
412	0.29	0.26	0.035	0.11	0.060	0.018	0.027	0.020
488	0.15	0.21	0.038	0.098	0.035	0.013	0.027	0.014
555	0.11	0.19	0.073	0.091	0.077	0.0094	0.072	0.0060
650	0.37	0.15	0.36	0.085	0.36	0.014	0.36	0.014

detectable contrast of 2.8% ($= e^{-3.56}$) at the spatial resolution of the eye. The spatial resolutions of three mesopelagic fish were chosen to span a wide range of visual acuity: (1) $R = 0.11°$ (the "lovely hatchetfish" *Argyropelecus aculeatus*), (2) $R = 0.23°$ (the spookfish *Opisthoproctus soleatus*), and (3) $R = 0.50°$ (the myctophid fish *Lampanyctus festivus*) (Collin *et al.*, 1997; Wagner *et al.*, 1998). *A. aculeatus* and *O. soleatus* both have upward-viewing tubular eyes; *L. festivus* has lateral-viewing eyes and so probably does not search for overhead, counterilluminating prey.

The acuity of these species was measured from the density of their retinal ganglion cells (which accounts for spatial summation). Because these counts also include displaced ganglion cells, they may slightly overestimate acuity. The predicted acuity also assumes a well-focused image, but this is generally the case for the foveal regions of deep-sea eyes (Warrant and Locket, 2004). Increasing spatial summation will also lower the acuity. Finally, it is important to note that these spatial resolutions do not include potential blurring of a moving image due to large temporal summation. Since long temporal summation times are common at depth (Frank, 1999) and animals do drift relative to one another in the water, the actual spatial resolution in certain situations may be less than that predicted by retinal morphology.

The minimum contrast threshold is the smallest percentage variation in radiance that can be detected. This value for fish is approximately 1%–2% in bright light, but it rises as depth increases (Douglas and Hawryshyn, 1990). Though few direct measurements have been made, the threshold at mesopelagic light levels appears to range from about 25% to 50% (*e.g.*, threshold for the Atlantic cod *Gadus morhua* at 650-m depth is approximately 50% (Anthony, 1981)). We therefore set the minimum contrast threshold at 33%, while accepting that depth, water clarity, and special visual adaptations make the actual threshold highly variable.

The attenuation coefficients of direct downward radiance K_{Ld} were calculated by modeling the underwater radiance distribution using radiative transfer software (Hydrolight 4.2, Sequoia Scientific Inc., Bellevue, WA, www.hydrolight.info). The inherent optical properties required by the software were obtained from measured vertical profiles of chlorophyll concentration and absorption and scattering coefficients from the four water types examined (see Johnsen, 2002; and Johnsen and Sosik, 2003, for details). The sun was assumed to be at the zenith on a clear day with no wind.

Measurement of moonlight and starlight spectra

Nocturnal spectra under moonlight and starlight were measured using a spectrometer with a highly sensitive photomultiplier detector (OL-754-PMT, Optronics Laboratories Inc., Orlando, FL). Moonlight spectra were measured in air on a barrier island in Florida during full moon (moon was at its peak elevation). An integrating sphere was used to collect light from all regions of the sky. Starlight spectra were measured on a moonless night on a completely darkened ship in the center of the Gulf Stream (latitude ~27°N) to ensure a complete absence of light pollution. To minimize light loss, the integrating sphere was removed and the entrance slit of the spectrometer (~30° angular field) was aimed at the zenith. The downwelling irradiance at 5-m depth under moonlight and starlight was calculated using the above-described radiative transfer software, with the correct skylight spectrum as an input.

Results

Point spread and optical transfer functions of the water types and visual resolutions

The point spread functions in all four water types were extremely narrow, with the radiance at zero degrees 2–3 orders of magnitude larger than the radiance at higher angles (at a distance of 5 m) (Fig. 3). With increasing water clarity and depth, this effect became more pronounced. The wavelength dependence of the PSF was complex, depending on the relative numbers of scattering and absorption events.

In all four water types, the modulation transfer function was primarily affected by the visual resolution of the viewer's eye (Fig. 4). However, the MTFs in near-surface waters decreased at higher spatial frequencies (independently of the decrease due to visual acuity limitations), indicating some blurring by the water (Fig. 4A, B). The MTFs within a given water type had similar shapes and differed primarily in magnitude (set by $\text{MTF}(0) = e^{-5(c - K_{Ld})}$). This magnitude had a complicated wavelength dependence, being proportional to wavelength in near-surface waters and inversely proportional to wavelength in deep waters.

Perceived images

The perceived images were dramatically affected by the visual resolution of the viewer and, to a lesser extent, by scattering and absorption by the water (Figs. 5, 6). When viewed at 0.11° resolution, *Ceratoscopelus maderensis* and *Abralia veranyi* had a contrast greater than 33% at distances up to 4 to 8 m (though the visibility of the latter was primarily due to the unlit fins and appendages). However, when viewed at 0.5° resolution, the contrast of the counterillumination was greater than 33% only up to a distance of 1 to 2 m. The individual photophores of *C. maderensis* were distinguishable up to 2 m at 0.11° resolution, and the general pattern of photophores was distinguishable up to 2 m at lower resolutions. The general pattern of the photophores of
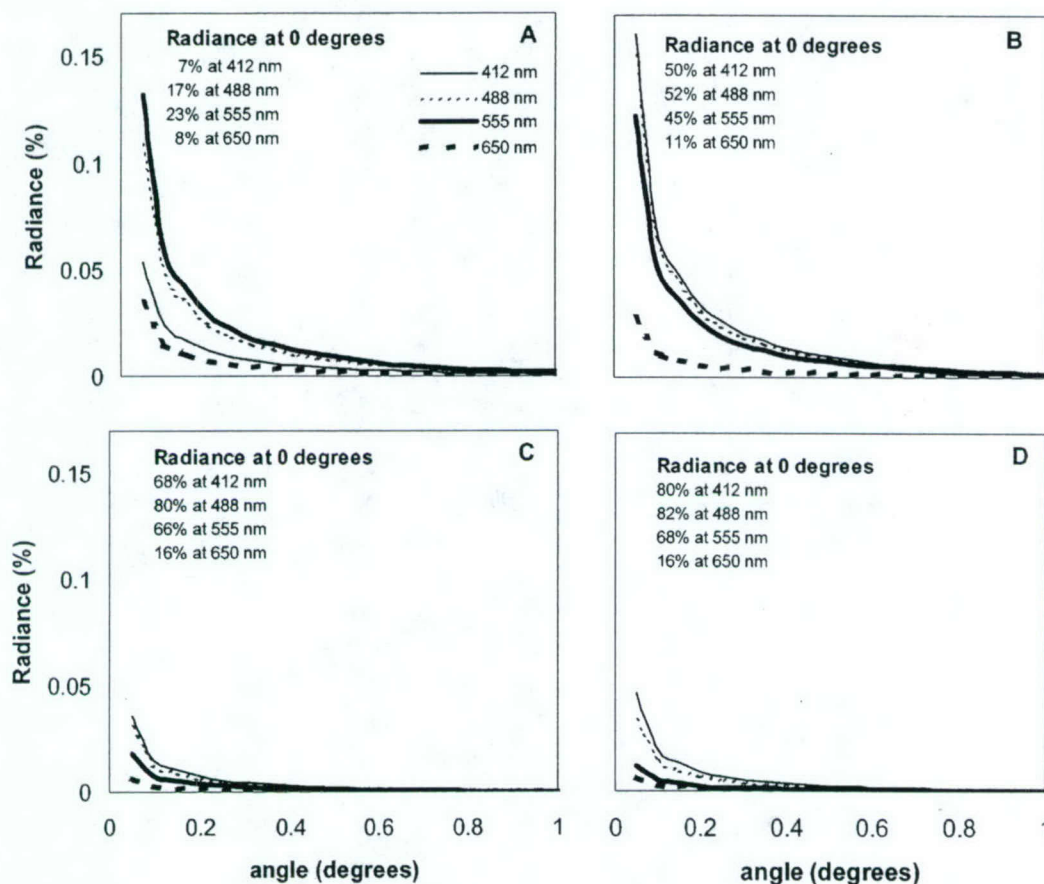
Figure 3. Radiance *vs.* angle for a point source viewed from a distance of 5 m (point spread function). The radiance is normalized by the radiance of a point source viewed at 5 m in a medium that does not scatter or absorb light. (A) Coastal water at 5-m depth. (B) Oceanic water at 5-m depth. (C) Oceanic water at 210-m depth. (D) Oceanic water at 800-m depth. The normalized radiances at zero degrees are given numerically rather than graphically because they are far higher than the other values.

A. veranyi was evident at 1 m at 0.11° resolution, but not at lower resolutions.

The counterillumination of both species is visible at roughly twice the distance in the clearest conditions studied (at 488 nm in oceanic water at 800-m depth) as it is in the most turbid conditions (at 412 nm in coastal water at 5-m depth) (Fig. 5A *vs.* 5B, Fig. 6A *vs.* 6B). The difference was entirely due to the difference in MTF(0) between the two water types (95% *vs.* 37% at a distance of 5 m) and not to significantly increased blurring of fine detail.

Variation of background spectra and wavelength dependence of contrast attenuation

The background spectra at shallow depths under moonlight and starlight differed substantially in both coastal and oceanic waters, particularly at shorter wavelengths (Fig. 7A, B). Under starlight, the spectrum narrowed and the peak wavelength was long-shifted (by 40 to 80 nm depending on

the water type and what is considered the true peak). The background spectra were also affected substantially by depth, even at mesopelagic depths. As the depth increased from 200 to 800 m, the spectra of the downwelling irradiance narrowed slightly and the peak wavelength shifted from 490 nm to 480 nm (Fig. 7C).

General contrast attenuation was relatively rapid and wavelength-independent at 5-m depth in both coastal and oceanic waters, with sighting distances (proportional to $1/c - K_{Ld}$) only 5%–20% of those in deeper waters (Fig. 7D). At greater depths, sighting distance was highly dependent on wavelength. At these depths, sighting distance increased with wavelength, until it reached a peak at a wavelength about 30 nm longer than that of the peak wavelength of downwelling irradiance. After this peak, the sighting distance decreased rapidly with wavelength. For wavelengths greater than 600 nm, the sighting distances at depth were less than those near the surface.
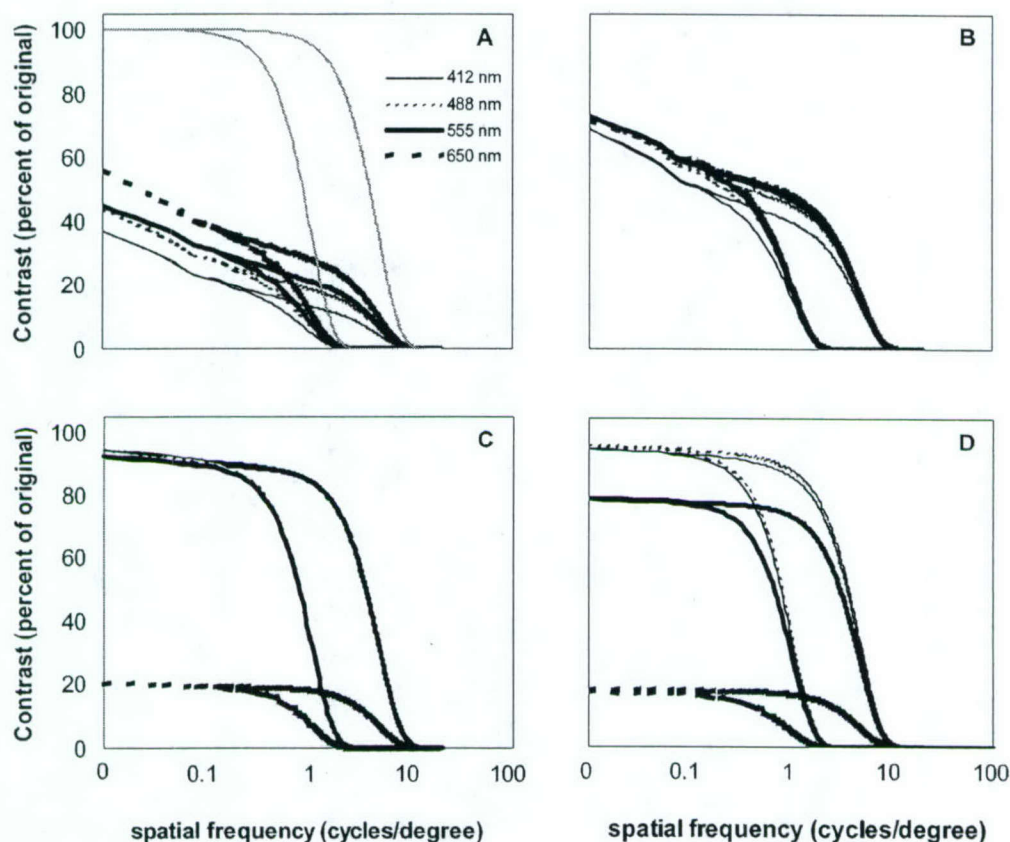
Figure 4. Contrast as a function of spatial frequency for an object viewed from a distance of 5 m (modulation transfer function, MTF). The contrast is normalized by the contrast at a distance of 0 m. (A) Coastal water at 5-m depth. (B) Oceanic water at 5-m depth. (C) Oceanic water at 210-m depth. (D) Oceanic water at 800-m depth. The MTF is shown for two visual systems, one with 0.11° resolution and one with 0.5° resolution. At a spatial frequency of approximately 0.4 cycles/deg, the data split, with the lower trace denoting 0.5° resolution. The two gray lines in (A) denote the MTF for the eyes alone. Because the MTF at 0 cycles/deg is important, the graphs include this point despite being logarithmic.

Discussion

This study shows that a counterilluminating individual faces a number of difficulties. First, an acute eye (0.11° resolution) with moderate contrast sensitivity (33%) can detect the photophore patterns of both *Abralia veranyi* and *Ceratoscopelus maderensis* at distances greater than 1 m. Second, even the water at the relatively turbid shallow coastal site blurred the counterillumination signals very little. Although all four water types did lower the overall contrast of the counterilluminator, the attenuation rate was quite low, particularly at mesopelagic (>200 m) depths. Finally, the spectrum of downwelling background light varied considerably with depth in the mesopelagic zone and was strongly affected by the source of nocturnal illumination at the shallow depths. This suggests that counterilluminating photophores must be spaced closely together when viewed by visually acute species, and that matching the

background spectrum may be more difficult than previously considered. From the predator's point of view, this study suggests that high spatial resolution and color discrimination in the blue-green portion of the spectrum are highly advantageous for detecting counterilluminating prey. However, since both of these characteristics reduce sensitivity, they also have a cost that must be balanced.

The remainder of the paper explores these limitations in detail. It is important to note that, despite these limitations, counterillumination dramatically decreases the visibility of the individual. The visibility of *A. veranyi* at distances greater than 1 m is entirely due to the unlit fins, tentacles, and arms (Fig. 5), which may be held above and against the body to minimize their silhouette (Fig. 2A). The visibility of these unlit regions at distances of at least 8 m highlights the impressive crypsis afforded by counterillumination. In addition, in certain cases the goal may not be complete cryp-
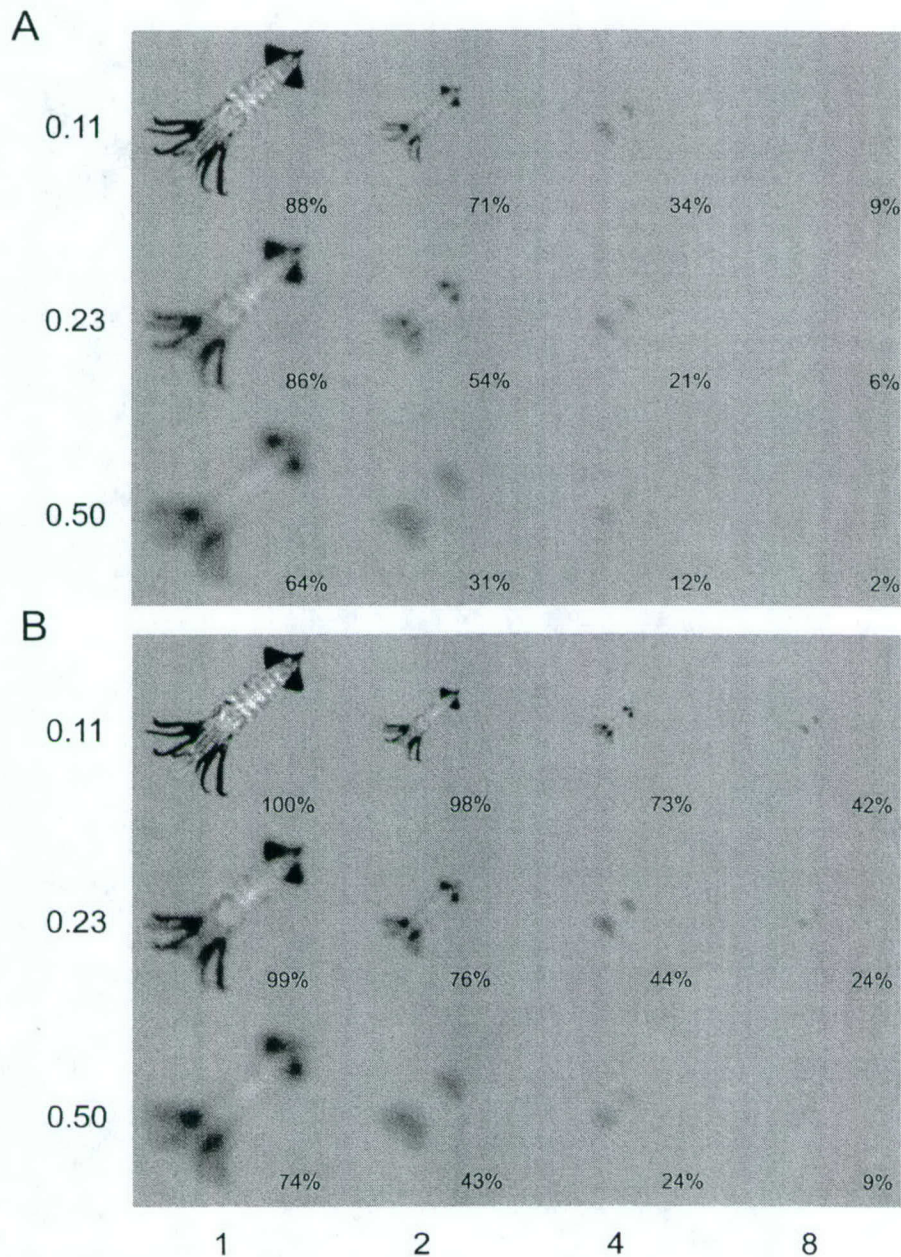
Figure 5. Counterillumination of *Abralia veranyi* viewed from distances of 1, 2, 4, and 8 m by animals with eyes of 0.11°, 0.23°, and 0.5° resolution. (A) Counterillumination is viewed at a wavelength of 412 nm in coastal water at 5-m depth (the optical conditions that had the greatest effect on image propagation). (B) Counterillumination is viewed at a wavelength of 488 nm in oceanic water at 800-m depth (the optical conditions that had the least effect on image propagation). The percentages indicate the maximum contrast in each image. All images are scaled in size for viewing distance, and the backgrounds are all set equal. To see the absolute brightness values in the image, view the figure under dim illumination so that the printed background matches the brightness at the relevant depth. For example, to see what the counterillumination looks like at depths of 200, 300, and 400 m, view the figure under civil twilight, full moonlight, and half-moonlight respectively.

sis, but a bioluminescent analog of disruptive coloration. The individual photophores may break up the silhouette so that it appears as a number of small objects rather than as one large, recognizable outline. This tactic is common and highly successful in benthic and terrestrial habitats where the background is complex (Lythgoe, 1979). Its effective-
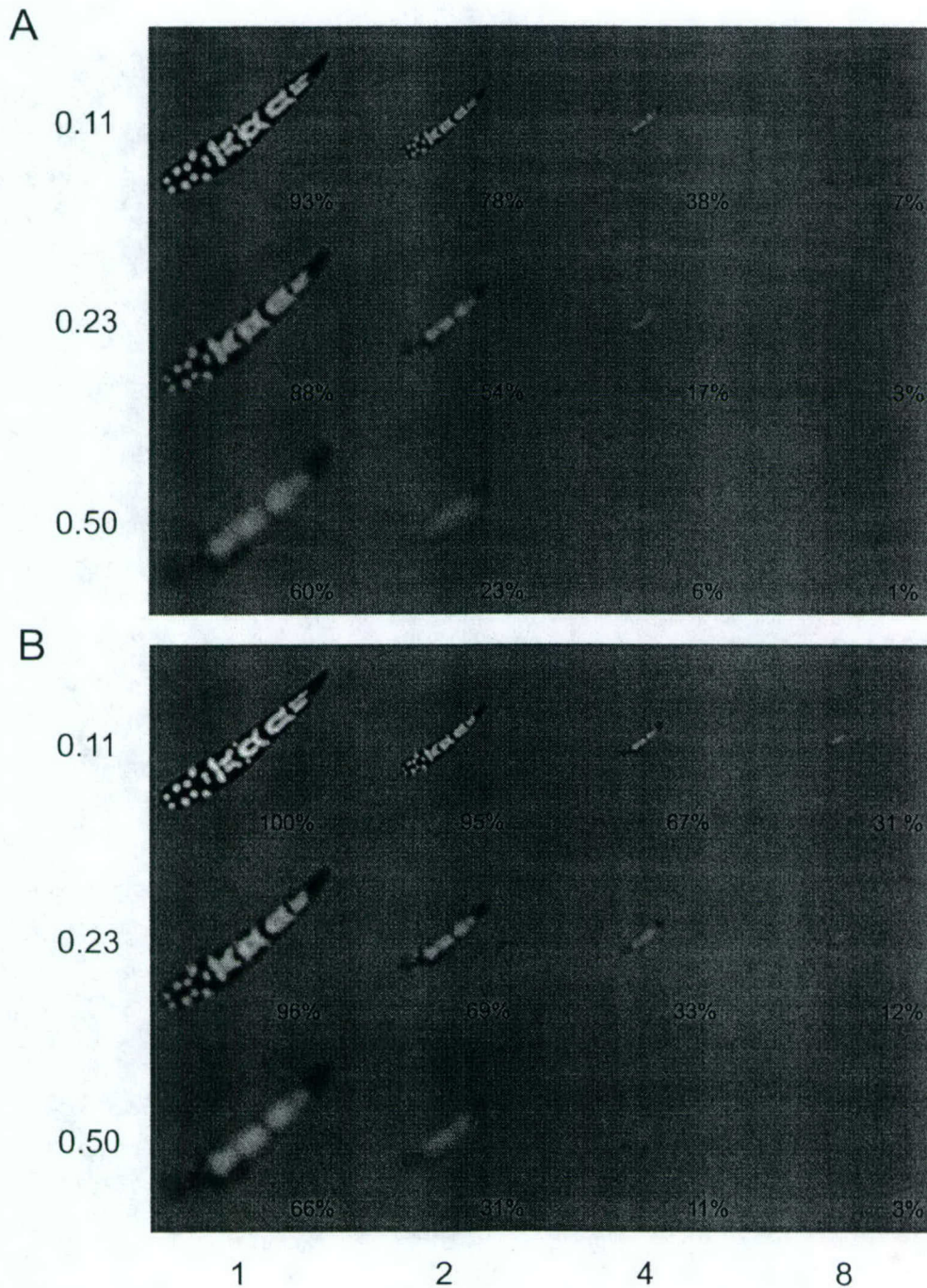
Figure 6. Identical to Figure 5, except that the counterillumination signal is generated by *Ceratoscopelus maderensis.*

ness in pelagic environments, where the background is very uniform, is uncertain. Finally, the ability of the predator to recognize the perceived image as potential prey depends on pattern recognition, a higher level of visual processing that is poorly understood in oceanic species.

Effects of intervening water on counterillumination

Despite the authors' initial expectations, the water had little effect on the appearance of the counterillumination. This was due to several factors. First, even in the worst case
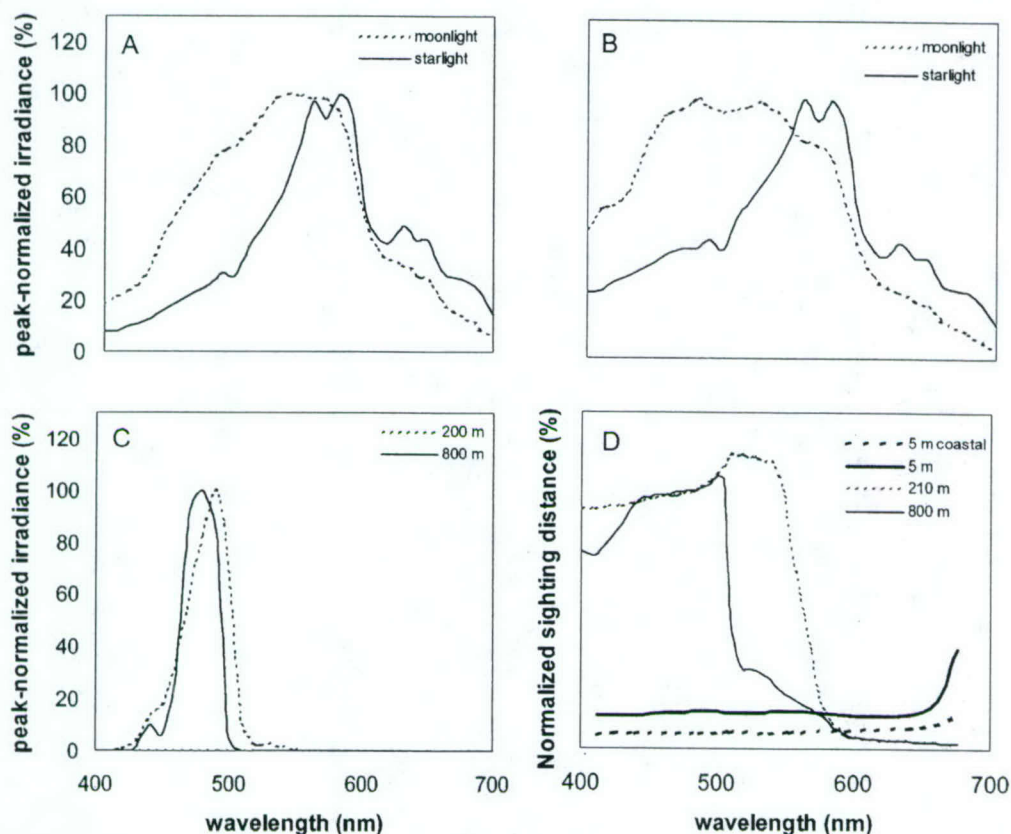
Figure 7. (A) Downwelling irradiance (normalized by peak) at 5-m depth in coastal water under moonlight and starlight. (B) Same as (A), but in oceanic water. (C) Downwelling daytime irradiance at depths of 200 and 800 m. (D) Sighting distance of a counterilluminator, normalized by sighting distance in mesopelagic waters at 480 nm. Because all published bioluminescence spectra are calibrated in energy units (instead of quanta), (A), (B) and (C) are calibrated in relative energy units.

(412-nm light in coastal water at 5-m depth), 8% of the photons were neither scattered nor absorbed after traveling 5 m ($=e^{-5(a + b)} = e^{-5(0.29 + 0.26)}$). The viewer perceives these uncollided photons as all arriving from one point (which has a radius determined by the spatial resolution of the eye), so the perceived radiance of this unscattered light is quite high. In contrast, the scattered photons, although more numerous (92% in this case), are scattered over a larger angular area and so have a lower radiance. Second, for a photon to contribute to image blurring, it must be scattered but not absorbed by the water. Because highly scattering waters also tend to be highly absorbing (see Table 1), many scattered photons are absorbed before they can reach the eye and thus cannot contribute to image blurring. This is in sharp contrast to atmospheric scattering (e.g., due to haze or fog), which can be high while absorption is negligible (Bohren and Huffman, 1998). Finally, light scattering in water is strongly biased in the forward direction. In the phase function used in this study, more than 50% of the scattered photons are deflected less than 5° (Petzold, 1977).

Thus, the halo of scattered light surrounding the image of a point source is quite narrow. This also differs from the atmospheric case, where light is often scattered over relatively large angles (Bohren and Huffman, 1998). For all the above reasons, the images in all the water types examined did not lose a substantial amount of fine detail. There are, of course, considerably more turbid marine waters (very close to shore or to river plumes, coccolithophore blooms, etc.). Counterilluminators, however, are seldom found in these locations.

A parameter that was greatly affected by the water was the attenuation of the contrast of the entire scene (e.g., MTF(0)). The attenuation coefficient depends on the viewing angle of the predator and for upward viewing is $c - K_{Ld}$ (see Eq. 5). This coefficient is far smaller than the attenuation coefficients for viewing an object horizontally or from above (c, and $c + K_{Ld}$ respectively), so objects viewed from below are visible at much longer distances (Johnsen, 2002). This result derives from the fact that, as a viewer moves down and away from a counterilluminator, the background

dims almost as quickly as the signal does, thus maintaining the contrast. The unusual wavelength dependence of the attenuation of counterillumination occurs because c and K_{Ld} vary somewhat independently. At shorter wavelengths, $c - K_{Ld}$ increases slightly with wavelength; at longer wavelengths at depth, c increases rapidly with wavelength, while K_{Ld} remains more or less constant. This is because almost all long-wavelength light at depth is due to Raman scattering, in which a small portion of the blue-green light is converted into longer wavelength light (Marshall and Smith, 1990; Johnsen, 2002). Because this Raman-scattered light is produced *de novo* from shorter wavelength light, it has roughly the same attenuation coefficient as that light, and so the difference between c and K_{Ld} can grow quite large. But because the long wavelength light is extremely dim, it may not be of visual significance, particularly at mesopelagic depths.

A curious feature of this wavelength dependence is that the wavelength of least contrast attenuation is about 30 nm longer than the peak wavelength of the downwelling light. The lower contrast attenuation at these wavelengths allows for a slightly longer sighting distance (proportional to $1/c - K_{Ld}$: 12.5% longer at 210 m; 5.5% longer at 800 m) than at the peak wavelength. Because the spectral responses of most deep-sea visual systems are relatively flat (Douglas *et al.*, 1998), this shift may be inconsequential.

Effect of variation in background illumination

The fact that the spectrum of the background changes with depth has been examined before (*e.g.*, Young and Mencher, 1980). This study confirms that, even at mesopelagic depths, the spectrum changes substantially with depth. While a 10-nm shift in the peak wavelength appears minor, it causes large shifts in the intensity of the off-peak light because the wavelength distributions are quite narrow. For example, if the peak intensities are set equal at 100% (as in Fig. 7C), the difference between the downwelling irradiance at depths of 200 and 800 m is 62% at 500 nm and 32% at 470 nm.

A previously unconsidered issue is the effect of the nocturnal illumination source. Many counterilluminators are vertical migrators and can be found near the surface at night (the downwelling irradiance at 5-m depth under moonlight and starlight equals that found during the middle of the day at 300 and 500 m respectively). The background illumination then depends on whether the moon is present. Over a complete lunar cycle, the moon is above the horizon for about half of the nocturnal hours. Because the moon reflects all wavelengths more or less equally (Munz and McFarland, 1977), the spectrum of the night sky with the moon present is similar to the spectrum of daylight (though dimmer by about 6 orders of magnitude, and slightly red-shifted due to background starlight). When the moon is not

present, the illumination has three primary components: (1) starlight, mostly due to dim red stars invisible to the naked eye, (2) scattering of sunlight by dust in the plane of the solar system, and (3) emission spectra from gases in the upper atmosphere (*e.g.*, airglow) (Munz and McFarland, 1977). The final irradiance spectrum is strongly red-shifted. Whereas the spectral shift from moonlight to starlight is minor at mesopelagic depths, it is quite obvious in near-surface waters (Fig. 7A, B), particularly in blue, oceanic waters. Since very few marine species are known to have long-wavelength sensitivity at scotopic light levels, the implications of the spectral shifts at these wavelengths are unknown. However, the shifts at blue-green wavelengths (450–500 nm) are also substantial, and can be detected by nearly all deep-sea visual systems. Although certain counterilluminating species alter the spectra of their emitted light with ambient temperature or depth (Young and Mencher, 1980; Young and Arnold, 1982; Herring *et al.*, 1992), adaptations to the spectral shift caused by the presence or absence of the moon are unknown.

Implications for counterillumination

The clarity of the water and the spectral variation due to depth and the presence or absence of the moon have several important implications for counterilluminators. First, since it is unlikely that light scattering by the water will combine the light from the individual photophores into an even light field, an animal with few, widely spaced light organs is at a disadvantage, particularly when the background light levels are relatively high. Furthermore, the fewer the photophores, the brighter they must be to balance out the unlit regions of the ventral surface. In this study, the photophores of *C. maderensis* had to be 175% brighter than the background radiance, whereas the more finely distributed photophores of *A. veranyi* had to be only 34% brighter. For this reason, a counterilluminator viewed by a high-resolution eye will appear as a signal both brighter and darker than the background (*i.e.*, bright photophores on a silhouetted body). This may explain why shallower species generally have more finely spaced photophores, since acute vision is only possible at higher levels of illumination (Widder, 1999; Warrant and Locket, 2004).

A second important implication of this study is that counterillumination is potentially more successful at shallower depths. Due to the greater contrast attenuation at shallow depths, any mismatch with the background is detectable at only 5%–20% of the distance at which the same mismatch would be detectable in deeper waters. This increase in contrast attenuation may offset the disadvantage due to the variable spectra and angular distribution found near the surface.

Finally, because contrast attenuation is relatively constant over a wide range of wavelengths (Fig. 7D), and because

contrast sensitivity decreases rather slowly with decreasing illumination (Warrant, 1999), a counterilluminator ideally must match the downwelling spectrum from about 450 to 520 nm at depth and over a somewhat greater wavelength range near the surface. However, a survey of published photophore spectra shows that this is not the case (Fig. 8). Photophores involved in counterillumination do have spectral characteristics different from those used for other purposes, but the pattern is far from intuitive. In fish, counterilluminating photophores produce light with roughly the same peak wavelength (but with a narrower spectrum) as those of non-counterilluminating photophores. In decapods, the peak is red-shifted and the spectrum narrower in counterilluminating *versus* non-counterilluminating photophores. In squid and a few fish, counterilluminating photophores emit light at a longer (and occasionally shorter) wavelength than the non-counterilluminating photophores. Interestingly, the spectra of the counterilluminators, despite being quite clustered (suggesting natural selection), seldom match the downwelling spectrum. Some are 10–20 nm too blue, and others are 10–30 nm too red. This suggests that they may be visible to predators whose color discrimination
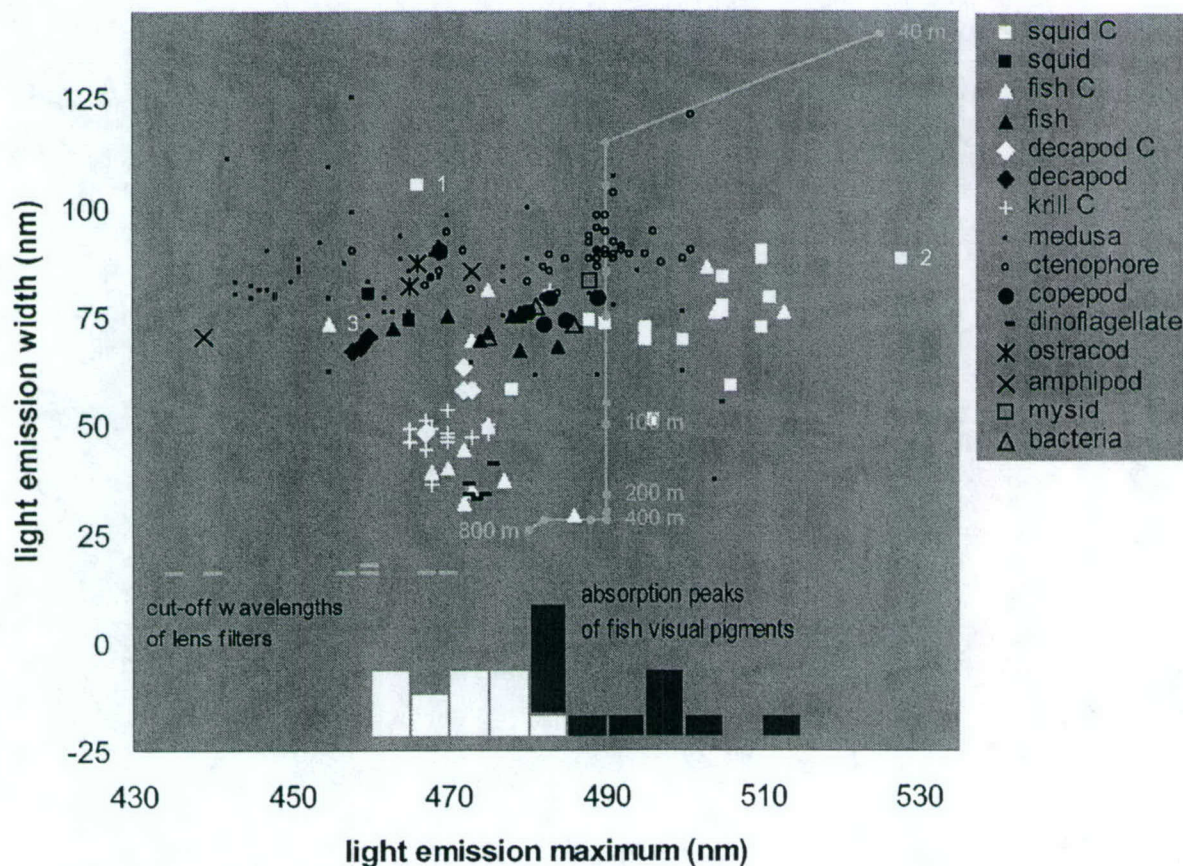
Figure 8. Peak wavelength *vs.* emission width (full-width half-max, FWHM) for the light emissions from various species. White symbols denote photophores involved in counterillumination. Black symbols denote photophores and other luminous sources used for other tasks (warning, luring, etc.). The outliers among the counterilluminators are [1]*Abraliopsis falco* (enoploteuthid squid), [2]*Teuthowenia megalops* (cranchiid squid), [3]*Isistius brasiliensis* (cookie-cutter shark). White line shows peak wavelength and FWHM for downwelling light as a function of depth (depth intervals are 10 m down to 100 m, and then 100 m for depths down to 800 m). Bar chart is a histogram of visual pigment absorption peaks for deep-sea fish eyes known to have multiple pigments in the blue-green portion of the spectrum (data from Douglas *et al.*, 1998). The white bars are the short-wavelength pigments; the black bars are the long-wavelength pigments. The gray symbols show the cut-off wavelengths for the filters in the lenses of seven species of deep-sea fish (data from Douglas and Thorpe, 1992). Photophore spectral data taken from Nicol (1960), Swift *et al.* (1973, 1977), Biggley *et al.* (1981), Herring (1983), Denton *et al.* (1985), Widder *et al.* (1983), Herring *et al.* (1992, 1993), and Haddock and Case (1999). Because the published bioluminescence spectra are calibrated in energy units (instead of quanta), the downwelling light curve is calibrated in relative energy units.

at blue and green wavelengths is good owing to multiple visual pigments or ocular filters.

Although about 15 deep-sea species (including fish, alciopid polychaetes, oplophorid shrimp, and the squid genus *Watasenia*) are known to have multiple visual pigments, most deep-sea species apparently are monochromatic, with a relatively flat spectral response near the maximum wavelength (due to the extreme thickness of their photoreceptors) (Douglas *et al.*, 1998). Therefore the spectral mismatches seen in Figure 8 may not be detectable as a color shift by many predators (excepting those possessing color filters). For a counterilluminator facing a color-blind predator, the relevant issue is that the light emitted from the photophores is attenuated more quickly than the downwelling light, due to higher absorption at non-peak wavelengths. Therefore, even if the emitted light perfectly matches the background intensity at one distance, the counterillumination will become darker than the background at a greater distance. The difference between the attenuation coefficients at 470 nm and 480 nm is small. Therefore, this issue is likely to be insignificant for the krill, fish, and decapods whose photophores emit at 470 nm. The close clustering of the spectra of these species remains puzzling, but may be an evolutionary strategy to prevent predators from developing a species-specific search image. This is analogous to the "selfish herd" effect, in which identical individuals in large aggregations reduce their chance of predation (Hamilton, 1971; Bond and Al Kamil, 2002).

The light emitted by squid photophores that peaks at 510 nm will be attenuated significantly more quickly than the downwelling light, potentially leading to the detection of the squid, but these measured spectra may not be representative of the natural spectra. As mentioned above, certain squid can change the spectrum of their counterillumination depending on temperature. Since the spectral measurements were not done *in situ* and often required a fair bit of manipulation, the squid may have been at a higher temperature and thus produced light to match shallower and therefore greener water. In fact, the published spectra of all counterilluminators must be treated with some caution because very few of the animals were measured while they were passively counterilluminating, but instead were being manually stimulated to emit light. Because manual stimulation tends to turn on all available photophores in an attention-getting signal that is assumed to act as a "burglar alarm" (Widder, 1999), the measured spectrum may include light from photophores that are not active during counterillumination, altering the spectrum.

Effects of visual resolution and color discrimination on perceived image

Although the range of water types commonly inhabited by counterilluminators had little effect on their visibility, the range of visual acuities of potential predators had a dramatic effect. Because light scattering by the water had little effect on the appearance of the counterillumination signal, acute vision can detect the individual photophores and is therefore highly advantageous. Indeed, many deep-sea species are known to have far greater resolution ($\sim 10\times$) in the dorsal viewing region than in other directions (Collin *et al.*, 1997; Wagner *et al.*, 1998; Land, 1999; Warrant and Locket, 2004). For example, although the spatial resolution for upward viewing in the hatchet fish *Argyropelecus aculeatus* is 0.11° (see Materials and Methods), the spatial resolution over the rest of visual field is 0.7°–1.7° (Collin *et al.*, 1997). In contrast, the myctophid *Lampanyctus festivus*, which has lateral-viewing eyes, has a relatively constant and low visual acuity (0.5°) over the entire visual field (Wagner *et al.*, 1998). Because this increased spatial resolution decreases sensitivity (and hence ability to detect contrast), it has an associated cost. Warrant and Locket (2004) analyzed the benefits and costs of high spatial resolution as a function of what is being viewed; they determined that high spatial resolution should be selected for in eyes that search overhead for small, silhouetted objects. While they do not explicitly consider the spatial pattern of counterillumination, the same principles apply.

The high spectral variation of the background light and the spectral mismatches seen in Figure 8 suggest that good color discrimination in the blue-green would be extremely advantageous. As mentioned above, certain deep-sea species probably have good color discrimination at blue and green wavelengths. Indeed, the peaks of these pigments seem to support the hypothesis of Douglas *et al.* (1998) that one pigment matches the counterilluminator's spectrum and one matches the downwelling light (Fig. 8). In addition, certain species with only one visual pigment have multi-banked retinas. The filtering of the light by the vitread banks alters the spectrum of the light reaching the sclerad banks, changing their sensitivity and theoretically allowing for color discrimination (Denton and Locket, 1989). Finally, the lenses of certain deep-sea species have yellow filters that can also increase the contrast of a counterilluminator against the background (Munz, 1976; Douglas and Thorpe, 1992).

Conclusions

Although counterillumination is a ubiquitous and successful cryptic strategy, the clarity of the water implies that the camouflage can be broken by species with acute vision at longer distances than anticipated. In addition, the background to be matched depends not only on depth, but also on the source of nocturnal illumination. While spectral variation is greatest near the surface, contrast attenuation is also greatest. These results suggest several fruitful avenues for future research, including further analysis of the conflicting constraints of visual sensitivity and spatial resolu-

tion, a determination of how counterilluminators that can change spectral emissions choose the correct spectrum (despite being color-blind), and investigation of a possible relationship between the resolution of ventral photophore patterns and the acuity of potential predators.

Acknowledgments

Literature Cited

Anthony, P. D. 1981. Visual contrast thresholds in the cod *Gadus morhua. J. Fish Biol.* **19:** 87–103.

Biggley, W. H., T. Napora, and E. Swift. 1981. The color of bioluminescent secretions from decapod prawns in the genera *Oplophorus* and *Systellaspis* (Caridea). Pp. 66–71 in *Bioluminescence: Current Perspectives*, K. H. Nealson, ed. Burgess Publishing, Minneapolis, MN.

Bogucki, D. J., J. A. Domaradzki, D. Stramski, and J. R. Zaneveld. 1998. Comparison of near-forward scattering on oceanic turbulence and particles. *Appl. Optics* **37:** 4669–4671.

Bohren, C. F., and D. R. Huffman. 1998. *Absorption and Scattering by Small Particles*. John Wiley & Sons, New York.

Bond, A. B., and A. C. Kamil 2002. Visual predators select for crypticity and polymorphism in virtual prey. *Nature* **415:** 609–613.

Capone, A., T. Digaetano, A. Grimaldi, R. Habel, D. Lo Presti, E. Migneco, R. Masullo, F. Moro, M. Petruccetti, C. Petta, P. Piatelli, N. Randazzo, G. Riccobene, E. Salusti, P. Sapienza, M. Sedita, L. Trasatti, and L. Ursella. 2002. Measurements of light transmission in deep sea with the AC9 transmissometer. *Nucl. Instr. Meth. Phys. Res.* **487:** 423–434.

Collin, S. P., R. V. Hoskins, and J. C. Partridge. 1997. Tubular eyes of deep-sea fishes: a comparative study of retinal topography. *Brain Behav. Evol.* **50:** 335–357.

Denton, E. J., and N. A. Locket. 1989. Possible wavelength discrimination by multibank retinae in deep-sea fishes. *J. Mar. Biol. Assoc. UK* **69:** 409–435.

Denton, E. J., J. B. Gilpin-Brown, and P. G. Wright. 1972. The angular distribution of the light produced by some mesopelagic fish in relation to their camouflage. *Proc. R. Soc. Lond. B* **182:** 145–158.

Denton, E. J., P. J. Herring, E. A. Widder, M. F. Latz, and J. F. Case. 1985. The roles of filters in the photophores of oceanic animals and their relation to vision in the oceanic environment. *Proc. R. Soc. Lond. B* **225:** 63–97.

Douglas, R. H., and C. W. Hawryshyn. 1990. Behavioral studies of fish vision: an analysis of visual capabilities. Pp. 373–418 in *The Visual System of Fish*, R. H. Douglas and M. B. A. Djamgoz, eds. Chapman and Hall, New York.

Douglas, R. H., and A. Thorpe. 1992. Short-wave absorbing pigments in the ocular lenses of deep-sea teleosts. *J. Mar. Biol. Assoc. UK* **72:** 93–112.

Douglas, R. H., J. C. Partridge, and N. J. Marshall. 1998. The eyes of

deep-sea fish. I. Lens pigmentation, tapeta and visual pigments. *Prog. Retin. Eye Res.* **17:** 597–636.

Frank, T. M. 1999. Comparative study of temporal resolution in the visual systems of mesopelagic crustaceans. *Biol. Bull.* **196:** 137–144.

Goodman, J. W. 1996. *Introduction to Fourier Optics*. McGraw Hill, New York.

Haddock, S. H. D., and J. F. Case. 1999. Bioluminescence spectra of shallow and deep-sea gelatinous zooplankton: ctenophores, medusae, and siphonophores. *Mar. Biol.* **133:** 571–582.

Hamilton, W. D. 1971. Geometry for the selfish herd. *J. Theor. Biol.* **31:** 295–311.

Harper, R. D., and J. F. Case. 1999. Disruptive counterillumination and its anti-predatory value in the plainfish midshipman *Porichthys notatus. Mar. Biol.* **134:** 529–540.

Herring, P. J. 1977. Luminescence in cephalopods and fish. *Symp. Zool. Soc. Lond.* **38:** 127–159.

Herring, P. J. 1983. The spectral characteristics of luminous marine organisms. *Proc. R. Soc. Lond. B* **220:** 183–217.

Herring, P. J. 1985. Bioluminescence in the crustacea. *J. Crustac. Biol.* **5(4):** 557–573.

Herring, P. J., E. A. Widder, and S. H. D. Haddock. 1992. Correlation of bioluminescence emissions with ventral photophores in the mesopelagic squid *Abralia veranyi* (Cephalopoda: Enoploteuthidae). *Mar. Biol.* **112:** 293–298.

Herring, P. J., M. I. Latz, N. J. Bannister, and E. A. Widder. 1993. Bioluminescence of the poecilostomatoid copepod *Oncaea conifera. Mar. Ecol. Prog. Ser.* **94:** 297–309.

Jaffe, J. S. 1992. Validity and range of linear approximations in underwater imaging. Pp. 388–396 in *Ocean Optics XII*, G. D. Gilbert, ed. The International Society of Optical Engineering, Bellingham, WA.

Johnsen, S. 2002. Cryptic and conspicuous coloration in the pelagic environment. *Proc. R. Soc. Lond. B* **269:** 243–256.

Johnsen, S., and H. M. Sosik. 2003. Cryptic coloration and mirrored sides as camouflage strategies in near-surface pelagic habitats: implications for foraging and predator avoidance. *Limnol. Oceanogr.* **48:** 1277–1288.

Land, M. F. 1999. Compound eye structure: matching eye to environment. Pp. 51–71 in *Adaptive Mechanisms in the Ecology of Vision*, S. N. Archer, M. B. A. Djamgoz, E. R. Loew, J. C. Partridge, and S. Vallerga, eds. Kluwer Academic, Boston.

Latz, M. I. 1995. Physiological mechanisms in the control of bioluminescent countershading in a midwater shrimp. *Mar. Freshw. Behav. Physiol.* **26:** 207–218.

Lythgoe, J. N. 1979. *The Ecology of Vision*. Clarendon Press, Oxford.

Marshall, B. R., and R. C. Smith. 1990. Raman scattering and in-water optical properties. *Appl. Optics* **29:** 71–84.

Mertens, L. E. 1970. *In-Water Photography: Theory and Practice*. John Wiley, New York.

Mertens, L. E., and R. S. Replogle. 1977. Use of point spread and beam spread functions for analysis of imaging systems in water. *J. Opt. Soc. Am.* **67:** 1105–1117.

Mobley, C. D. 1994. *Light and Water: Radiative Transfer in Natural Waters*. Academic Press, New York.

Mobley, C. D., B. Gentili, H. R. Gordon, Z. Jin, G. W. Kattawar, A. Morel, P. Reinersman, K. Stamnes, and R. H. Stavn. 1993. Comparison of numerical models for computing underwater light fields. *Appl. Optics* **32:** 7484–7504.

Munz, W. R. A. 1976. On yellow lenses in mesopelagic animals. *J. Mar. Biol. Assoc. UK* **56:** 963–976.

Munz, F. W., and W. N. McFarland. 1977. Evolutionary adaptations of fishes to the photic environment. Pp. 194–274 in *The Visual System of Vertebrates*, F. Crescitelli, ed. Springer-Verlag, New York.

Nicol, J. A. C. 1960. Spectral composition of the light of the lantern-fish, *Myctophum punctatum. J. Mar. Biol. Assoc. UK* **39:** 27–32.

Petzold T. J. 1977. Volume scattering functions for selected ocean waters. Pp. 150–174 in *Light in the Sea,* J. E. Tyler, ed. Dowden, Hutchinson, and Ross, Stroudsberg, PA.

Swift, E., W. H. Biggley, and H. H. Seliger. 1973. Species of oceanic dinoflagellates in the genera *Dissodinium* and *Pyrocystis:* interclonal and interspecific comparisons of the color and photon yield of bioluminescence. *J. Phycol.* **9:** 420–426.

Swift, E., W. H. Biggley, and T. Napora. 1977. The bioluminescence emission spectra of *Pyrosoma atlanticum, P. spinosum* (Tunicata), *Euphausia tenera* (Crustacea) and *Gonostoma sp.* (Pisces). *J. Mar. Biol. Assoc. UK* **57:** 817–823.

Ulloa, O., S. Sathyendranath, and T. Platt. 1994. Effect of the particle-size distribution on the backscattering ratio in seawater. *Appl. Optics* **33:** 7070–7077.

Vecchione, M., and C. F. E. Roper. 1991. Cephalopods observed from submersibles in the western north Atlantic. *Bull. Mar. Sci.* **49:** 433–445.

Voss, K. J. 1991. Simple empirical model of the oceanic point spread function. *Appl. Optics* **30:** 2647–2651.

Wagner, H. J., E. Froehlich, K. Negishi, and S. P. Collin. 1998. The eyes of deep-sea fish II. Functional morphology of the retina. *Prog. Retin. Eye Res.* **17:** 637–685.

Warrant, E. J. 1999. Seeing better at night: life style, eye design, and the optimum strategy of spatial and temporal summation. *Vision Res.* **39:** 1611–1630.

Warrant, E. J., and N. A. Locket. 2004. Vision in the deep sea. *Biol. Rev. Camb. Philos. Soc.* (In press).

Widder, E. A. 1999. Bioluminescence. Pp. 555–581 in *Adaptive Mechanisms in the Ecology of Vision,* S. N. Archer, M. B. A. Djamgoz, E. R. Loew, J. C. Partridge, and S. Vallerga, eds. Kluwer Academic, Boston.

Widder, E. A., M. I. Latz, and J. F. Case. 1983. Marine bioluminescence spectra measured with an optical multichannel detection system. *Biol. Bull.* **165:** 791–810.

Young, R. E., and J. M. Arnold. 1982. The functional morphology of a ventral photophore from the mesopelagic squid, *Abralia trigonura. Malacologia* **23:** 135–163.

Young, R. E., and F. M. Mencher. 1980. Bioluminescence in mesopelagic squid: diel color change during counterillumination. *Science* **208:** 1286–1288.

Young, R. E., and C. F. E. Roper. 1976. Bioluminescent countershading in midwater animals: evidence from living squid. *Science* **191:** 1046–1048.

Appendix D.

A comparison of Multi-layer Perceptron and multilinear regression algorithms for the inversion of synthetic ocean colour spectra

S. DRANSFELD†, A. R. TATNALL‡, I. S. ROBINSON§ and
C. D. MOBLEY*

†CLS (Collect Localisation Satellite), Direction d'Océanographie Spatiale,
Parc Technologique du canal, 8–10 rue Hermes, 31526 Ramonville St Agne,
France; e-mail: sdransfeld@cls.fr
‡University of Southampton Astronautics Group, School of Engineering
Sciences, University of Southampton, Highfield, Southampton, Hampshire
SO17 1BJ, UK
§Southampton Oceanography Centre Highfield, Southampton, Hampshire
SO17 1BJ, UK
*Sequoia Scientific, Inc. Westpark Technical Center, 15317 NE 90th Street,
Redmond, WA 98052, USA

Abstract. Artificial radiance sets were used as inputs to Multi-layer Perceptron and multilinear regression algorithms to study their retrieval capabilities for optically active constituents in sea water. The radiative transfer model Hydrolight was used to produce 18,000 artificial reflectance spectra representing various case 1 and case 2 water conditions. The remote sensing reflectances were generated at the Medium Resolution Imaging Spectrometer (MERIS) wavebands 412, 442, 490, 510, 560, 620, 665 and 682 nm from randomly generated triplet combinations of chlorophyll a, non-chlorophyllous particles and CDOM (Coloured Dissolved Organic Matter) concentrations. These reflectances were contaminated with different noise terms, before they were used to assess the performance of multilayer perceptron and multilinear regression algorithms. The potential of both algorithms for retrieving optically active constituents was demonstrated with the neural network showing more accurate results for case 2 scenarios.

1. Introduction

With the deployment of the Medium Resolution Imaging Spectrometer (MERIS) instrument on board the Envisat satellite from the European Space Agency, a need has arisen for more complex ocean colour algorithms that cater for the larger selection of bands that MERIS has to offer compared to similar instruments. This should result in more accurate results for coastal regions than from previous ocean colour instruments. Coastal regions are very dynamic environments where conditions vary over short time and spatial scales. Tidal currents and river-runoff carrying coloured dissolved organic matter (CDOM) and suspended sediment into the oceans influence ocean colour in these waters (Gould and Arnone 1997). Coastal waters are typically classified as case 2, signifying that

chlorophyll a is not the only significant influence on the colour and there are other optically active substances not correlated with the chlorophyll a (Mobley 1994). In such waters, the concentration of the optically active constituents needs to be estimated from the surface colour spectra. Numerous algorithms have been developed to undertake this process and recently some based on multi-layer perceptron (MLP) neural networks have shown promising capabilities (Gross *et al.* 2000). The purpose of this research letter is to compare the ocean colour parameter estimation performance of neural networks and multilinear regression algorithms presented with ocean colour spectra obtained from the ocean colour model Hydrolight.

2. Artificial radiance spectra generation

The data used for this research were artificially generated as an alternative to the use of *in situ* measurements of water parameters matched to a concurrent satellite overpass. This approach was adopted in order to have control over the amount of noise in the spectral sets. In total 18,000 remote sensing reflectance spectra were produced; 9000 for case 1 and 9000 for case 2 conditions. This was carried out in three steps described in the following three sections. Section 2.4 describes the noise terms added to the data.

2.1. *Generation of optically active parameter concentrations*

Chlorophyll a, non-chlorophyllous matter and CDOM can be expressed as the optically active parameters (OAPs) in sea water. Their parameterisations are the chlorophyll a mass to volume concentration C (mg m^{-3}), the scattering coefficient of non-chlorophyllous particles at 550 nm X (m^{-1}) and the absorption coefficient of yellow substance at 440 nm Y (m^{-1}). A combination of C, X and Y is used to produce one spectrum. A random number generator has been used to create the OAP combinations according to the statistical distribution parameters shown in table 1, where μ and σ represent the distribution mean and standard deviation respectively. The values for case 1 water in table 1 have been based on the analysis of a CZCS (coastal zone colour scanner) global composite pigment map histogram and the case 2 water values reflect typical case 2 concentration ranges (Cipollini 1996).

2.2. *The bio-optical model*

To evaluate the scattering and absorption values in the water related to each combination of OAP values, a biooptical model was used. Total absorption a was partitioned into the separate contributions of pure seawater a_w, phytoplankton a_{ph},

Table 1.   Statistical properties of OAP generation.

	Case I waters		Case II waters	
	μ_{Log}	σ_{Log}	μ_{Log}	σ_{Log}
Log(C)	−0.86	0.3	0.0	0.5
Log(X)	−1.21	0.3	0.0	0.5
Log(Y)	−1.75	0.3	−0.5	0.5
correlation	$\rho_{Log(C),Log(X)}$ 0.8	$\rho_{Log(C),Log(Y)}$ 0.8	$\rho_{Log(C),Log(X)}$ 0.5	$\rho_{Log(C),Log(Y)}$ 0.5

sediment a_{sed} and CDOM a_y. The scattering coefficient was partitioned into the separate contributions of water b_w, phytoplankton b_{ph} and sediment scattering b_{sed}.

The biooptical model was used to obtain the total absorption and scattering coefficients for the eight MERIS bands. Once these had been calculated, they were used as the inputs to the radiative transfer model that converted the absorption and scattering coefficients into the remote sensing reflectances. The detailed biooptical model can be found in Cipollini *et al.* (2001). The phytoplankton scattering coefficient included a fluorescence peak directly proportional to the C concentration which, in this letter, has been amended slightly to avoid a fluorescence peak solely dependent on the chlorophyll a concentration. Expression (1) shows the amended scattering coefficient for phytoplankton based on the original expression given by Cipollini *et al.* (2001).

$$b_{ph} = 0.3 C^{0.62} \left(1 + R9 \exp\left[-\frac{(\lambda - 685)^2}{200} \right] \right) \tag{1}$$

The amendment consists of a random variable R controlling the height of the fluorescence peak that was originally modelled by superimposing a Gaussian peak onto the phytoplankton scattering spectrum commonly modelled as a flat line.

2.3. *Radiative transfer model*

The absorption and scattering values computed by the biooptical model were used as an input to the radiative transfer model Hydrolight (Mobley, 1995) that generated the remotely sensed reflectance for each OAP combination. Two datasets for case 1 and case 2 waters, respectively, were created each totalling 9000 spectra and their corresponding OAP combinations.

2.4. *Noise terms added to datasets*

Three different noise terms were added to the datasets to represent noise due to the remote sensing instrument, an *in situ* measurement noise inherent to any instrument calibration datasets and an atmospheric correction error residual to ocean colour products after the atmospheric contributions have been removed. The instrument noise is a Gaussian noise within $\pm 2\%$ of the reflectance value in each band and the *in situ* noise is a Gaussian noise within $\pm 40\%$ of the concentration value of each OAP. In both cases the percentages represent the extremes the noiselevels can reach. The atmospheric correction error was simulated by taking three reflectance values at the bands 442, 490 and 560 nm, suggested by Antoine and Morel (1999) to be the largest allowable errors for an atmospheric correction, and using these values as negative and positive limits for a Gaussian error distribution. The values for the remaining bands were found by linear interpolation and extrapolation so that the maximum error spectrum shown in table 2 was obtained.

3. Algorithms

The MLP neural network used for the case 1 data set had 8 input nodes, 4 nodes in the first hidden layer, 3 in the next and 3 output nodes for each OAP derived. A sigmoid nodal transfer function was used for both case 1 and case 2 data. The case 2 MLP was chosen to be a bit more complex so that it could deal with the greater spread of the case 2 data. It consisted of 8 input nodes, 6 nodes in

Table 2. Atmospheric noise boundaries.

Wavelength (nm)	Reflectance $+/-$
412	0.003
442	0.002
490	0.0005
510	0.0004
560	0.0002
620	0.0002
665	0.0002
682	0.0002

the first hidden layer, three nodes in the second hidden layer and 3 output nodes. These architectures were determined, by a systematic procedure of reducing complex nets to simpler ones without a loss of performance. In that procedure, nodes were removed from the MLPs until their performance in terms of relative RMS errors and determination coefficients, started deteriorating, i.e. the errors increased and the determination coefficients decreased. A similar procedure was carried out to find optimum training and query set sizes as well as the optimum number of iterations before over fitting becomes an issue. For both case 1 and case 2 the training and query set sizes were 6000 and 3000 spectra, respectively, as well as a training time of 6000 iterations.

The multilinear regression as shown in (2) was carried out on the 6000 spectra used for the training set, and the 3000 spectra for the test set were used to assess the performance of the regression.

$$\log(C) = a_0 + \sum_{i=1}^{N} a_i \log(R_i) \tag{2}$$

4. Results for case 1 and case 2 waters

The capacity of the algorithms' outputs to match the original spectra-generating OAPs is presented in terms of the relative root-mean-square error

$$\text{relative rms} = \sqrt{\frac{1}{n} \sum_{k=1}^{n} \left[\frac{t^k - o^k}{t^k} \right]^2}$$

indicating the precision of the predicted values, and the coefficient of determination R^2:

$$R^2 = 1 - \frac{SSE}{SST}, \text{ where } SSE = \sum (y_i - \hat{y}_i)^2 \text{ and } SST = \left(\sum y_i^2 \right) - \frac{\left(\sum y_i \right)^2}{n}$$

$$SSE = \text{sum of squares error}, \; SST = \text{total sum of squares}$$

$$y_i = \text{datapoint}, \; \hat{y}_i = \text{adjunct point on trendline}$$

$$t = \text{target value}, \; o = \text{output value from neural network}$$

The results of all algorithms for the case 1 water set can be seen in table 3a & b. For case 1, the neural network and multilinear algorithm perform similarly with large R^2 values and small RMS errors. The MLP is showing an overall more accurate performance despite a slightly larger RMS error for the estimation of C.

Table 3(a). rel. RMS errors and R^2 for case 1.

Algorithm	C rRMS	X rRMS	Y rRMS	C R^2	X R^2	Y R^2
MLP	0.220	0.208	0.178	0.902	0.912	0.903
ML	0.197	0.219	0.215	0.869	0.881	0.855

Table 3(b). rel. RMS errors and R^2 for case 2.

Algorithm	C rRMS	X rRMS	Y rRMS	C R^2	X R^2	Y R^2
MLP	0.539	0.418	0.226	0.651	0.953	0.920
ML	0.909	0.240	0.290	0.557	0.938	0.825

For case 2 the MLP is most accurate for the estimation of C and Y whereas the ML algorithm estimates X more precisely indicated by the smaller RMS error.

5. Conclusion

Whereas both algorithms show similar performance levels for case 1 data, the MLP shows a more significant potential for the retrieval of OAPs from reflectance spectra of the case 2 dataset. Hence the authors propose that for ocean colour algorithm development, emphasis should be placed on the use of MLP neural networks. However, the relatively inaccurate results also evident for the MLP, during the C retrieval of case 2 water parameters indicate the difficulty associated with these waters. One of the main challenges for ocean colour algorithm development therefore is the creation of algorithms capable of generating accurate ocean colour products from case 2 regional imagery. The case 2 data generated for this letter are generic representing a wide variety of conditions. The great variability that exists between different case 2 regions in contrast suggests that algorithms should be developed using regionally specific models.

Acknowledgments

References

ANTOINE, D., and MOREL, A., 1999, A multiple scattering algorithm for atmospheric correction of remotely sensed ocean colour (MERIS) instrument: principles and implementation for atmospheres carrying various aerosols including absorbing ones. *International Journal of Remote Sensing*, **20**, 1875–1916.

CIPOLLINI, P., and CORSINI, G., 1996, "The Modular Optoelectronic Scanner MOS: a study of its capabilities for optically active parameter estimation by means of an ocean colour model" Ocean Optics XIII, Proc. SPIE no. 2963, Halifax (Canada), 22–25 October 1996, pp. 648–653.

CIPOLLINI, P., CORSINI, G., DIANI, M., and GRASSO, R., 2001, "Retrieval of Sea Water Optically Active Parameters from Hyperspectral data by means of Generalised Radial Basis Function Neural Networks", IEEE Transactions on Geoscience and Remote Sensing, vol. 39, no. 7, pp. 1508–1524.

GOULD, R. W., and ARNONE, R. A., 1997, Remote Sensing Estimates of Inherent Optical Properties in a Coastal Environment. *Remote Sensing Environment*, **61**, 290–301.

GROSS, L., THIRIA, S., FROUIN, R., and MITCHELL, B. G., 2000, Artificial neural networks

for modelling the transfer function between marine reflectance and phytoplankton pigment concentration. *Journal of Geophysical Research*, **105**, 3483–3495.

MOBLEY, C., 1994, *Light and Water: Radiative Transfer in Natural Waters*. London, Academic Press Ltd.

MOBLEY, C., 1995, Hydrolight, source code for Radiative Transfer model.

MOREL, A., 1988, Optical modelling of the upper ocean in relation to its biogenous matter content (case I waters). *Journal of Geophysical Research*, **93**, 10749–10768.

Appendix E.

Radiative transfer equation inversion: Theory and shape factor models for retrieval of oceanic inherent optical properties

Frank E. Hoge

National Aeronautics and Space Administration, Goddard Space Flight Center, Wallops Flight Facility, Wallops Island, Virginia, USA

Paul E. Lyon

E. G. & G. Inc., Wallops Flight Facility, Wallops Island, Virginia, USA

Curtis D. Mobley and Lydia K. Sundman

Sequoia Scientific, Inc., Redmond, Washington, USA

[1] It is shown that the in-water, shape factor formulation of the radiative transfer equation (RTE) (1) yields exact in-air expressions for the remote sensing reflectance R_{rs} and the equivalent remotely sensed reflectance RSR_a and (2) can be configured for inherent optical property (IOP) retrievals using standard linear matrix inversion methods. Inversion of the shape factor RTE is exact in the sense that no approximations are made to the RTE. Thus errors in retrieved IOPs are produced only by uncertainties in (1) the models for the shape factors and related quantities and (2) the IOP models required for inversion. Hydrolight radiative transfer calculations are used to derive analytical models for the necessary backscattering shape factor, radiance shape factor, fractional forward scattering coefficient, ratio of air-to-water mean cosines, and diffuse attenuation coefficient for in-water upwelling radiance. These models predict the various shape factors with accuracies ranging typically from 2 to 20%. Using the modeled shape factors the in-air remotely sensed reflectance RSR_a can be predicted to within 20% of the correct (Hydrolight-computed) values 96% of the time (or ± 0.0005 sr^{-1} 86% of the time) for the synthetic data used to determine the shape factor models. Inversion of this shape factor RTE using field data is a comprehensive study to be published in a later paper.   *INDEX TERMS:* 4552 Oceanography: Physical: Ocean optics; 4847 Oceanography: Biological and Chemical: Optics; 4275 Oceanography: General: Remote sensing and electromagnetic processes (0689); 4842 Oceanography: Biological and Chemical: Modeling; *KEYWORDS:* remote sensing, optical oceanography, inverse modeling, radiative transfer theory

1. Introduction

[2] Semianalytic radiance models [*Gordon et al.*, 1988; *Morel and Gentili*, 1996] can be readily inverted by linear matrix methods [*Hoge et al.*, 1999a, 1999b, 2001] to provide oceanic inherent optical properties (IOPs). Such inversions are well conditioned [*Hoge and Lyon*, 1996] and promise a powerful method of simultaneously retrieving constituent absorption and backscattering coefficients in the upper surface layer of the world's oceans using satellite data [*Hoge et al.*, 2001; *Hoge and Lyon*, 2002]. However, semianalytic radiance models (1) do not provide an exact framework to account for all possible environmental and viewing conditions [*Weidemann et al.*, 1995] and (2) contain fixed constants that both obscure insight into the physical radiative transfer processes and limit their flexibility.

[3] The radiative transfer equation (RTE) can provide exact inverse solutions, but the RTE is not easily inverted for many remote sensing situations [*Zaneveld*, 1995]. Therefore a specific form of the RTE inversion is investigated, namely a modified version of the shape factor formulation of *Zaneveld* [1995]. Some of the motivation for the work herein comes from the distinct need for highly accurate methods to retrieve the absorption coefficients of the chlorophyll accessory pigment phycoerythrin [*Hoge et al.*, 1999b]. To this end the absorption coefficients of chlorophyll and chromophoric dissolved organic matter (CDOM) must be accurately retrieved; otherwise, weaker absorbing constituents (such as phycoerythrin) will be obscured.

[4] In this paper (1) the shape factor form of the RTE is shown to be readily configured into linear form for simultaneous retrieval of oceanic IOPs using standard matrix methods; (2) the RTE inversion is derived for the principal

"big three" IOPs, namely the phytoplankton absorption coefficient, the CDOM + detritus absorption coefficient, and the total constituent backscattering coefficient; (3) shape factor and related models required for the inversion are developed for backscattering and radiance shape factors, the diffuse attenuation coefficient for upwelling radiance, the ratio of average cosines of the air and water downwelling irradiances, and the fractional forward scattering coefficient; and (4) propagation of errors into the IOP state vector resulting from errors in the data-model matrix and hydrospheric vector as well as shape factor and related models are assessed.

[5] Our ultimate objective is to determine if the shape factor RTE matrix inversion methodology will result in accurate algorithms for application to satellite ocean color data. This paper presents the underlying shape factor RTE theory and develops the needed models for the shape factors and related quantities, while future work will describe comprehensive studies of the shape factor RTE inversion of synthetic and real data.

2. Shape Factor Form of the Radiative Transfer Equation

[6] Establish a Cartesian coordinate system with $+z$ axis vertically downward into the ocean and x and y axes lying within the atmosphere-ocean boundary. In a plane parallel medium without internal sources or inelastic scattering, the radiative transfer equation is

$$\cos\theta \frac{dL(\theta,\phi,z)}{dz} = -c(z)L(\theta,\phi,z)$$
$$+ \int_0^{2\pi}\int_0^{\pi} \beta(\theta,\phi;\theta',\phi';z)L(\theta',\phi',z)\sin\theta'\,d\theta'\,d\phi'.$$
$$(1)$$

(See notation section for definition of symbols.) *Zaneveld* [1995, 1982] showed that equation (1) can be rewritten in terms of the in-water remotely sensed reflectance (*RSR*) as

$$RSR = \frac{L_u(\theta,\phi,z)}{E_{od}(z)} = \frac{f_b(\theta,\phi,z)\frac{b_b(z)}{2\pi}}{-\cos\theta\,k(\theta,\phi,z) + c(z) - f_L(\theta,\phi,z)b_f(z)},$$
$$(2)$$

where the dimensionless backscattering shape factor $f_b(\theta, \phi, z)$ is given by

$$f_b(\theta,\phi,z) = \frac{\int_0^{2\pi}\int_0^{\pi/2} \beta(\theta,\phi;\theta',\phi',z)L_d(\theta',\phi',z)\sin\theta'd\theta'\,d\phi'}{\frac{b_b}{2\pi}E_{od}(z)}, \quad (3)$$

the dimensionless radiance shape factor $f_L(\theta, \phi, z)$ is given by

$$f_L(\theta,\phi,z) = \frac{\int_0^{2\pi}\int_{\pi/2}^{\pi} \beta(\theta,\phi;\theta',\phi',z)L_u(\theta',\phi',z)\sin\theta'\,d\theta'\,d\phi'}{b_f(z)L_u^{iso}(z)}, \quad (4)$$

and the diffuse attenuation coefficient for upwelling radiance $k(\theta, \phi, z)$, with units of m^{-1}, is given by

$$k(\theta,\phi,z) = -\frac{1}{L_u(\theta,\phi,z)}\frac{dL_u(\theta,\phi,z)}{dz}. \quad (5)$$

Equation (2) is *Zaneveld*'s [1995] equation (7) and is exact because it is simply a restatement of the RTE (1) for upward directions using definitions (3)–(5). Subscripts d and u appended to the radiance L explicitly remind us that the radiance in equation (3) is downwelling ($0 \leq \theta \leq \pi/2$), whereas the radiance in equations (4) and (5) is upwelling ($\pi/2 < \theta \leq \pi$). (The iso- superscript is discussed below.)

[7] The numerator of the f_b shape factor in equation (3) shows how much downwelling radiance is scattered upward into direction (θ, ϕ). The denominator is the same quantity evaluated for the special case of an isotropic volume scattering function (in which case $\beta = 2b_b/4\pi$). Thus the f_b shape factor is a measure of how much the actual phase function differs from a constant over the backscattering directions. Similarly, the numerator of f_L in equation (4) shows how much the upwelling radiance is forward scattered into direction (θ, ϕ). The denominator is the same quantity evaluated for the special case of an isotropic upwelling radiance distribution whose magnitude is L_u^{iso} and for the special case of an isotropic volume scattering function. Clearly, these shape factors depend both on the IOPs (namely on the volume-scattering function, in this case) and on the ambient radiance distribution, as does the diffuse attenuation coefficient of equation (5). These quantities therefore are unknown terms in equation (2) if equation (2) is to be inverted to obtain the IOPs a and b_b from measured upwelling radiances and downwelling irradiances. The fact that shape factors are unknown prevents the RTE in equation (2) from being inverted unless further assumptions are made about the values of the shape factors. Modeling these unknowns in terms of known quantities is the major focus of this paper.

[8] Equations (1)–(5) are valid at any depth within an arbitrarily stratified water column, but the specific interest herein is remote sensing of near-surface water IOPs. Therefore one needs to relate the quantities in equations (2)–(5), when evaluated just beneath the mean sea surface, to quantities in air just above the sea surface, which can be deduced via in-air remote sensing techniques. Equation (2) can be converted into a form suitable for above-water remote sensing applications as follows. The n-squared law for radiance transmittance across a boundary between two media [*Mobley*, 1994, equation (4.21)] can be used to convert the in-water upwelling radiance just beneath the sea surface, $L_u(\theta, \phi, z = 0)$, to the water-leaving radiance in-air just above the sea surface, $L_{ua}(\theta_a, \phi)$:

$$L_u(\theta,\phi,z=0) = \frac{n_w^2}{t}L_{ua}(\theta_a,\phi). \quad (6)$$

Subscript a denotes values in air, just above the mean sea surface; depth $z = 0$ denotes values in water, just beneath the sea surface. The in-air polar angle θ_a associated with $L_{ua}(\theta_a, \phi)$ is the refracted viewing angle above the sea surface obtained by applying Snell's law to the in-water

angle θ. The downwelling scalar irradiance $E_{od}(z)$ is converted to the downwelling plane irradiance $E_d(z)$ via the mean cosine of the downwelling radiance, $\bar{\mu}_d$: $E_{od}(z) = E_d(z)/\bar{\mu}_d$. The plane irradiance just beneath the sea surface can be related to the in-air value via [*Mobley*, 1994, equation (7.19)] $E_d(z = 0) = E_{da}\bar{t}/(1 + rR)$. Combining these results gives [*Mobley*, 1994, equation (10.27)]

$$\frac{L_u(\theta, \phi, z = 0)}{E_{od}(z = 0)} = \frac{n_w^2(1 - rR)\bar{\mu}_d}{t\,\bar{t}} \frac{L_{ua}(\theta_a, \phi)}{E_{da}}. \quad (7)$$

In equation (7), define $M \equiv [(t\,\bar{t})/[(1 - rR)n_w^2]$. For a wide range of sky and sea surface conditions and for viewing directions relevant to remote sensing, M lies in the range of 0.53 to 0.55 [*Mobley*, 1994; *Hoge and Lyon*, 1996; *Hoge et al.*, 1999a, 1999b; *Morel and Gentili*, 1996]. Thus M can be approximated as $M \approx 0.54$, with an error of less than 2%. Using equation (7) and partitioning the beam attenuation coefficient as $c(z) = a(z) + b_f(z) + b_b(z)$, equation (2) becomes

$$R_{rs} = \frac{L_{ua}(\theta_a, \phi)}{E_{da}}$$
$$= \frac{M f_b(\theta, \phi, 0)\, b_b(0)/[2\pi\,\bar{\mu}_d(0)]}{-k(\theta, \phi, 0)\cos\theta + b_f(0)[1 - f_L(\theta, \phi, 0)] + a(0) + b_b(0)}. \quad (8)$$

Except for the small error associated with the assumed value for M, equation (8) remains an exact RTE expression for the in-air remote sensing reflectance, R_{rs}, just above the sea surface. The remote sensing reflectance is the quantity used as the basis for ocean color remote sensing by the Sea-viewing Wide Field-of-view Sensor (SeaWiFS) [*O'Reilly et al.*, 1998; *Hoge et al.*, 2001; *Hoge and Lyon*, 2002] and airborne systems [*Davis et al.*, 2002; *Hoge et al.*, 1999a, 1999b] systems. R_{rs} can be obtained from at-sensor radiances after atmospheric correction; for our purposes here it is therefore considered known. As noted by *Zaneveld* [1995], it is desirable to use RSR_a, the in-air value of RSR, rather than R_{rs} because the scalar irradiance E_{od} is less sensitive to solar zenith angle effects than is the plane irradiance E_d. Thus use $RSR_a = \bar{\mu}_{da}R_{rs}$ to rewrite equation (8) as

$$RSR_a = \frac{L_{ua}(\theta_a, \phi)}{E_{oda}}$$
$$= \frac{M\dfrac{f_b(\theta, \phi, 0)}{2\pi}\dfrac{\bar{\mu}_{da}}{\bar{\mu}_d(0)}b_b(0)}{-k(\theta, \phi, 0)\cos\theta + b_f(0)[1 - f_L(\theta, \phi, 0)] + a(0) + b_b(0)}. \quad (9)$$

The simplicity of *Zaneveld's* [1995] original in-water *RSR* formulation remains in this equation for RSR_a, except for M and the $\bar{\mu}_{da}/\bar{\mu}_d$ ratio for the downwelling light field. As a practical matter, equation (8) is presently more easily applied to oceanic field data because the in-air downwelling plane irradiance is more generally available, but there are no instrumental barriers to using scalar irradiance as in equation (9).

[9] To further simplify equation (9) for later use, define the first term in the denominator as

$$D_L(\theta, \phi, 0) = -k(\theta, \phi, 0)\cos\theta. \quad (10)$$

Call D_L the radiance derivative term because it is a measure of the depth rate of change of the upwelling radiance, as seen in equation (5). Define the second term in the denominator as

$$B_f(\theta, \phi, 0) \equiv b_f(0)[1 - f_L(\theta, \phi, 0)]. \quad (11)$$

The shape factor f_L varies from 0.963 to 1.152 for nadir viewing [*Weidemann et al.*, 1995; *Zaneveld*, 1995]; thus B_f ranges from $0.037b_f$ to $-0.152b_f$, which is a small fraction of the forward scattering coefficient b_f. Therefore call B_f the fractional forward scattering coefficient. Thus b_f and f_L are found in a combination in which one (f_L) serves to reduce the size of the other (b_f). Finally, define the mean cosine ratio as

$$R_\mu = \frac{\bar{\mu}_{da}}{\bar{\mu}_d(0)}. \quad (12)$$

Using definitions (10)–(12), equation (9) becomes

$$RSR_a(\theta_a, \phi) = \frac{L_{ua}(\theta_a, \phi)}{E_{oda}}$$
$$= \frac{M\dfrac{f_b(\theta, \phi, 0)}{2\pi}R_\mu\, b_b(0)}{D_L(\theta, \phi, 0) + B_f(\theta, \phi, 0) + a(0) + b_b(0)}. \quad (13)$$

Equations (8), (9), and (13) are each called the shape factor form of the RTE. Equation (13) is addressed hereafter. The ultimate goal is to use equation (13) to relate the unknown absorption and backscattering coefficients just beneath the sea surface to the known remotely sensed reflectance and other known quantities. As noted above, $M = 0.54$. However, the four quantities f_b, R_μ, D_L, and B_f (or, equivalently, f_b, R_μ, k, and b_f $(1 - f_L)$ as seen in equation (9) and for brevity call all of these quantities shape factors) are unknown. The shape factors depend in complicated ways on the water column IOPs, environmental conditions (sky radiance and sea state), and viewing geometry (Sun zenith angle and viewing direction). In section 4 the shape factors are modeled, so that they too can be considered known in equation (13).

3. Linear Form of the Radiative Transfer Equation and Its Inversion

[10] The in-air RSR_a of equation (13) immediately yields the fundamental linear form of the RTE,

$$a(0) + b_b(0)V + D_L + B_f = 0, \quad (14)$$

where

$$V(\theta, \phi, 0) = 1 - \frac{M\dfrac{f_b(\theta, \phi, 0)}{2\pi}R_\mu}{\dfrac{L_{ua}(\theta_a, \phi)}{E_{oda}}}. \quad (15)$$

V is called the backscattering enhancement factor.

[11] Next, partition the total absorption coefficient into contributions by pure water, phytoplankton, and CDOM

plus detritus. Similarly, the backscattering coefficient is written as the sum of contributions by pure seawater and by particulate matter. It is easy to show [*Hoge and Lyon*, 1996; *Hoge et al.*, 1999a, 1999b] that the equation describing the desired phytoplankton absorption coefficient a_{ph}, CDOM + detritus absorption coefficient a_d, and total constituent backscattering coefficient b_{bt} resulting from equation (14) is

$$a_{ph}(\lambda_i) + a_d(\lambda_i) + b_{bt}(\lambda_i)V = -a_w(\lambda_i) - b_{bw}(\lambda_i)V - D_L - B_f. \tag{16}$$

The wavelength dependency of the IOPs is now shown explicitly, while the depth and angular dependencies have been suppressed for clarity. Note that the observed water-leaving radiances L_{ua} occur on both sides of the equation (within V). The pure water absorption a_w is known from *Pope and Fry* [1997], and the water backscattering coefficient b_{bw} is given by *Smith and Baker* [1981]. The right-hand side of equation (16) is therefore known, given the shape factors and a measurement of $RSR_a(\lambda_i)$. This linear form of the RTE is still exact in the sense that no approximations have been made to the RTE, but clearly, the IOP retrieval accuracy will be determined by the accuracy of the shape factor models.

[12] Given the water-leaving radiance at three wavelengths, equation (16) still cannot be solved for the "big three" IOPs, $a_{ph}(\lambda_i)$, $a_d(\lambda_i)$, and $b_{bt}(\lambda_i)$, because each measurement of $RSR_a(\lambda_i)$ yields an equation with three unknown IOPs. However, it is easy to show that a consistent solution is available by introducing spectral models for $a_{ph}(\lambda_i)$, $a_d(\lambda_i)$, and $b_{bt}(\lambda_i)$ [*Hoge and Lyon*, 1996; *Hoge et al.*, 1999a, 1999b]. Substitution of such spectral models for $a_{ph}(\lambda_i)$, $a_d(\lambda_i)$, and $b_{bt}(\lambda_i)$ into equation (16) yields

$$a_{ph}(\lambda_g) \exp\left[-\frac{(\lambda_i - \lambda_g)^2}{2g^2}\right]$$
$$+ a_d(\lambda_d) \exp[-S(\lambda_i - \lambda_d)] + b_{bt}(\lambda_b)\left(\frac{\lambda_b}{\lambda_i}\right)^n V$$
$$= - a_w(\lambda_i) - b_{bw}(\lambda_i)V - D_L - B_f. \tag{17}$$

Equation (17) now has only three unknowns, $a_{ph}(\lambda_g)$, $a_d(\lambda_d)$, and $b_{bt}(\lambda_b)$, so that the system is solvable given measurements of $RSR_a(\lambda_i)$ at three wavelengths. This linear form of the radiative transfer equation remains exact and precise, but the uncertainty in the retrieved IOPs is now additionally influenced by the uncertainty in the IOP models [*Hoge et al.*, 1999a, 1999b] (in addition to the shape factors).

[13] At their respective reference wavelengths, λ_g, λ_d, and λ_b, the IOPs $a_{ph}(\lambda_g)$, $a_d(\lambda_d)$, and $b_{bt}(\lambda_b)$, are linearly related to the column matrix, or vector, containing the hydrospheric constants (sea water absorption and backscattering), radiances, and the shape factors. (It is easy to see from equation (16) that it is, in principle, possible to concurrently solve for the radiance derivative term $D_L(\lambda_i)$ and/or for the fractional forward scattering coefficient, B_f, in addition to the IOPs, given measurements of $RSR_a(\lambda_i)$ at additional wavelengths. However, the IOP models then must be of sufficient accuracy at yet a fourth and/or fifth wavelength,

and the required wavelength dependency of these models was not a focus of this study. Therefore such retrievals are beyond the scope of this initial RTE inversion work.) Equation (17) is very similar to the one used to analyze the effect of radiance errors and model uncertainties upon IOPs [*Hoge and Lyon*, 1996], and to retrieve IOPs from atmospherically corrected airborne and satellite upwelling radiances [*Hoge et al.*, 1999a, 1999b, 2001] when retrieved by semianalytic radiance model inversion. Equation (17) can therefore be written in matrix form as

$$Dp = h. \tag{18}$$

Here the hydrospheric vector h is given by the right-hand side of equation (17). The IOP state vector is $p = [a_{ph}(\lambda_g), a_d(\lambda_d), b_{bt}(\lambda_b)]^T$, where T denotes the transpose and D is the data-model matrix [*Hoge and Lyon*, 1996; *Hoge et al.*, 1999a, 1999b, 2001], which also contains shape factors. The IOPs are immediately determined from $p = D^{-1}h$.

[14] The uncertainties in the IOP state vector p can be analyzed in a manner similar to other linear inversions [*Hoge and Lyon*, 1996]. Since $p = D^{-1}h$, both D and h determine p and the errors that propagate into p. Because the backscattering shape factor f_b is always found within D, f_b influences the propagation of errors into the IOPs more so than the remaining factors. The discussion of the uncertainties in the IOP state vector p caused by possible singularity of D^{-1} and by perturbations in D somewhat parallels a similar previous discussion [*Hoge and Lyon*, 1996] and is briefly addressed in a later section herein.

4. Models for Shape Factors and Related Quantities

[15] Inversion of equation (17) using remotely sensed ocean color data requires knowledge of V, D_L, and B_f. These quantities in turn depend on the shape factors f_b and f_L, the diffuse attenuation coefficient k, and the mean cosine ratio R_μ, as defined above. For ease of comparison with previous work on shape factors [*Weidemann et al.*, 1995] and to reveal the underlying physics as much as possible, explicit models for f_b, f_L, k, and R_μ, are given rather than D_L and B_f. For notational convenience, let X_i with $i = 1$, 2, 3, and 4 denote f_b, f_L, k, and R_μ, respectively.

[16] Because shape factors, diffuse attenuation functions, and mean cosines all depend on the ambient radiance, they depend implicitly on the solar zenith angle and viewing direction, as well as on the IOPs. The solar angle and viewing direction are known in any particular remote sensing situation; these geometric quantities are thus available for modeling the X_i in terms of known quantities. However, the IOPs are unknown. Explicit inversions of the RTE (to obtain the IOPs) excludes the IOPs from the models for the X_i. However, an implicit, or iterative, inversion of the RTE, can include the retrieved IOPs in the X_i models, for the following reason. In an iterative inversion, one starts with an initial guess for the X_i, derived either from models that do not include IOPs or from physical intuition. (For example, a reasonable initial guess for f_b would be 1, the value corresponding to a constant phase function. Similarly, $f_L = 1$, $k = 0$, and $R_\mu = 1$ would be acceptable initial guesses.) Using the initial guesses for the X_i, the RTE is

Table 1. Parameters and Their Values Used to Generate the Original Database of 184,800 Records[a]

Parameter	Values Used in Hydrolight Runs
chlorophyll concentration, *Chl*	**0.1, 0.5, 1.0, 5.0, 10.0** mg m^{-3}
solar zenith angle, θ_s	**0.0, 10, 20, 30, 40,** 60 degrees
wind speed	**0,** 10 m s^{-1}
cloud cover	**0,** 100%, i.e., clear sky and solid overcast
wavelength, λ	**412, 426, 440, 465, 490, 522.5, 555, 612, 670, 685** nm
polar viewing angle θ_v (in water, relative to the zenith)	**0.0, 10, 20, 30, 40,** 50, 60 degrees
azimuthal viewing angle ϕ_v (relative to Sun)	0, **90,** 180 degrees
depth, *z*	**0,** 0.5, 1, 1.5, 2, 2.5, 3, 3.5, 4, 4.5, 5 m

[a]The values shown in bold correspond to the 1,500 records in the remote sensing database.

inverted to obtain initial values for $a_{ph}(\lambda_g)$, $a_d(\lambda_d)$, and $b_{bt}(\lambda_b)$, from which the IOPs $a = a_t + a_w = a_{ph} + a_d + a_w$ and $b_b = b_{bt} + b_{bw}$ can be obtained at all wavelengths via the IOP models seen in equation (17). The X_i models developed below are based on an assumed phase function for particle scattering. Taking the particle phase function as known, the total constituent (particle) backscattering fraction $B_t = b_{bt}/b_t$ is also known. Thus the total constituent forward scattering coefficient b_{ft} can be obtained from the recovered b_{bt} and B_t: $b_{ft} = b_{bt}(1 - B_t)$. The total beam attenuation coefficient is then known from $c = a + b_{ft} + b_{bt} + b_w$. Therefore models are developed for the X_i that depend both on the known geometrical (viewing direction (subscript v), solar direction (subscript s), and physical (wind speed, wavelength)) parameters, as well as on certain IOPs (namely, a, c, and b_b).

4.1. Database

[17] To begin the analysis, 120 Hydrolight [*Mobley*, 2001a, 2001b] runs were made using its IOP model for case 1 waters and the Petzold "average particle" phase function [*Mobley et al.*, 1993] for scattering by the particles. This case 1 IOP model is a two-component model: pure water plus "everything else." The non-water absorption and scattering coefficients are parameterized in terms of the chlorophyll concentration according to commonly used models by *Mobley* [1994, equations (3.27) and (3.40)]. The input for these runs covered a wide range of chlorophyll concentrations, solar zenith angles, cloud covers, and wind speeds. Each Hydrolight run generated output at various wavelengths, depths, and viewing directions. The resulting database potentially contains millions of records, where one record corresponds to a particular set of input values, output values for a particular viewing geometry, wavelength, depth, etc., and the values of the four X_i. Some of these records are not of great interest, for example, records whose azimuthal viewing directions ϕ_v differ by only 15 degrees (the resolution of ϕ_v in the standard version of Hydrolight). Therefore selected records were used to generate a database of more manageable size but one that still covers the range of parameter values relevant to most remote sensing. Table 1 shows the input and output values in this database, which was used in the initial investigation of the functional forms of the X_i. Each of the four X_i was computed for each parameter combination represented in Table 1.

[18] First, the sensitivity of the X_i to the various parameters (wind speed, viewing direction, IOPs, etc.) available for construction of models for the X_i was examined. It was

found that the surface wind speed has a negligible effect on each of the X_i (less than 1% difference in X_i for the 0 and 10 m s^{-1} wind speeds, with all else being equal). Thus the wind speed was not considered in subsequent modeling. Likewise, for similar reasons, only the clear-sky data, which are of greatest interest for remote sensing applications were included. As noted above, for remote sensing applications the shape factors X_i need evaluation only at depth $z = 0$. (Note, however, that the values of the X_i at $z = 0$ incorporate the effects of all the absorption and multiple scattering occurring throughout the entire water column.) Thus only output from the Hydrolight runs at $z = 0$ was retained. The original database included records generated for azimuthal viewing angles of $\phi_v = 0$ (looking toward the Sun) and $\phi_v = 180$ degrees (looking away from the Sun). Most remote sensing is, or can be, accommodated at azimuthal angles of $\phi_v \approx 90$ degrees, which minimizes Sun glint and instrument self shading. Thus only the records corresponding to $\phi_v = 90$ degrees were included. Likewise, remote sensing generally uses in-air nadir viewing directions θ_{va} of less than 60 degrees, which correspond to in-water angles $\theta_v \leq 40$ degrees. Eliminating the larger in-water nadir viewing angles ($\theta_v = 50$ and 60 degrees in Table 1) gives a final "remote sensing" data set of 1500 records, which was used to determine models for the X_i. The parameter values corresponding to this remote sensing database are shown in bold in Table 1.

4.2. Determining Functional Forms

[19] Let P_k with $k = 1, \ldots, N_k$, denote the parameters (wavelength, viewing direction, IOPs, etc.) to be used in modeling the X_i. These parameters include those seen in Table 1, as well as the absorption, scattering, and backscattering coefficients (which are functions of the chlorophyll concentration if case 1 water is assumed).

[20] The simplest possible model for the X_i is a linear function of the P_k:

$$X_i = \sum_{k=1}^{N_k} \alpha_{ik} P_k, \quad i = 1, \ldots, 4. \tag{19}$$

The α_{ik} are fitting coefficients whose values are to be determined; a different set of coefficients is needed for each factor X_i. That is, a large linear least squares problem was initiated to determine if this model was adequate to fit the various factors. Not surprisingly, the fits were unsatisfactory. In other words, the ocean is more complicated than equation (19).

Figure 1. Sun, sensor, and single-scattering geometry. Equation (1) measures the polar angle θ from the nadir with $+z$ downward, and Hydrolight computes in this coordinate system as well, but the above-surface solar and viewing directions are shown for convenience as being measured from the zenith.

[21] The goal then became to develop models that are nonlinear in the parameters but still reflect the underlying physics of the X_i. Thus replace equation (19) by

$$X_i = \sum_{k=1}^{N(i)} F_{ik}(\{P_k\},\{\alpha_{ik}\}). \qquad (20)$$

This notation means that each function F_{ik} will contain some subset of the parameters P_k and will have its own set of fitting coefficients. For example, as shall be seen in the next section, the model for f_b will contain terms involving the scattering-to-backscattering ratio and a nonlinear function of the three geometric parameters (θ_s, θ_v, and ϕ_v), with four fitting coefficients in all.

4.3. Model for f_b

[22] To obtain initial guidance about the possible functional form for an f_b model, single-scattering theory was first used to evaluate the definition of f_b seen in equation (3). According to the single-scattering approximation (SSA), the downwelling radiance is [*Gordon*, 1994, equation (1.30)]

$$L_d(\theta',\phi',z) = E_{od}\delta(\mu'-\mu_s)\delta(\phi'-\phi_s)e^{-cz/\mu_s}, \qquad (21)$$

where $\mu = \cos\theta$ and (μ_s, ϕ_s) denote the in-water direction of the Sun's direct beam as refracted through a level sea surface; δ is the Dirac delta function. Inserting equation (21) into equation (3), integrating, and evaluating the result at $z = 0$ gives

$$f_b \approx 2\pi \frac{b}{b_b}\widetilde{\beta}(\mu_s,\phi_s,\mu,\phi). \qquad (22)$$

Note that for isotropic scattering, $\widetilde{\beta} = 1/4\pi$, $b = 2b_b$, giving $f_b = 1$, as expected. As the phase function becomes more anisotropic, b/b_b increases, and f_b increases. In equation (22) the phase function indicates that to first order, f_b involves downwelling radiance that is singly scattered from the Sun's direct beam into the viewing direction. In remote sensing applications the total phase function (water plus particles) will be unknown, but for any given phase function the contribution to f_b will depend on the scattering angle ψ corresponding to the Sun's downward beam being scattered into the upward viewing direction. This scattering angle is equivalent to the easily computed Sun sensor-included angle ξ, as shown in Figure 1. Given the Sun's location (θ_s; $\phi_s = 0$), the viewing direction (θ_v, ϕ_v), ξ is given by

$$\cos\xi = \cos\theta_s\cos\theta_v + \sin\theta_s\sin\theta_v\cos\phi_v.$$

Figure 2. Values of f_b plotted as a function of Sun sensor included angle ξ and coded to show the dependence on b/b_b.

Thus, as a preliminary functional form for the f_b model, consider the estimated backscattering shape factor

$$\hat{f}_b \propto \frac{b}{b_b} \Xi(\xi),$$

where $\Xi(\xi)$ is a function of angle ξ whose form is to be determined.

[23] Figure 2 shows the 1,500 values of f_b in the remote sensing database plotted as a function of ξ and b/b_b. This figure suggests that a cosine function may capture the ξ dependence. Thus construct a model of the form

$$\hat{f}_b = \alpha_1 + \alpha_2 \frac{b}{b_b} \cos(\alpha_3 \xi), \qquad (23)$$

where α_1, α_2, and α_3 are fitting coefficients (the α_{ik} of equation (20) for model $i = 1$) whose values are to be determined by minimizing the squared difference between $\hat{f}_b$ and f_b for the 1,500 values in the remote sensing database. Note from the points in Figure 2 that f_b is largest for small b/b_b, and vice versa, which is contrary to the behavior predicted by equation (22). This reversal may be due to the dominance of multiple scattering in ocean waters, but further investigations would be necessary to understand this discrepancy between the SSA predictions and the Hydrolight predictions, which include all orders of multiple scattering and other effects not included in the SSA. In any case, there is a clear dependence on b/b_b, which can be modeled.

[24] The best fit coefficients α_j in equation (23) were determined by least-squares minimization using a variety of numerical techniques appropriate for nonlinear functions. After comparing the model predictions $\hat{f}_b$ with the actual f_b values, it was seen that not all of the b/b_b dependence was

captured by the model of equation (23). Some experimentation showed that the remaining b/b_b dependence could be accounted for by adding another term proportional to b/b_b. Thus the final f_b took the form

$$\hat{f}_b = \alpha_1 + \alpha_2 \frac{b}{b_b} \cos(\alpha_3 \xi) + \alpha_4 \frac{b}{b_b}$$

$$= \alpha_1 + \alpha_4 \frac{b}{b_b} \left[1 + \frac{\alpha_2}{\alpha_4} \cos(\alpha_3 \xi) \right]. \qquad (24)$$

Equation (24) shows that the additive term is equivalent to keeping the general form of the model suggested by the SSA, but picking a different angular function $\Xi(\xi)$. The complicated dependence of f_b on b/b_b and ξ is not surprising if one remembers that the $\Xi(\xi)$ function is fundamentally an attempt to parameterize the unknown phase function effects for a given Sun and viewing geometry; thus the scattering and geometric effects are not independent. The final set of fitting coefficients for the model in equation (24) is shown in Table 2.

[25] Figure 3 shows the model and actual f_b values. The dashed lines are the 5% error bounds. Using the model of equation (24), 96.3% of the predicted values are within 5% of the correct value; the linear correlation coefficient between the model and actual points is $r = 0.955$. There is no systematic dependence on b/b_b or ξ of the model

Table 2. Best Fit Coefficients for the f_b Model of Equation (24)

Coefficient	Value
α_1	1.2077
α_2	0.001977
α_3	3.3790
α_4	−0.004863
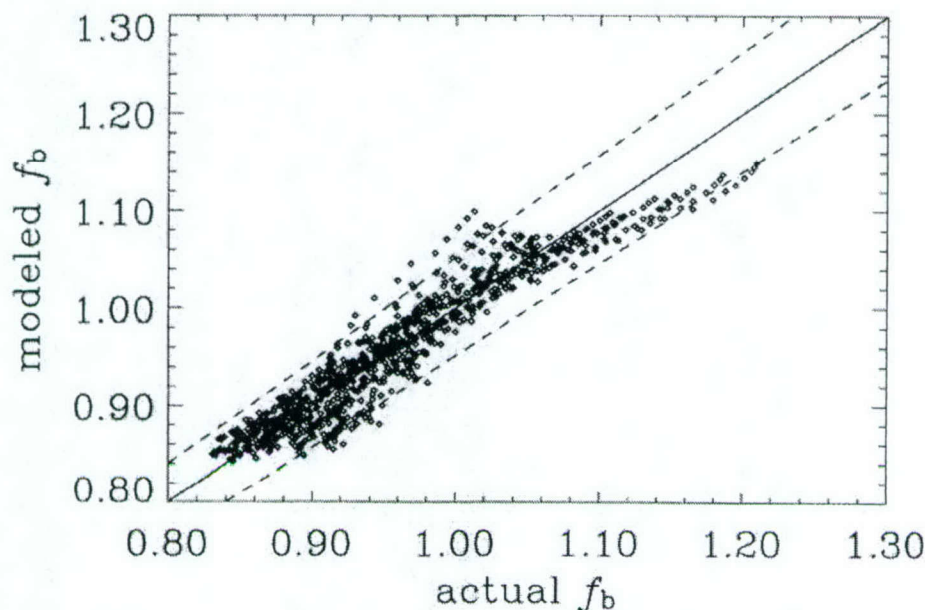
Figure 3. Comparison of modeled and actual f_b values, using the model of equation (24). Here 96.3% of the modeled values lie within the dashed lines, which represent values with 5% of the correct value; the model-actual correlation coefficient is $r = 0.955$.

discrepancies seen in the individual points of Figure 3. It would be possible to continue adding ad hoc terms in other variables to equation (24) and perhaps reduce the model-data discrepancy even more. However, such a process is likely to deviate from physical foundations, with the end result that the final model would not be applicable beyond the exact conditions used to generate the present remote sensing data set. For this initial study it is best to be content with the simple model of equation (24).

4.4. Model for $B_f = b_f[1 - f_L]$

[26] Since b_f is an IOP the model required for B_f is f_L. Just as with f_b, use the SSA for guidance as to the general form of the model for f_L. In the SSA the upwelling radiance is [*Gordon*, 1994, equation (1.32)]

$$L_u(\mu', \phi', z) = \frac{b}{c} E_d(0)\widetilde{\beta}(\mu_s, \phi_s, \mu', \phi') \frac{1}{\mu_s - \mu'} e^{-cz/\mu_s}. \quad (25)$$

Note that $\mu_s > 0$ and $\mu' < 0$. Inserting this SSA radiance into equation (4), the definition of f_L, integrating, and setting $z = 0$ gives

$$f_L \approx \frac{b_2 E_d(0)}{b_f c L_u^{iso}} \int_0^{2\pi} \int_0^{-1} \widetilde{\beta}(\mu', \phi', \mu, \phi)\widetilde{\beta}(\mu_s, \phi_s, \mu', \phi') \frac{1}{\mu_s - \mu'} d\mu' \, d\phi'.$$

In most ocean waters, $b \approx b_f$. However, further simplification is difficult. The remaining integrals describe how the Sun's downwelling direct beam is first scattered upward and then scattered again into the viewing direction. The most that can be said is that this is some function of the scattering phase function and the viewing geometry. As with f_b, this

function was parameterized in terms of the Sun sensor included angle ξ via a model of the form

$$\hat{f}_L \propto \frac{b}{c} \Xi(\xi).$$

Unfortunately, plots of f_L similar to Figure 2 did not suggest a clear functional form for $\Xi(\xi)$ or show any significant dependence on b/c. This failure of the SSA to provide a functional form for f_L is not surprising because f_L inherently involves at least two scatterings, and multiple scattering can be expected to make an important contribution to the upwelling radiance.

[27] Linear correlations between f_L and the various available fitting parameters were then examined. The results are seen in Table 3.

[28] The only potential model parameter that correlates well with f_L is the solar zenith angle θ_s. A plot of f_L versus θ_s

Table 3. Correlation Between the Radiance Shape Factor f_L and Various Parameters

Parameter	Correlation Coef. r With f_L
Absorption coefficient a	0.291
Scattering coefficient b	0.205
Albedo of single scattering b/c	−0.076
Backscattering coef b_b	0.180
Forward scattering coef b_f	0.206
Backscattering fraction b_b/b	−0.343
Forward scattering fraction b_f/b	0.343
Backscattering to absorption b_b/a	−0.231
Wavelength λ	0.210
Solar zenith angle θ_s	0.778
Polar viewing angle θ_v	−0.006
Sun sensor included angle ξ	−0.562
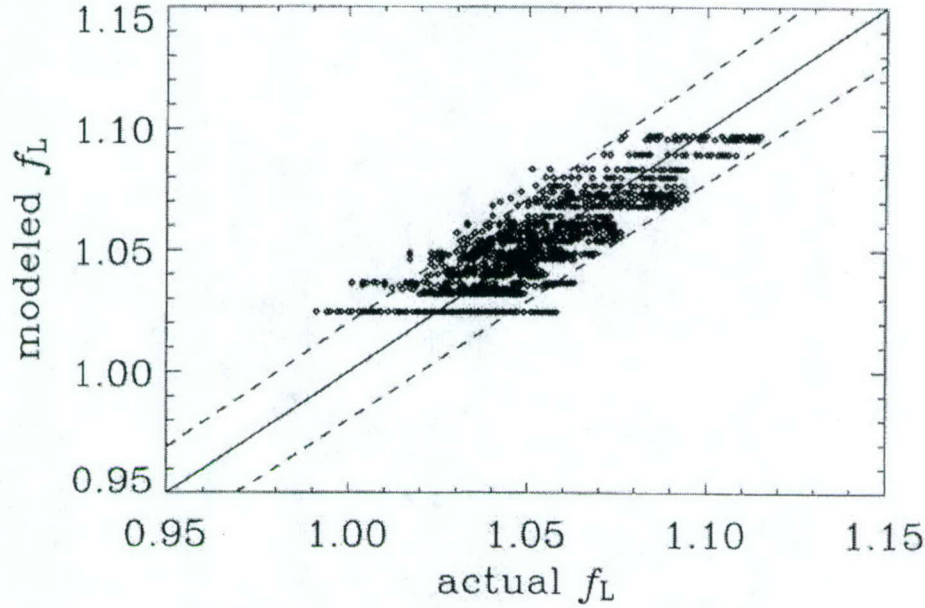
Figure 4. Comparison of modeled and actual f_L values, using the model of equation (24). Here 93.0% of the modeled values lie within the dashed lines, which represent values with 2% of the correct value; the model-actual correlation coefficient is $r = 0.829$.

suggested a sine function for θ_s (although a simple linear function is almost as good). Thus a model of the form $\hat{f}_L = \alpha_5 + \alpha_6 \sin(\alpha_7\theta_s)$ was tried. The residuals of this model showed a weak wavelength dependence. After considerable experimentation the model chosen was

$$\hat{f}_L = \alpha_5 + \alpha_6 \left(\frac{\lambda}{550}\right) \sin(\alpha_7\,\theta_s). \qquad (26)$$

The best fit values of the coefficients are $\alpha_5 = 1.0247$, $\alpha_6 = 0.4584$ (for λ in nanometers), and $\alpha_7 = 0.1221$ (for θ_s measured in radians). Figure 4 shows the scatterplot for this model. Here 93.0% of the model predictions are within 2% of correct (points lying between the dashed lines); the correlation coefficient is $r = 0.829$. Although it is possible to obtain slightly better fits by including IOPs in an ad hoc fashion, the model of equation (26) was selected because of its simplicity and because of the lack of physical guidance for the IOP dependence.

[29] Although one is unable to model the remaining variability of f_L in terms of the IOPs or other parameters, this may be of little importance in predicting f_L itself because f_L is always near 1. Perhaps more important is the fact that the variability in f_L determines the variability in the fractional forward scattering coefficient $B_f = b_f (1 - f_L)$. Small fractional errors in f_L can cause large fractional errors in B_f. Figure 5 shows the resulting scatterplot for B_f, computed using the exact values of b_f as found in the database. Although 93.0% of the f_L values are within 2% of their correct value, only 5.4% of the B_f values are within 2% of the correct value; 58.1% of the B_f are within 20% of the correct value. However, a percentage error criterion may be misleading for B_f because of the cluster of points near zero, where small absolute errors can be large fractional

errors. The dotted lines in Figure 5 thus show absolute errors of ± 0.02 m^{-1}; 94.5% of the B_f have errors smaller than this. The model-actual correlation coefficient is $r = 0.966$.

4.5. Model for k

[30] The SSA again suggests a functional form for the $k(\theta, \phi, z = 0)$ model. Differentiating the SSA upwelling radiance of equation (25) gives

$$k(\theta, \phi, 0) = \left[-\frac{1}{L_u(z)} \frac{dL_u(z)}{dz}\right]_{z=0} \approx \frac{c}{\cos(\theta_s)}.$$

Although k is strongly correlated with a ($r = 0.99$), it is not strongly correlated with c ($r = 0.56$). At the level of the quasi-single-scattering approximation (QSSA), which often works well for upwelling radiances, $c \approx a + b_b$, in which case, $k \approx (a + b_b)/\cos(\theta_s)$. This suggested a model k with the functional form

$$\hat{k} = \frac{\alpha_8 a + \alpha_9 b_b}{\cos(\theta_s)}. \qquad (27)$$

When equation (27) was used to fit the points in the remote sensing data set, the points separated into distinct groups for $\theta_s \geq 60°$ and for $\theta_s < 60°$. Plots of k and the residual error in k as functions of θ_s suggested that an additive $\sin(\theta_s)$ term would represent the θ_s dependence better than the $1/\cos(\theta_s)$ factor in equation (27). This then gave the final k model:

$$\hat{k} = \alpha_8 a + \alpha_9 b_b + \alpha_{10} \sin(\theta_s). \qquad (28)$$

The best fit parameters are $\alpha_8 = 1.0896$, $\alpha_9 = -0.5931$, and $\alpha_{10} = 0.0492$ (for a, b_b, and k in inverse meters). (Note that
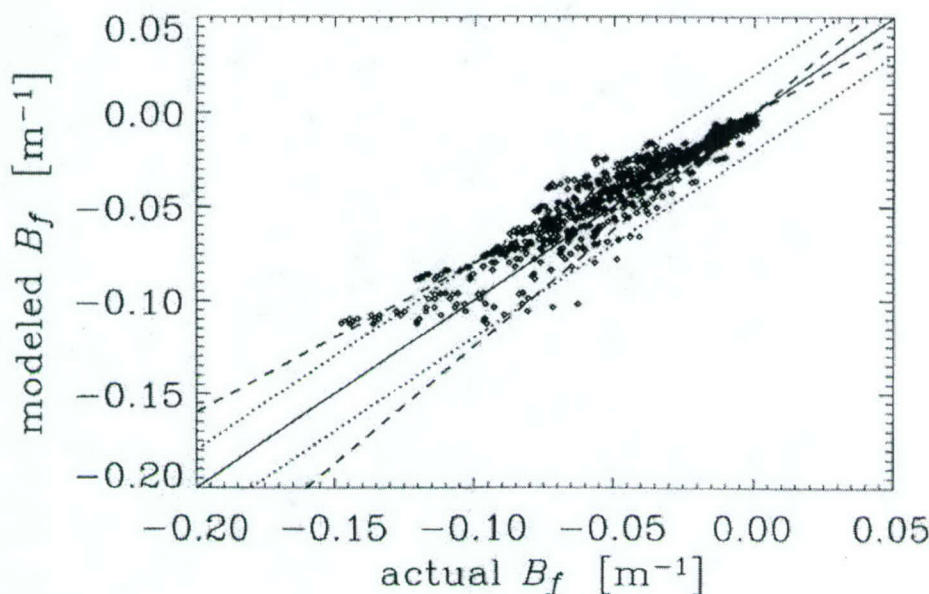
Figure 5. Comparison of modeled and actual B_f values, computed using the f_L model of equation (26). The dashed lines are 20% error bounds; the dotted lines are ± 0.02 m^{-1} error bounds.

although θ_s in equation (28) refers to the polar angle of the solar beam in water, the in-air solar zenith angle for θ_s, can be used because the index-of-refraction factor that converts $\sin(\theta_s$ in air) to $\sin(\theta_s$ in water) is incorporated into α_{10}.) The points still separate somewhat by $\theta_s \geq 60°$ and for $\theta_s < 60°$ but not as much as for equation (27). Although equation (28) has lost some of its intuitive, first-order physics, namely the $1/\cos(\theta_s)$ factor in equation (27), the final model does a better job of predicting k, which, of course, is influenced by multiple scattering and other effects not included in the SSA.

Figure 6 shows the scatterplot for the k model. Because of small differences near $k = 0$, only 76.8% of the points are within 20% of the correct value. However, 93.6% of the points lie within an absolute error of ± 0.05 m^{-1}. The model-actual correlation coefficient is $r = 0.993$.

4.6. Model for R_μ

[31] A model for $R_\mu = \bar{\mu}_d$(in air)/$\bar{\mu}_d$(in water at z = 0) can be constructed simply by using Snell's law to refract the direct solar beam through a level water surface. The result is
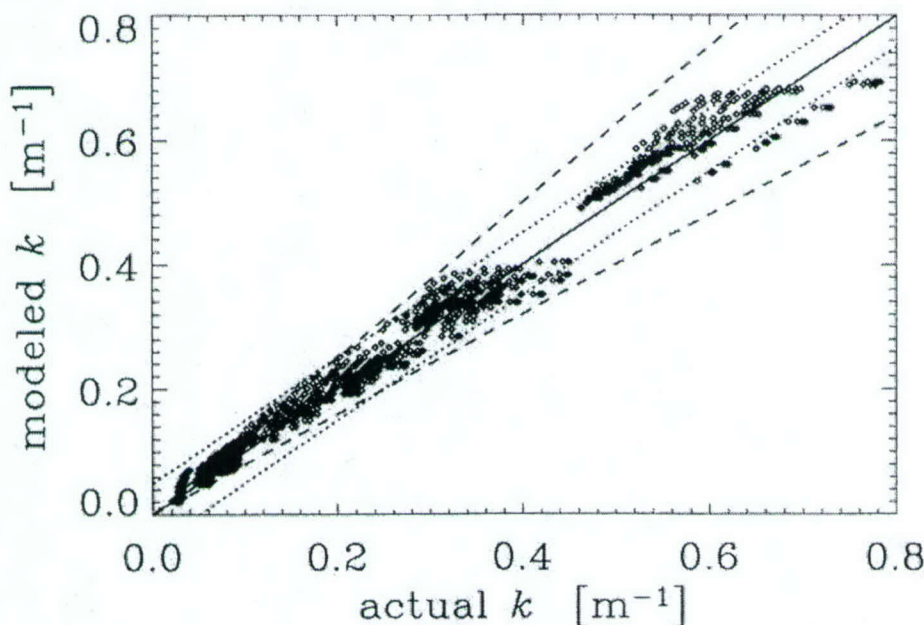
Figure 6. The k model of equation (28). The dashed lines are the 20% error bounds, and the dotted lines are ± 0.05 m^{-1} error bounds.
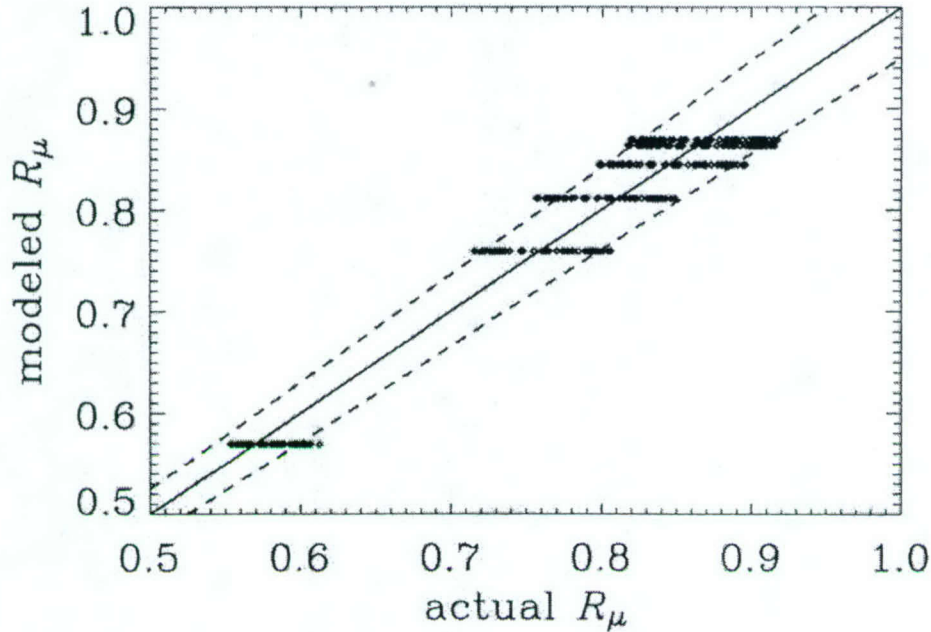
Figure 7. The model of equation (29) applied to the RS data set. The dashed lines are 5% error bounds.

$$\hat{R}_\mu = \alpha_{11} \frac{\cos\theta_s}{\cos\left[\sin^{-1}\left(\frac{\sin\theta_s}{n}\right)\right]} = \alpha_{11}\Theta(\theta_s), \qquad (29)$$

where $n = 1.34$ is the index of refraction of water. The ratio R_μ is independent of the viewing direction because the mean cosines are computed from integrals over the direction of the radiance distribution; there are consequently, many fewer distinct points in the data set. When equation (29) is applied to the RS data set, the best fit value is $\alpha_{11} = 0.869$. Figure 7 shows the results of this model applied to all points in the RS data set. The six groups of points correspond to the six solar angles in the data set: $\theta_s = 0, 10, 20, 30, 40,$ and 60 degrees. Here 85.7% of the points lie within 5% of the correct value, as shown by the dashed lines. The correlation coefficient is $r = 0.964$.

5. Remotely Sensed Reflectance RSR_a Estimation

[32] Models that estimate the shape factors and related quantities with varying degrees of certainty are now complete. The question next arises as to how well one can predict the remotely sensed reflectance RSR_a using these models within equation (9). Figure 8 gives the answer: 68.1% of the RSR_a predictions fall within 10% of the correct values, and 95.7% fall within 20% of correct (shown by the dashed lines in Figure 8); 85.6% of the predictions are within ± 0.0005 sr^{-1} of the correct value. The model-actual correlation coefficient is $r = 0.983$.

6. Discussion

[33] To facilitate a brief comparison of the shape factor models, propagation of errors into the retrieved IOPs, and

discussion of future inversion research, all the models are reassembled below.

$$\hat{f}_b = \alpha_1 + \alpha_4 \frac{b}{b_b}\left[1 + \frac{\alpha_2}{\alpha_4}\cos(\alpha_3\,\xi)\right]. \qquad (30)$$

$$\hat{B}_f = b_f\left(1 - \hat{f}_L\right) \quad where \quad \hat{f}_L = \alpha_5 + \alpha_6\left(\frac{\lambda}{550}\right)\sin(\alpha_7\theta_s). \quad (31)$$

$$\hat{k} = \alpha_8\,a + \alpha_9\,b_b + \alpha_{10}\sin(\theta_s). \qquad (32)$$

$$\hat{R}_\mu = \alpha_{11} \frac{\cos\theta_s}{\cos\left[\sin^{-1}\left(\frac{\sin\theta_s}{n}\right)\right]} = \alpha_{11}\Theta(\theta_s). \qquad (33)$$

Although they were derived from a physical basis, it was seen that the models could take various forms. At this early stage of development the above models probably represent the starting point of their eventual evolution.

[34] The highly important $\hat{f}_b$ model contains (1) two IOPs: b_b and b_f (but in a ratio combination $b/b_b = [(b_b + b_f)/b_b] = [1 + b_f/b_b]$), (2) the most model coefficients (four), and (3) the Sun sensor included angle ξ (but not the solar zenith angle θ_s as do all the other models). In contrast, the B_f model contains (1) the solar zenith angle and one IOP (b_f) and (2) the sole wavelength dependence found within the models. The $\hat{k}$ model contains only one IOP, b_b, and the solar zenith angle, θ_s. The $\hat{R}_\mu$ model contains no IOPs; only the solar zenith angle θ_s. (Inversion of the shape factor RTE also requires models for those IOPs that are to be retrieved. For example, the phytoplankton absorption coefficient a_{ph}, the CDOM/detritus absorption coefficient a_d and total constituent backscattering b_{bt} as given in equation (17).
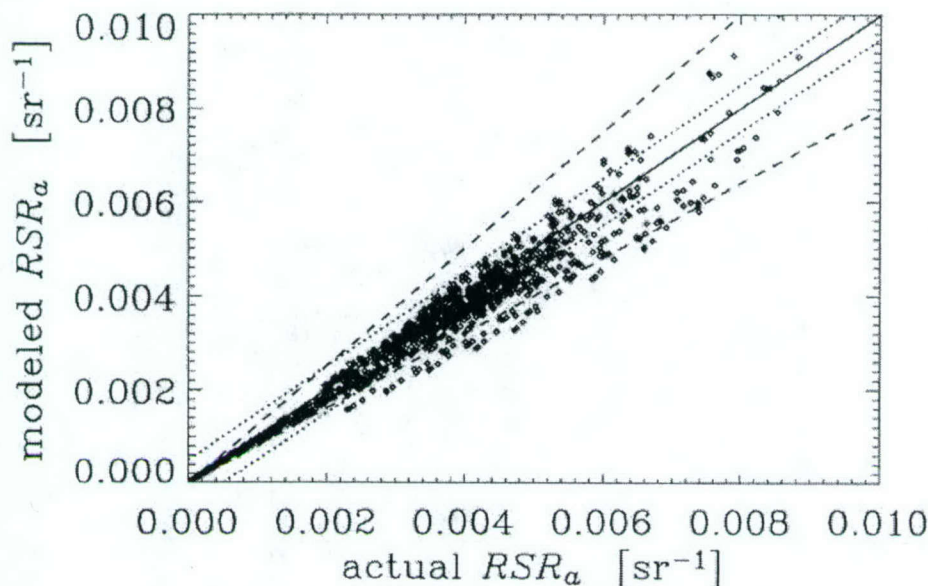
Figure 8. RSR_a as modeled by equation (9) using the four shape factor models. The dashed lines are 20% error bounds; the dotted lines are ± 0.0005 sr^{-1}.

These IOP models [*Hoge and Lyon*, 1996] are considered more mature than the shape factor models. Uncertainty propagated into retrieved IOPs by the IOP models used within a semianalytic radiance model inversion has been studied [*Hoge and Lyon*, 1996].)

[35] Thus, to initiate an iterative inversion, starting values are required for both b_b and b_f. Physics demands that $b_b \geq b_{bw}$, where b_{bw} is the backscattering coefficient for water. One possible method for selecting the starting value for b_b is to retrieve it by first executing a semianalytic model inversion [*Hoge and Lyon*, 1996; *Hoge et al.*, 1999a, 1999b, 2001]. Then it can continually be updated after each shape factor RTE inversion in equation (17) since $b_b = b_{bw} + b_{bt}$. Similarly, physics dictates and limits the range of b_f for the first iteration of the shape factor RTE inversion: $b_f \geq b_{fw}$ where b_{fw} is the forward scattering coefficient for water. Although $b_f = b_{fw}$ can perhaps be used as the starting value for the first iteration, future research efforts must develop methods for better (1) selection of starting values and (2) updating of the value during subsequent iterations. Like b_b, the b_f can, in principle, be retrieved using equation (17). This too, however, presents some concerns: (1) few if any models exist for b_f to allow its retrieval by equations (17) and (2) a concurrent retrieval of b_f potentially weakens the retrieval of the desired a_{ph}, a_d, and b_{bt}. Detailed error propagation analyses of the shape factor RTE inversion are outside the scope of this present paper, but a brief discussion of the relative influence of the shape factor models on the desired IOP state vector, $p = [a_{ph}(\lambda_g), a_d(\lambda_d) b_{bt}(\lambda_b)]^T$, is provided in the following section.

6.1. Uncertainties in the IOP State Vector p

6.1.1. Sensitivity of p to Perturbations in the Data-Model Matrix D

[36] As already noted, the inversion of the shape factor form of the RTE is exact from the standpoint of radiative

transfer theory, and uncertainties in the retrieved IOPs within the IOP state vector p are due only to the accuracy of the (1) shape factor models and their related quantities and (2) IOP models. Perturbations within D arise, for example, from the water-leaving radiances, scalar irradiances, IOP models, and backscattering shape factor contained within it. Similarly, uncertainties in h arise from the radiances, irradiances, hydrospheric constants (or IOP constants a_w and b_{bw}) for sea water, as well as f_b, $dL_u(\lambda_i)/dz$, $b_f(\lambda_i)$, $f_L(\lambda_i)$, and $\cos \theta$. Relative to h, the data-model matrix, D, plays the major role in the propagation of errors into p since $\|p - p'\|/\|p\| \leq \kappa(D) (\|\Delta_D\|/\|D\| + \|\delta_h\|/\|h\|)$, where $\|D\|$ is the determinate of D and $\kappa(D) = \|D\| \|D^{-1}\|$ [*Ortega*, 1990; *Hoge and Lyon*, 1996]. The latter expression is the condition number of D, and Δ_D and δ_h represent uncertainty or perturbation of D and h, respectively. Here p' is the perturbed solution of p. The first expression simply states that to first order the relative error in p can be $\kappa(D)$ times the relative error in D and h. Thus the propagation into p of the relative errors of both D and h is governed by the condition number of D. For any norm, $1 \leq \kappa(D) \leq \infty$. For the limiting cases: $\kappa(D) = 1$, D is said to be perfectly conditioned, while for $\kappa(D) = \infty$, D is singular. For intermediate values of $\kappa(D)$ the interpretation of the condition number is very subjective and must be evaluated separately. For large $\kappa(D)$ the D matrix is said to be ill conditioned and large errors may be found in p. For small $\kappa(D)$ the D matrix is said to be well-conditioned and smaller errors may be found in p. Of the shape factor components only f_b occurs in D (via V) and therefore provides the strongest influence on the IOP retrieval errors. This is in agreement with *Zaneveld* [1995], who concluded that f_b is most critical since the in-water remotely sensed reflectance (see equation (2)) is directly proportional to it. It is for this reason that shape factor RTE component model developments should probably focus on f_b.

[37] However, if other RTE components such as D_L (or dL_u/dz) and/or B_f are solved for, then they too will appear in the D matrix and thereby further increase the errors in p. Also, in general, the condition number increases as the number of unknowns increases [McCormick, 1992], contributing still more uncertainty in p. In part, the additional uncertainty in p will then be due to D_L and/or B_f model errors. If D_L and B_f are both zero, then equation (13) shows that both R_{rs} and RSR_a are linearly proportional to $b_b/(a + b_b)$, which is a well known *approximate* functional form for the dependence of water-leaving reflectances on the absorption and backscattering coefficients. However, other work [Gordon et al., 1988] suggests, but does not prove, that since the shape factor RTE is exact, both D_L and B_f cannot concurrently be zero. For example, the semianalytic model contains a quadratic term $[b_b/(a + b_b)]^2$, and this suggests that the multiplier $M \frac{f_b(\theta,\phi,0)}{2\pi} R_\mu$ in the numerator of equation (13) above must jointly account for both linear and quadratic variability in $b_b/(a + b_b)$ if both D_L and B_f are null. This comparison to the semianalytic model [Gordon et al., 1988] also suggests, but does not prove, that (1) D_L and B_f (when not being solved for) jointly contribute only a small amount to the reflectances and thus to the IOP retrievals and, (2) accordingly, their contribution to retrieved IOP uncertainty may not be strong.

6.1.2. Sensitivity of p to Perturbations in h

[38] While the condition of D is most important in determining the errors in the IOP state vector p, the error propagation equation, $\|p - p'\|/\|p\| \leq \kappa(D) (\|\Delta_D\|/\|D\| + \|\delta_h\|/\|h\|)$, shows that uncertainties in h also propagate into p.

6.2. Future Studies

[39] To fully understand how shape factor model errors affect the accuracy of retrieved IOPs, it is necessary to perform in-depth studies of the iterative shape factor inversion algorithm outlined above by (1) its application to synthetic and (2) actual data sets. Thus future research in our laboratories will study the details of the shape factor inversion in a controlled environment such as Hydrolight-generated synthetic RSR_a data, for which the correct IOP values are known from the input to the Hydrolight computer program. The inversion will then be applied to actual RSR_a or R_{rs} field data that further contain experimental errors. Too, the convergence and condition (i.e., well conditioned or ill conditioned) of successive iterations using the retrieved/updated b_f and b_b must also be assessed. Results of these anticipated studies of the inversion of the shape factor RTE are the subject of future publications.

Notation

a total absorption coefficient, $a_t + a_w$, m^{-1}; denotes "in air" when used as a subscript.

a_d absorption coefficient of CDOM and detritus, m^{-1}.

a_{ph} absorption coefficient of phytoplankton, m^{-1}.

a_t total constituent absorption coefficient, $a_t = a_{ph} + a_d$, m^{-1}.

a_w absorption coefficient of water, m^{-1}.

b total scattering coefficient, m^{-1}.

b_b total backscattering coefficient, $b_b = b_{bw} + b_{bt}$, m^{-1}.

b_f total forward scattering coefficient, m^{-1}.

b_{ft} total constituent forward scattering coefficient, m^{-1}.

b_{bt} total constituent backscattering (TCB) coefficient, m^{-1}.

b_{bw} backscattering coefficient of seawater, m^{-1}.

B_f fractional forward scattering coefficient, defined by equation (11), m^{-1}.

B_t b_{bt}/b_t, the total constituent (particle) backscattering fraction.

c beam attenuation coefficient, $c = a + b$, m^{-1}.

CDOM chromophoric dissolved organic matter.

D data and model matrix.

$\|D\|$ determinate of D.

D_L radiance derivative term, defined by equation (10), m^{-1}.

$E_{od}(z)$ downwelling scalar irradiance, in water, W m^{-2} nm^{-1}.

E_{oda} downwelling scalar irradiance, in air, just above sea surface, W m^{-2} nm^{-1}.

$E_d(z)$ downwelling plane irradiance, in water, W m^{-2} nm^{-1}.

E_{da} downwelling plane irradiance, in air, W m^{-2} nm^{-1}.

$E_u(z)$ upwelling plane irradiance, in water, W m^{-2} nm^{-1}.

E_{ua} upwelling plane irradiance, in air, W m^{-2} nm^{-1}.

F_{ik} modeling function; contains some subset of the parameters P_k.

f_b backscattering shape factor, dimensionless.

$\hat{f}_b$ estimated backscattering shape factor, dimensionless.

f_L radiance shape factor, dimensionless.

$\hat{f}_L$ estimated radiance shape factor, dimensionless.

$\bar{f}_L$ average of f_L values having θ_s in remote sensing data set.

g phytoplankton Gaussian model spectral width parameter, nm.

h vector of hydrospheric constants, shape factors, radiance attenuation coefficient, m^{-1}.

IOP inherent optical property.

K_{Lu} diffuse attenuation coefficient for upwelling radiance, $K_{Lu} = -d[\log L_u(z, \theta, \phi)]/dz$.

L_u upwelling radiance, below sea surface, W m^{-2} sr^{-1} nm^{-1}.

L_{ua} upwelling radiance, in air, just above sea surface, W m^{-2} sr^{-1} nm^{-1}.

M $[(\bar{t}\bar{t})/[(1 - rR)n_w^2] \approx 0.54$ for nominal sea conditions, dimensionless.

n total constituent backscattering coefficient spectral model exponent, as used in equation (17), dimensionless.

n_w index of refraction of sea water, dimensionless.

P_k modeling parameter; $k = 1,\ldots, N_k$, denote the parameters (wavelength, viewing direction, IOPs, etc) to be used in modeling the X_i.

p oceanic state vector of retrieved IOPs, $^{-1}$.

p' perturbed oceanic state vector of retrieved IOPs, $^{-1}$.

$\|p\|$ determinate of p.

r water-to-air surface reflectance for plane irradiance, dimensionless; correlation coefficient when specifically identified.

R plane irradiance reflectance, in water, $E_u(z)/E_d(z)$, dimensionless.

R_μ ratio of air-to-water mean cosines for downwelling irradiance.

$\hat{R}_\mu$ estimate of ratio of air-to-water mean cosines for downwelling irradiance.

RSR remotely sensed reflectance, in-water, $L_u(\theta, \phi, z)/E_{od}(z)$, sr^{-1}.

RSR_a remotely sensed reflectance, in air, $L_{ua}(\theta, \phi)/E_{oda} = \bar{\mu}_{da}R_{rs}$, sr^{-1}.

R_{rs} remote sensing reflectance, in air, $L_{ua}(\theta, \phi)/E_{da}$, sr^{-1}.

RTE radiative transfer equation.

s subscript denoting solar; used in subscript rs denotes remote sensing.

S spectral slope within the a_d model for CDOM+detritus, nm^{-1}.

t water-to-air radiance transmittance, dimensionless.

$\bar{t}$ water-to-air plane irradiance transmittance, dimensionless.

TCA total constituent absorption, a_t, m^{-1}.

TCB total constituent backscattering, b_{bt}, $^{-1}$.

v subscript; italicized letter "v" denoting viewing.

V backscattering enhancement factor, defined by equation (12), dimensionless.

X_i shape factors and related quantities; $i = 1, 2, 3,$ and 4, denote f_b, f_L, k, and R_μ respectively.

z depth, m.

α_i model fitting parameters, see text and tables for numerical values.

α_{ik} model fitting coefficients; a different set of coefficients is needed for each factor X_i.

β volume scattering function.

δ Dirac delta function.

Δ_D uncertainty or perturbation of D.

$\|\Delta_D\|$ determinate of Δ_D.

δ_h uncertainty or perturbation of h.

$\|\delta_h\|$ determinate of δ_h.

$\kappa(D)$ $\|D\| \|D^{-1}\|$, the condition number of D.

λ wavelength, nm.

λ_b reference λ for total constituent backscattering (TCB) coefficient model, nm.

λ_d reference wavelength for CDOM+detritus absorption coefficient model, nm.

λ_g peak wavelength for Gaussian phytoplankton absorption coefficient model, nm.

λ_i wavelength of observational bands, i = 1, 2, 3, ..., nm.

v italicized Greek letter nu is not used in this paper: see italicized letter "v" above.

$\bar{\mu}_d$ average cosine for downwelling irradiance, in water, dimensionless.

$\bar{\mu}_{da}$ average cosine for downwelling irradiance, in air, dimensionless.

ϕ azimuth angle, radians; subscripts v, s denote viewing, solar.

θ polar zenith angle in-water with respect to +z axis, radians; subscripts v, s, and a denote viewing, solar, and in-air, respectively.

ξ included angle, solar-to-viewing direction.

ω_o single-scattering albedo b/c.

References

Davis, C. O., et al., Ocean PHILLS hyperspectral imager: Design, characterization, and calibration, *Opt. Express*, *10*, 210–221, 2002.

Gordon, H. R., Modeling and simulating radiative transfer in the ocean, in *Ocean Optics*, edited by R. W. Spinrad, K. L. Carder, and M. J. Perry, chap. 1, pp. 3–39, Oxford Univ. Press, New York, 1994.

Gordon, H. R., O. B. Brown, R. H. Evans, J. W. Brown, R. C. Smith, K. S. Baker, and D. K. Clark, A semianalytic radiance model of ocean color, *J. Geophys. Res.*, *93*, 10,909–10,924, 1988.

Hoge, F. E., and P. E. Lyon, Satellite retrieval of inherent optical properties by linear matrix inversion of oceanic radiance models: An analysis of model and radiance measurement errors, *J. Geophys. Res.*, *101*, 16,631–16,648, 1996.

Hoge, F. E., and P. E. Lyon, Satellite observation of chromophoric dissolved organic matter (CDOM) variability in the wake of hurricanes and typhoons, *Geophys. Res. Lett.*, *29*(19), 1908, doi:10.1029/2002GL015114, 2002.

Hoge, F. E., C. W. Wright, P. E. Lyon, R. N. Swift, and J. K. Yungel, Satellite retrieval of inherent optical properties by inversion of an oceanic radiance model: A preliminary algorithm, *Appl. Opt.*, *38*, 495–504, 1999a.

Hoge, F. E., C. W. Wright, P. E. Lyon, R. N. Swift, and J. K. Yungel, Satellite retrieval of the absorption coefficient of phytoplankton phycoerythrin pigment: Theory and feasibility status, *Appl. Opt.*, *38*, 7431–7441, 1999b.

Hoge, F. E., C. W. Wright, P. E. Lyon, R. N. Swift, and J. K. Yungel, Inherent optical properties imagery of the western North Atlantic Ocean: Horizontal spatial variability of the upper mixed layer, *J. Geophys. Res.*, *106*, 31,129–31,140, 2001.

McCormick, N. J., Inverse radiative transfer problems: A review, *Nucl. Sci. Eng.*, *112*, 185–198, 1992.

Mobley, C. D., *Light and Water, Radiative Transfer in Natural Waters*, Academic, San Diego, Calif., 1994.

Mobley, C. D., *Hydrolight 4. 2 Users' Guide*, 88 pp., Sequoia Sci., Redmond, Wash., 2001a. (Available at www.sequoiasci.com.)

Mobley, C. D., *Hydrolight 4. 2 Technical Documentation*, 79 pp., Sequoia Sci., Redmond, Wash., 2001b.

Mobley, C. D., B. Gentili, H. R. Gordon, Z. Jin, G. W. Kattawar, A. Morel, P. Reinersman, K. Stamnes, and R. H. Stavn, Comparison of numerical models for computing underwater light fields, *Appl. Opt.*, *32*, 7484–7504, 1993.

Morel, A., and B. Gentili, Diffuse reflectance of oceanic waters. III. Implication of bidirectionality for the remote sensing problem, *Appl. Opt.*, *35*, 4850–4862, 1996.

O'Reilly, J., S. Maritorena, B. G. Mitchell, D. A. Siegel, K. L. Carder, S. A. Garver, M. Kahru, and C. McClain, Ocean color chlorophyll algorithms for SeaWiFS, *J. Geophys. Res.*, *103*, 24,937–24,953, 1998.

Ortega, J. M., Numerical analysis, in *A Second Course*, Soc. for Ind. and Appl. Math., Philadelphia, Pa., 1990.

Pope, R. M., and E. S. Fry, Absorption spectrum (380–700 nm) of pure water: II. Integrating cavity measurements, *Appl. Opt.*, *36*, 8710–8723, 1997.

Smith, R. C., and K. S. Baker, Optical properties of the clearest natural waters (200–800 nm), *Appl. Opt.*, *20*, 177–183, 1981.

Weidemann, A. D., R. H. Stavn, J. R. V. Zaneveld, and M. R. Wilcox, Error in predicting hydrosol backscattering from remotely sensed reflectance, *J. Geophys. Res.*, *100*, 13,163–13,177, 1995.

Zaneveld, J. R. V., Remotely sensed reflectance and its dependance on vertical structure: A theoretical derivation, *Appl. Opt.*, *21*, 4146–4150, 1982.

Zaneveld, J. R. V., A theoretical derivation of the dependance of the remotely sensed reflectance of the ocean on the inherent optical properties, *J. Geophys. Res.*, *100*, 13,135–13,142, 1995.

F. E. Hoge, National Aeronautics and Space Administration, Goddard Space Flight Center, Wallops Flight Facility, Wallops Island, VA 23337, USA. (frank.hoge@nasa.gov)

P. E. Lyon, E. G. & G. Inc., Wallops Flight Facility, Wallops Island, VA 23337, USA.

C. D. Mobley and L. K. Sundman, Sequoia Scientific, Inc., Westpark Technical Center, 15317 NE 90th Street, Redmond, WA 98052, USA.